Corrosion Evaluation of Chromized Steel Utilized in Automotive Exhaust Applications

CORROSION EVALUATION OF CHROMIZED STEEL UTILIZED IN AUTOMOTIVE EXHAUST APPLICATIONS

By YOEL EMUN, B.ENG.

A Thesis

Submitted to the Department of Materials Science & Engineering

and the School of Graduate Studies

in Partial Fulfilment of the Requirements

for the Degree Master of Applied Science

McMaster University

McMaster University

Hamilton, Ontario

MASTER OF APPLIED SCIENCE (2019)

(Materials Science and Engineering)

TITLE:

Corrosion Evaluation of Chromized Steel Utilized in Automotive Exhaust Applications

AUTHOR:

Yoel Emun, B. Eng. (McMaster University)

SUPERVISOR:

Dr. J.R. Kish, Dr. H. Zurob

NUMBER OF PAGES:

112

Abstract

Experiments were conducted to determine the suitability of a chromized steel for use in automotive exhaust applications. Due to government regulations leading to higher temperatures and a more corrosive environment within the automotive exhaust system, Cr-lean alloys such as Type 409 no longer suffice. The high cost of increasing alloying elements to reduce the corrosion susceptibility of exhaust components has led to exhaust manufactures moving toward a sacrificially protected aluminized stainless steel (Type 409Al). Yet, costs remain high due to the stainless steel substrate. Arcanum Alloys have designed a process in which an IF steel coil is chromized using a Cr-rich slurry, creating a thin but corrosion resistant layer. This chromized layer drastically increases the corrosion resistance, without affecting the formability of the interstitial-free (IF) steel substrate and remaining cost-effective. The localized corrosion resistance of the chromized IF steel (XHOM) was measured against current generation ferritic stainless steels in a simulated interior (exhaust gas condensate) and exterior (NaCl (aq)) automotive exhaust environment.

Electrochemical polarization measurements along with atmospheric corrosion tests were conducted to characterize and compare the localized corrosion susceptibility of XHOM and benchmark ferritic stainless steels. The specific tests include the following:

I. Potentiodynamic polarization curves in NaCl (aq), measuring the corrosion potential (E_{corr}), critical current density (i_{crit}) and breakdown potential (E_b).

II. Double loop electrochemical potentiokinetic reactivation (DLEPR) testing measuring the ratio of the activation critical current density (i_a) and the reactivation critical current density (i_r).

III. Salt-fog testing (ASTM B117) (external) and exhaust gas condensate exposure testing (internal), measuring the mass loss, pitting density, maximum pit depth and corrosion rate.

Although Type 409 and Type 439 exhibited evidence of sensitization in the mill annealed condition, all materials exhibited a resistance to further sensitization during heat treatment, indicating sensitization will not occur during service.

The electrochemical polarization curves in the NaCl (aq) resulted in XHOM yielding the highest breakdown potential, yet XHOM also exhibited the highest corrosion rate during the salt fog (ASTM B117) exposure. The latter is due to exposure of the XHOM cut edge where only the plan surface was exposed during the electrochemical polarization measurements. A galvanic couple exists between the chromized coating (cathode) and steel substrate (anode) leading to rapid corrosion of the substrate when exposed. When the cut edge of XHOM is masked, the corrosion rate drops drastically, performing comparably to the highly ferritic stainless steels. During the salt fog (ASTM B117) exposure, pitting of XHOM and Type 409 was caused by cut edge corrosion leading to corrosion product migrating down the panel surfaces and initiating under deposit pitting. A singular pit was observed on the XHOM surface, which led to delamination of the coating surrounding the pit, caused by the galvanic couple at the coating substrate/interface once the substrate was penetrated. The overall corrosion resistance ranking of the materials in the external environment incorporating corrosion rate and pit depth is as follows: Type 436 ≈ XHOM Masked Edges ≈ Type 439 > Type 409Al > Type 409 > XHOM Edges Exposed. Strain was also found to have an effect on the localized corrosion susceptibility of XHOM in NaCl (aq), unlike Type 409, which exhibited no change. The influence of the drain hole manufacturing method (punching and drilling) on the corrosion susceptibility of XHOM and Type 409 was also measured. The punching method caused a smearing effect of the chromized coating, which served to partially cover and protect the cut edge. The main corrosion mechanism that occurred within the external environment is cut edge corrosion, which led to under deposit pitting.

Heat treatment of samples prior to testing in the internal exhaust environment led to an intermetallic phase change within the aluminized coating on Type 409Al, drastically reducing the

corrosion resistance of the material. An as-received aluminized Type 409 (Type 409Al-A) sample was tested in exhaust condensate exposure conditions to measure the difference in corrosion rate. XHOM with the cut edges exposed exhibited a corrosion rate comparable to Type 409 and heat treated aluminized Type 409, which is promising as XHOM already has an advantage in cost and formability. The overall corrosion resistance ranking of the materials exposed in the internal exhaust environment incorporating corrosion rate and pit depth is as follows: Type 409Al-A > Type 436 > Type 439 > Type 409 ≈ XHOM Edges Exposed ≈Type 409Al-H (heat-treated).

Acknowledgements

Lastly, this project is in the loving memory of my late brother Eyobell Emun. He was taken too soon, but I know he is watching over me and is proud of my accomplishments. From him I learned "If you're going to do something, just do it and enjoy it!", which is a lesson for all of us, not to complain about the little things in life.

Table of Contents

Table of Tables

Table of Figures

1. Introduction

The purpose of the automotive exhaust system is to reduce the noise and air pollution from the exhaust gas. It is comprised of two sections: the hot and cold end. The hot end is labelled as such due to the high temperatures reached during service, ranging from $650 - 750$ °C. The cold end operates over a larger range of temperatures reached in service, ranging from $100 - 650$ °C. From a corrosion performance perspective, each section contends with different corrosion modes: high temperature oxidation in the hot end, and localized (pitting) corrosion from both salt spray exposure (external) and exhaust condensate exposure (internal) as well as sensitization (formation of $Cr_{23}C_6$) in the cold end. Thus, corrosion-resistant materials are necessary to fabricate automotive exhaust components for both sections to ensure a long service life.

Automotive exhaust components are typically made from ferritic stainless steels, due to their high corrosion resistance (relative to carbon steel and aluminized carbon steel), low thermal expansion coefficient, and suitable mechanical properties [1]. Due to the different corrosion modes associated with each section, different grades of ferritic stainless steels are used including Type 409, 439, 436 and 441 (listed in order of increasing Cr content). Although the addition of the Cr content increases the corrosion resistance, it decreases formability and increases the cost. An alternative method to improve corrosion resistance, without incurring the large increase in cost associated with increased Cr contents, is to apply a metallic coating to a Cr-lean (less expensive) stainless steel such as Type 409, which provides galvanic protection. The most common coating used for this purpose is Al-10%Si, which is applied to Type 409 stainless steel through a hot-dip process resulting in a multi-layered material with increased corrosion resistance (surface performance) and unaffected formability (substrate performance) [2, 3]. One drawback to applying an Al-rich coating for corrosion control is the relatively low melting temperature: 600 °C for the Al-10%Si coating. Once the coating melts, the diffusion of Fe from the substrate into the coating is accelerated, which in turn accelerates the formation of Fe-Al intermetallic phases [4]. These

1

intermetallic phases are undesirable as they renders the coating more susceptible to corrosion. As a consequence of this drawback, "aluminized" (application of an Al-10%Si protective coating) Type 409 stainless steel is typically restricted to cold end components [4, 5].

From a maximum cost effectiveness and formability perspective, a different approach to applying a protective coating to a Cr-lean stainless steel substrate, is to apply a protective coating to a carbon steel substrate. Arcanum Alloys designed a process in which a Cr-rich slurry is applied to an uncoiled steel sheet, recoiled and annealed at 950 °C to create a chromized layer on both surfaces of an interstitial-free (IF) steel substrate. This multi-layered material (known as "XHOM") is currently used in the appliance industry to give the "stainless steel" appearance. XHOM has attracted interest from manufactures of automotive exhaust systems (Tenneco Automotive, in particular) as it possesses attractive benefits relative to the current generation of ferritic stainless steels used for fabrication. These include: (i) a corrosion-resistant surface layer that relies on the same protection principle as monolithic ferritic stainless steels with increased Cr content (formation of a protective Cr-rich oxide surface film), (ii) a protective surface layer that has high temperature stability (does not melt and has slow interdiffusion rates of Cr and Fe at the typical temperatures attained during operation) and (iii) formability that is dominated by the mechanical properties comparable to the IF steel substrate. So-called "chromizing" (application of a Cr diffusion coating) of steel for automotive exhaust components is not a new innovation. Chromizing of steel through pack cementation was invented in the 1920s, and investigated for automotive exhaust applications in 70s [6, 7]. This process ultimately was not plausible for an assembly line environment as temperatures above 1000 °C were required and the diffusion process ranged from 6-10 h [8]. As well economically, Cr-lean stainless steel become more popular such as Type 409 as no post processing was necessary on finished parts [9]. Now, with the coil arriving to manufactures already chromized, no processing is needed by the manufactures allowing this material to compete with ferritic stainless steels.

The overarching objective of the research study is to determine the suitability of XHOM as a candidate material from which to fabricate automotive exhaust applications, with a focus on the cold end components. Given the focus on the cold end section, the corrosion modes of interest include: localized (pitting) corrosion from salt spray exposure, acid condensate exposure and sensitization-induced Intergranular Corrosion. The suitability of XHOM is to be determined by gauging how the localized (pitting) corrosion resistance in both (external and internal) environments and sensitization susceptibility ranks relative to that exhibited by the current generation ferritic stainless steels [Types 409 (Fe-12Cr), 439 (Fe-17Cr) and 436 (Fe-17Cr-1Mo)] used to fabricate automotive exhaust systems.

One anticipated issue with the XHOM material is the expected accelerated corrosion that could occur at the cut edge that is exposed within drain holes in the muffler and perforations within the resonator. The accelerated corrosion in this case would be due to the galvanic couple that is exists between the more noble Cr-rich passive surface layer and the less noble IF steel substrate [10]. The localized corrosion susceptibility was determined through atmospheric-controlled cabinet tests in combination with electrochemical potentiodynamic polarization and immersion testing. Links between microstructure and corrosion susceptibility were determined using surface analysis spectroscopy techniques coupled with light optical and scanning electron microscopy (SEM) techniques.

This thesis includes six chapters including the Introduction as Chapter 1. Chapter 2 reviews the literature to provide an overview of automotive exhaust systems, key materials performance requirements and the localized corrosion and sensitization susceptibility of ferritic stainless steels, aluminized stainless steel and chromized steel in both the salt spray (external) and exhaust condensate (internal) relevant to the cold end section. Chapter 3 describes the experimental methods employed to determine the relative localized (pitting) corrosion and sensitization susceptibility of the XHOM material and current generation ferritic stainless steels. Chapter 4 presents the results and discussion of the corrosion testing conducted, the associated pre- and post-exposure material characterization that was

conducted and will discuss the experimental data presented. Chapter 5 will present a global discussion, on all the data and information given thus far in the thesis. Finally, Chapter 6 presents a set of major conclusions drawn from the analysis and interpretation of the experimental data collected.

2. Literature Review

2.1 Automotive Exhaust Systems: Materials Selection

As mentioned in the Introduction, the purpose of an automotive exhaust system is to reduce noise and exhaust gas pollution from the engine. Figure 1 shows a schematic of the major components of an exhaust system along with the exhaust gas and component temperatures expected during operation.
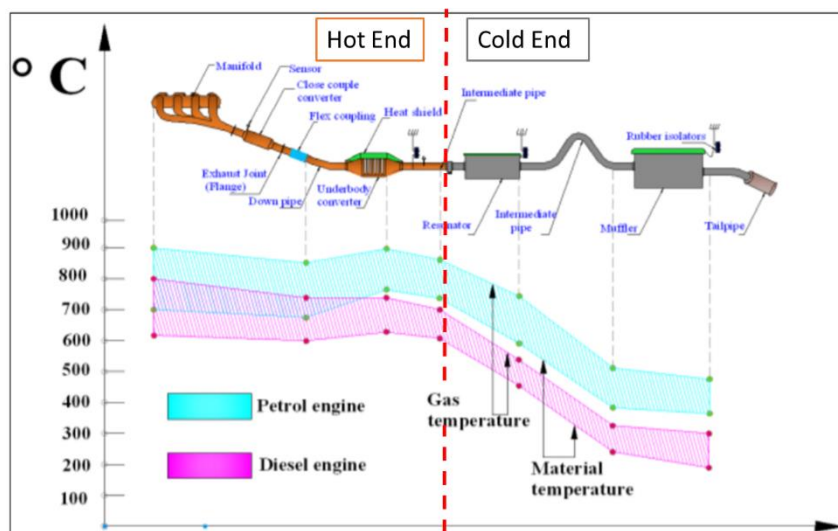
Figure 1: Exhaust system layout with temperatures reached during service [11]

This thesis concerns itself with the so-called cold end components, which includes the centre pipe, main muffler and tail pipe end, where the exhaust gas temperature ranges from 100 °C to 650 °C. A summary of the materials performance requirements for each of the major components is listed in Table I. Also listed are materials that typically are used to fabricate each of these major components given the required properties involved. Ferritic stainless steels are the materials of choice from which to

fabricate cold-end components since they exhibit a lower thermal expansion coefficient and cost

relative to austenitic stainless steel despite having lower high temperature mechanical properties.

Table I: Exhaust system components and current materials [1]

Component	Exhaust Manifold	Front Pipe	Flexible Pipe	Catalytic Converter		Center Pipe	Main Muffler	Tail end Pipe
				Shell	Catalyst Carrier			
	Hot End					**Cold End**		
Service Temperature (°C)	950 - 750	800 - 600			1000-1200	600-400	400-100	
Required Properties	- High temperature strength - Thermal fatigue life - Oxidation resistance	- High temperature strength -Thermal fatigue life - Oxidation resistance		-High temperature strength -High temperature salt corrosion resistance	- Oxidation resistance - Thermal shock resistance	- Salt corrosion resistance	- Corrosion resistance at inner surface - Corrosion resistance at outer surface	
Current Materials	Type 409L Type 430J1L Type 429 Type 444	Type 304		Type 409L Type 436J1L	SUH 21 20Cr-5Al Ceramics	Type 409L	Type 409L Type 409L-Al Type 436 Type 430J1L Type 436J1L	

Table II presents the major alloying elements (Cr % & Mo %), yield strength (YS), ultimate tensile

strength (UTS), formability (n & r) and maximum service temperature (°C). The properties n & r

represent the strain hardening exponent and the plastics strain ratio (drawability) [12], where maximum

service temperature is the temperature at which strength of the material begins to decline quickly [13].

Table II: Current generation ferritic stainless steel properties [14]

Type	Cr	Mo	Strength (MPa)		Formability		Max. T (°C)
	wt.%	wt.%	YS	UTS	N	r	
409	11.2	---	228	414	0.23	1.4	815
409Al	11.2	---	276	434	0.19	1.5	843
439	17.3	---	283	448	0.21	1.6	885
436L	17.3	1.3	317	483	0.20	1.3	885
441	17.9	---	310	483	0.20	1.4	950
444	18.5	2.0	360	515	---	---	1000

Ferritic stainless steels are composed of ferrite grains approximately 40 μm in size with secondary phase particles such as TiN, TiC, TiCN, and MnS distributed uniformly throughout the microstructure. As exhaust components reach a range of elevated temperatures during service, the microstructure is prone to abnormal grain growth. Abnormal grain growth can be detrimental because of its effect on mechanical properties. To address this issue, Ti is added to induce TiC/TiN formation. These particles pin the grain boundaries and, thus impede abnormal grain growth [15]. An image of a typical microstructure can be seen for a Fe-11Cr and Fe-17Cr alloy can be seen in Figure 2a and 2b. No difference can be seen in the microstructures illustrating the insignificance of Cr addition on microstructure, as Cr is a ferrite stabilizer.
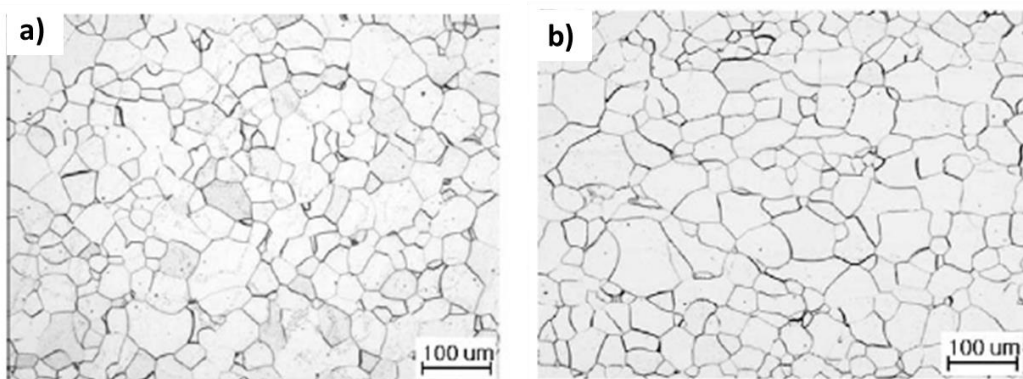
Figure 2: Ferritic stainless steel microstructure a) Fe-11Cr b) Fe-17Cr [16]

Aluminized carbon steel has been used for decades to build cold end exhaust components due to the increased corrosion resistance of the substrate provided by the Al barrier coating. The Al coating is applied through a hot dip process in which the steel is first heated in an oxidizing furnace to remove organic oils, then heated in a reducing furnace to reduce the oxide scale and finally dipped in Al-10%Si molten bath [17]. Si is added to reduce the formation of the brittle Fe-Al phases at the coating/metal interface [4] and to lower the melting temperature of molten bath from 660 °C to 600 °C.

Hot-dip aluminized ferritic stainless steel, particularly Type 409Al, has seen widespread use as a material of construction due the sacrificial anode cathodic protection of the Fe-11Cr substrate provided by the Al-rich coating [2], [3].

The low melting temperature of Al is a limitation that can restrict the utilization of aluminized materials. When exposed to temperatures above the melting temperature (600 °C), the Al-rich coating melts, which promotes the rapid diffusion of Fe from the substrate into the liquid coating. The increase in the Fe content then promotes the formation of brittle intermetallic Fe-Al phases including Al_2Fe_2Si (τ_1), Fe_2Al_5 (η) & $FeAl_2$ (ς). As each of these phases has a melting temperatures above 1000 °C, rapid solidification of the coating occurs, complete with significant cracking [4]. Cracks form during the re-solidification of the coating due to the different thermal expansion coefficient of the different intermetallic phases [4]. Through-thickness cracks are particularly problematic as they create a path for corrosive solutions to contact the underlying substrate with much less galvanic protection offered by the intermetallic phases than Al-10%Si coating. Heat treating aluminized steel/stainless steel above the melting temperature of the coating has been shown to significantly decrease the provided galvanic protection [5]. Table III and Figure 3, demonstrates the possible intermetallic phases that can occur during the solidification of the Fe-Al layer, depending on the time and temperature of heat treatment.

Table III: XRD analysis of phase formation in heat treated Al-Si coated steel [4]

No.	Phase	Formula	Al [wt%]	Si [wt%]	Fe [wt%]	T_{melt} [°C]
1	-	Al + Si	87	10	3	577
2	τ_5	Al_8FeSi	56	9	35	855
3	τ_1	Al_2Fe_2Si	32	13	55	1050
4	η/ς	$Fe_2Al_5/FeAl_2$	49	2	29	1156
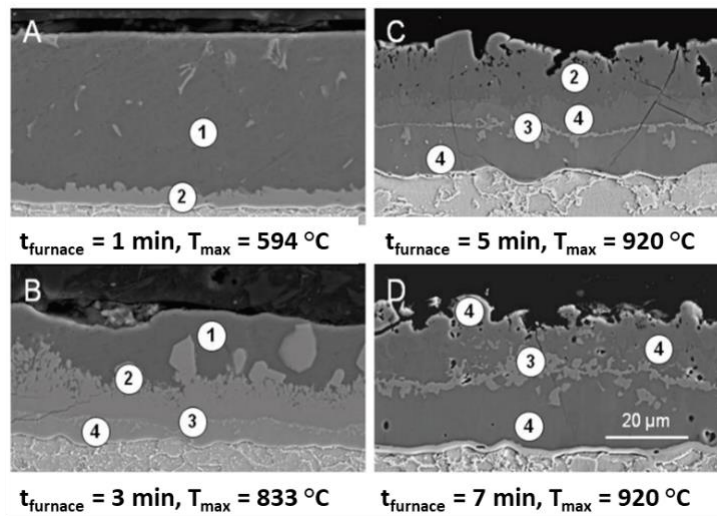
Figure 3: SEM images of heat treated Al-10%Si microstructure [4]

2.2 Localized Corrosion of Ferritic Stainless Steels

Stainless steels are well known for their relatively high aqueous corrosion resistance. This high corrosion resistance is due to the formation and maintenance of a protective (passive) oxide film that forms on the exposed surface. A very thin oxide layer 1-3 nm is formed when exposed to air, and once this film is formed the corrosion rate can be decreased by orders of magnitude, depending on the environmental conditions [18]. Localized corrosion involves breakdown of this passive film in localized areas due to the microgalvanic activity of cathodic/anodic precipitates, scratches/holidays in the passive

film, mechanical stresses and chemical attack by aggressive ions. Stainless steel is particularly prone to localized corrosion in halide (specifically chloride) environments [19].

Passive layers commonly have a chemical structure described by a bilayer model. According to this model, passive films contain an inner and outer layer. The inner layer (Cr_2O_3) plays the barrier role protecting against corrosion and the outer layer is either a hydroxide or oxy-hydroxide which behaves as an exchange layer between the metal surface and electrolyte [20]. The thickness of this passive layer is dependent on the bulk metal composition, pH of the electrolyte and the electrochemical potential. The composition of the bulk metal specifically the Cr content affects the thickness and corrosion resistance of the film. As Cr_2O_3 forms a thinner film than $Fe(OH)_3$, the more chromium present in the bulk the more Cr_2O_3 will form therefore producing a thinner overall passive film. Cr_2O_3 is more adherent to the metal surface, compared to the $Fe(OH)_3$ film which will break off exposing a fresh surface to the corrosive media.

Different methods for pit initiation have been reported, but the most accepted theory has been developed by MacDonald *et al*. known as the point defect model (PDM) [21]. Point defects, are assumed to be electrons, holes and metal/oxide vacancies. Aggressive anions such as Cl^- ions are believed to adsorb into the passive film creating a cationic vacancy. These vacancies then diffuse toward the metal surface and are annihilated by metal cations. If the flux of cationic vacancies is higher than the metal surface can annihilate, vacancies condense on the surface forming voids. These voids are an initiation site for localized corrosion to occur, therefore the higher the Cl^- concentration, the more cationic vacancies form leading to a higher density of voids [22]. Other theories discuss, the crystallinity of the passive oxide layer being susceptible to pitting at grain boundaries, as grain boundaries can exhibit ionic conductivities much larger than bulk oxide. In solutions without Cl^- ions, once the dissolution of the passive film occurs, repassivation initiates if sufficient OH^- ions adsorb to the exposed surface. Yet when Cl^- ions are present, a competition ensues with OH^- to adsorb on the surface and possibly impede

repassivation leading to stable pit growth [23]. Once stable pits grow in the presence of Cl^- ions, conditions are set such that pit growth is promoted. As the dissolution of Fe^{2+} ions, as well as the reduction of H_2O reducing to H^+ ions occurs, Cl^- ions electromigrate to the pit due to the charge imbalance. The formation of HCl (aq) within the pit lowers the pH of the pit environment, and the acidic chloride environment tends to propagate further pit growth [22].

Other factors that affect the corrosion resistance of stainless steel, include the crystallographic orientation of the grains, dislocation density and grain size. The influence of crystallographic orientations originates from the atomic densities, as a higher number of nearest neighbor atoms (high atomic density) requires a higher energy to break the bonds, and there is a reduction of the dissolution of atoms [24]. According to G. Lu *et al*. [25], strain can influence stainless steel by the formation and movement of dislocations leading to plastic deformation, as well as the formation of defects on the surface. An applied stress decreases the corrosion resistance of the cut edge by increasing the stored Gibbs energy, decreasing the electrochemical potential and, therefore increasing probability of dissolution, Equation 1 [26]. Equation 2, demonstrates the effect of dislocations on the donor density within the passive film. M represents metal, $V_{\ddot{O}}$ represents oxygen vacancy and T is defined as the dislocation formed at the metal/oxide interface. Hence, 1 mol of point defects (dislocations) forms (x/2) mols of vacancies, therefore the more dislocations created through applied strain, the more vacancies effecting the compactness of the passive film and, therefore the corrosion resistance [27]. According to the PDM, the more oxygen vacancies formed, the higher the chance of adsorption of Cl^- ions creating cationic vacancies. If a high enough flux of these cationic vacancies form, condensation on the metal/oxide interface leads to increased void formation. These voids can lead to fracturing of the passive film, behaving as pit initiation sites [21].

$$\Delta G = -Z * F \left(\frac{C}{mol} \right) * e(V) \quad (1)$$

$$M + T \rightarrow M_M + \frac{X}{2} V_{\ddot{O}} + Xe' \quad (2)$$
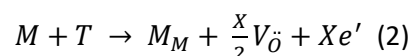
Tests were conducted on austenitic stainless steel, Type 304, measuring the corrosion rate with varying average grain sizes in 5% H_2SO_4 (aq). The results are shown in Figure 4a. A decrease in corrosion rate occurs as the grain size increases, which is caused by defects concentrated at the grain boundaries. As the grain size decreases, the grain boundary surface area increases resulting in more defects, destabilizing the passive film and lowering the intergranular resistance. Samples were also tested in 3.5% NaCl (aq), results shown in Figure 4b, which illustrate a different result in that decreasing the grain size decreases the pitting potential (E_b). This is due to a larger average grain size resulting in a lower pitting density, but deeper pits formed. In contrast, a smaller grain size results in a higher pitting density yet shallower pits. Therefore grain size can influence the corrosion rate positively or negatively depending on the surrounding environment [28].
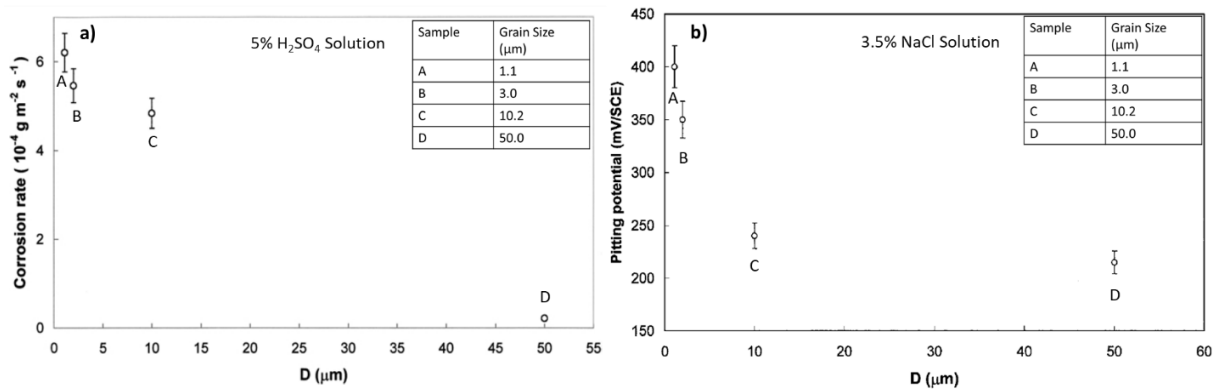
Figure 4: Plot comparing corrosion rate and average grain size a) 5% H_2SO_4 (aq) b) 3.5% NaCl (aq) [28]

To increase the localized corrosion resistance of a ferritic stainless steel, two main elements are used, Cr and Mo. Figure 5a and 5b reported by Horvath *et al*. [29], and Bond [30], demonstrate the increase in pitting potential achieved through the addition of Cr and Mo individually.
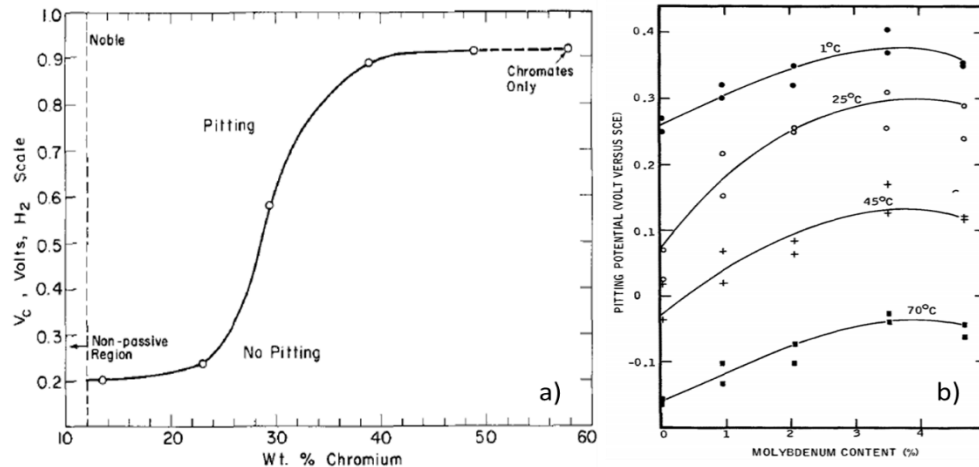
Figure 5: Graphic representation of effect of alloying elements on pitting potentials a) Influence of Cr addition on Fe-Cr alloy [29] b) Influence of Mo addition on Fe-18Cr alloy [30]

Authors debate over the reasoning behind the effect of Mo on the E_b. The current theories include Mo adsorbing on the surface film formed while in the active region forming molybdate or blocking active sites during active dissolution [22]. Mo has also been theorized to enhance the cation-selective properties of the passive film decreasing the amount of cationic vacancies [22]. Mo can also increase the nobility of a pit, decreasing pit current density, as well as has been suggested to counteract the effect of S by enriching the surface, bonding to adsorbed S and dissolving [22]. Yet the most accepted theory is Mo influences the E_b through dissolution and pit growth consideration [22]. The influence of temperature on the pitting potential of a Fe-Cr alloy is demonstrated in Figure 5b. The results illustrate a decrease in E_b and, therefore the corrosion resistance of a Fe-Cr alloy, with increasing temperature as ion transfer between the electrode and electrolyte is increased. The pitting resistance of stainless steels has been modeled by an equation, equating to a Pitting Resistance Equivalence Number (PREN), incorporating the elements which increase the E_b, Equation 3. Each element has a corresponding coefficient representing the influence it has on the E_b, normalized to the effect of Cr, which has a coefficient of 1 [31].

$$PREN = \%Cr + 3.3 \ x \ \%Mo + K\%N \ (3)$$

K has been reported to correspond to 16 and 30 [31]. Throughout this thesis, K is taken as 16. Equation 3 is commonly used for estimating the pitting resistance of austenitic and duplex stainless steels, as N is soluble in the austenite phase and not the ferrite phase. N, when in solid solution, has been reported to decrease the donor density and increase the Cr concentration in the passive film providing a more stable film with fewer defects increasing the corrosion resistance [19].

Preferred sites for pitting on the metal surface occurs at $(MnFe)S_x$ sulfides, which are nucleated during casting and difficult to avoid. The inclusion has been reported as electrochemically active and cathodic in a Fe-Cr matrix. Therefore, different authors have reported microcrevices caused by the dissolution of the MnS inclusion initiating pitting, as well as the accelerated dissolution of the near-by metal matrix. The size of and, therefore the impact of, the inclusion is dependent on precipitation, segregation, cold work and heat treatments [22]. Another secondary phase that behaves cathodically in the Fe-Cr matrix is TiN, which are more prevalent in ferritic stainless steels [32].

Oxy-hydroxide deposits or films can occur on metal surfaces leading to under-deposit pitting. Due to the film formed, occluded anodes become more frequent. An occluded anode is present underneath the deposit on the metal surface where the exterior surface of the deposit functions as the cathode. The mechanism of under deposit pitting is dependent on the conductivity of the oxy-hydroxide deposit. As iron oxides are electrically conductive, the outer surface behaves cathodically reducing dissolved oxygen as the deposit thickens. Through testing conducted by Suleiman *et al*. on Type 304, the influence of a rust layer on the corrosion resistance was measured. The results showed evidence that under deposit pitting behaves similar to crevice corrosion under a semi-permeable anion-selective deposit [33]. Though the rust layer behaves similar to a crevice, the ionic resistance is much lower than a conventional crevice, permitting rapid propagation of localized corrosion, even in dilute media [33]. Even though corrosion is localized under the deposit, pits differ in shape from the deep and narrow pits commonly found in stainless steels [34].

2.3 Intergranular Corrosion

Intergranular corrosion (IGC) is an attack of grain boundaries due to a galvanic couple typically created by a depletion of an element or reactive impurity segregation at the grain boundary [34]. The most common form of IGC occurs when ferritic stainless steels are heat treated in the range of 425 °C to 815 °C forming Cr-rich carbides or nitrides at the grain boundaries, depleting the adjacent matrix in Cr [16, 35]. Above 815 °C Cr-rich carbides are soluble, and below 415 °C the diffusion rate of C is too low to form carbides [34]. This altered microstructure is known as a sensitized microstructure, meaning it is susceptible to intergranular attack due to galvanic couple created between the grain boundary and adjacent Cr- depleted matrix [16, 35, 36, 37]. Figure 6 shows an elemental line scan across the grain boundary of a Fe-Cr alloy containing a Cr-rich carbide precipitate particle acquired using x-ray energy dispersive spectroscopy (EDS). The bulk Cr content of the grains adjacent to the boundary is 18%. The content decreases to a value of less than 10% as the boundary is approached, which is less than the critical Cr content of 10.5% required for "stainless" classification. The Cr content increases significantly as the Cr-rich carbide precipitate particles itself are traversed. The stoichiometry Cr/C ratio in the precipitate ($M_{23}C_6$) is very high, which makes Cr-rich carbide formation especially dangerous, as nearly four times more Cr is lost from the matrix to the precipitate particle than C.
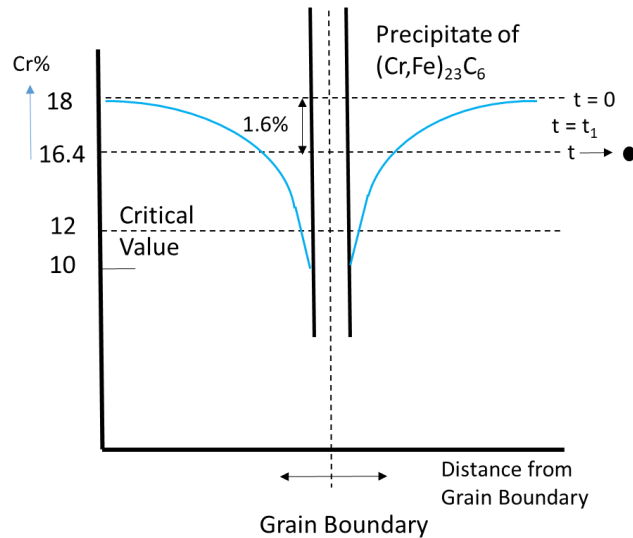
Figure 6: EDX linescan through Cr-rich $M_{23}C_6$ carbide containing grain boundary

In oxidizing conditions Cr-rich carbides behave inertly, yet the Cr depleted zone adjacent to the grain boundary is electrochemically active relative to the adjacent Cr-rich matrix. This results in a microscopic galvanic attack with the Cr-depleted zone serving as the anode and Cr-rich matrix serving as the cathode. Methods to decrease the susceptibility of IGC include decreasing the C content of the alloy, avoiding thermal heat treatments in stated temperature range and adding carbide stabilizing elements such as Ti and/or Nb to preferentially form carbide precipitates [16] [35].

Certain elements that are added to increase the corrosion resistance of stainless steel can have secondary effects, which alter the materials susceptibility to IGC. Mo, which is added to increase the pitting corrosion resistance can form carbides (MoC) at the grain boundary similar to Cr. This depletion of Mo will contribute to a galvanic couple between the depleted grain boundary and the matrix inducing IGC [34].

The solubility of N in austenite is very high and, therefore N does not precipitate as nitrides, yet in ferrite solubility is relatively low. Consequently, CrN can also precipitate at grain boundaries and serve to increase IGC susceptibility [34].

One popular method of determining the degree of sensitization (DOS) of stainless steel is the so called double loop electrokinetic potentiodynamic reactivation (DLEPR) test. This method involves anodically polarizing a working electrode in dilute H_2SO_4 (aq) measuring the ratio of the critical current density required to passivate, as measured during the activation (forward) scan (i_a), and depassivate, as measured during the reactivation (reverse) scan (i_r). If this ratio (i_r/i_a) is above 1%, the stainless steel is considered to be sensitized [35, 36, 37]. A schematic example of a non-sensitized DL-EPR curve is shown in Figure 7a, while Figure 7b shows a sensitized DLEPR schematic, and a typical DLEPR curve for Type 409 is shown in Figure 7c.
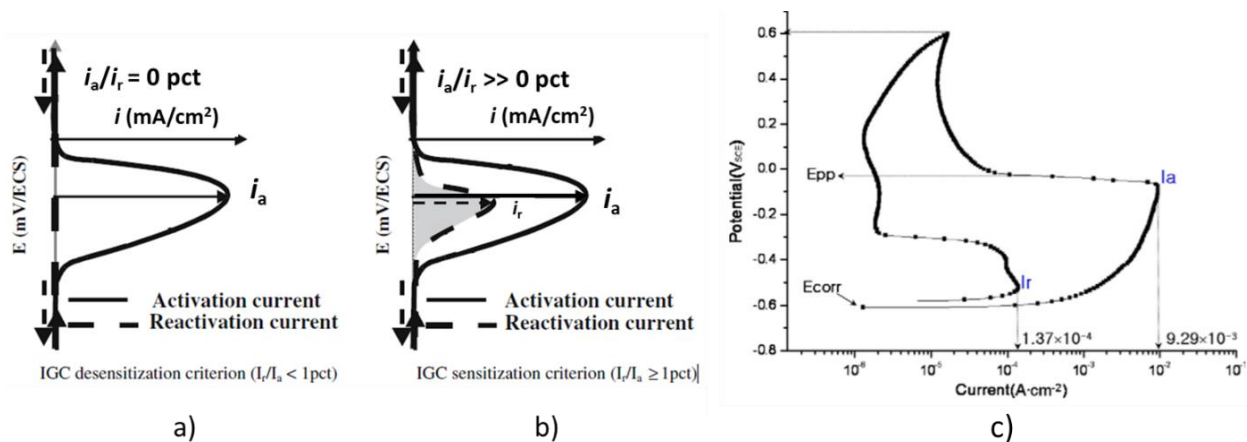
Figure 7: DL-EPR curves diagram: a) Desensitized material b) Sensitized material [38] c) DLEPR curve Type 409 [39]

Cold end components reach temperatures ranging from ambient air to 650 °C, which overlaps with the temperature range in which ferritic stainless steels are susceptible to sensitization. The ferritic stainless steels used to manufacture exhaust components are designed with a Ti safety factor to ensure IGC is impeded. A minimum amount of Ti $\geq$ 6 × %C is the ASTM requirement [40], yet commonly Ti concentration of up to 40 x (%C + %N) have been used as an attempt to ensure sensitization does not occur. I.A. Franson *et al*. [41], tested over 30 Type 409 samples with varying Ti, Nb, C and N contents all which met the ASTM requirement of Ti ≥ 6 × %C . Each of the samples were arc welded, pickled and immersed in a solution of boiling 0.5% H_2SO_4 (aq) + 6% $CuSO_4$ (aq) + Cu (s) shots for 20 h. The samples

were then cut in cross-section analyzing the grain boundary attack, denoting severely attacked samples as "IG attack", shallow grain boundary grooving as "Grooved GB" and unaffected samples as "Pass". The results were then plotted as shown in Figure 8. A line was drawn separating the "Pass" samples and attacked samples, revealing a pattern. This plot proves the ASTM requirement of alloying elements is insufficient as it does not include the sensitization contribution of N, hence why I.A. Franson *et al*. [41], calculated a new stabilization requirement, extrapolating from the plot Figure 8. Either **%Ti or (%Ti & %Cb) = 0.08 + 8 × (%C + %N).**
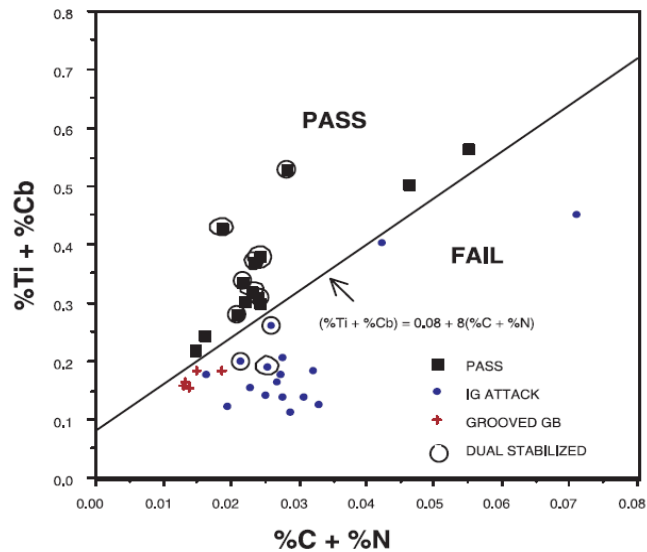
Figure 8: Plot comparing (%TI + %Nb) and (%C + %N) content of Type 409 alloys testing sensitization susceptibility [41]

Ti is very commonly added to stainless steels for the purpose of pinning grain boundaries impeding abnormal grain growth. In stainless steels, Ti is also used to react with any free C or N impeding $M_{23}C_6$ or MN formation, as this could induce IGC. The difference in size between TiN and TiC precipitates can be explained by the different temperatures in which precipitation occurs. TiN precipitate at approximately 1300 °C compared to TiC, which precipitates at 850 °C therefore allowing more time for growth of TiN [42]. These TiC/TiN precipitates form on or adjacent to grain boundaries, subboundaries and the fusion line. The attack at the grain boundaries is caused by the microgalvanic corrosion associated with

concentrated areas of TiN/TiC precipitates. Temperatures above the sensitization range of 425 °C to 815 °C induce IGC through the precipitation of TiC and TiN, which form at 850 °C and above [32]. Figure 9a below shows a Time-Temperature-Sensitization diagram for Type 409, demonstrating that there are two temperature ranges in which sensitization can occur. Figure 9b plots the sensitization susceptibility (i_r/i_a) results of Type 409 heat treated to multiple temperatures. The results of this plot confirm the sensitization temperature ranges shown in Figure 9a.
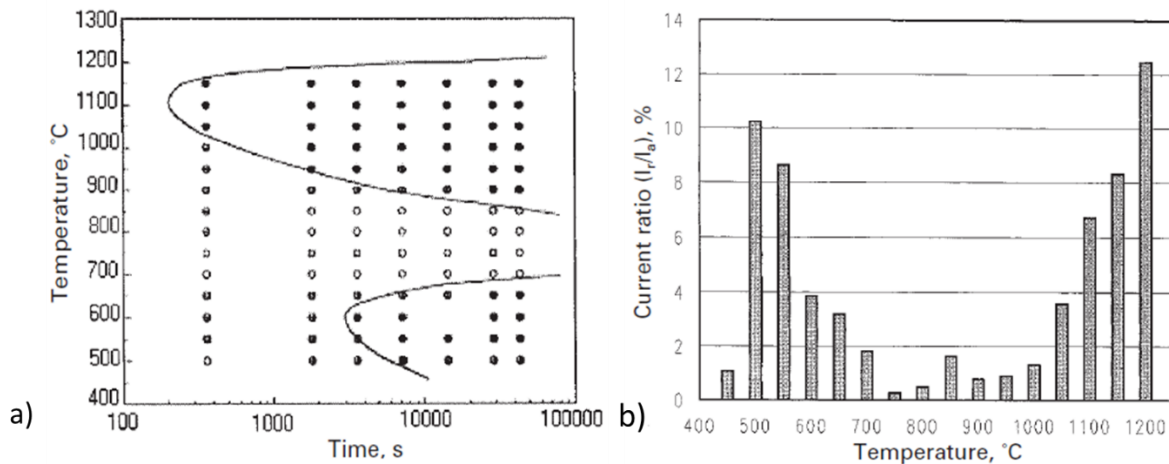
Figure 9: a) Time-Temperature-Sensitization diagram for Type 409 b) i_r/i_a ratio plotted against heat treatment temperature for Type 409 [32]

2.4 External Corrosion Performance

Due to the use of de-icing salts, chloride salts are bountiful on the roads during the winter months causing dominantly pitting corrosion of cold end components. Geography and climate are important to this form of corrosion as areas that are warm year round (not using de-icing salts) and inland, far from sea water do not experience this corrosion mode [43]. De-icing salts such as $CaCl_2$ and $MgCl_2$, which have lower freezing temperatures than NaCl, are commonly used for this purpose [44].

Localized external corrosion is a result of the combination of moisture, road debris and related external corrosion sources (road de-icing salt solutions, etc.) that becomes entrapped in various locations along the exhaust system [43]. Unlike internal exhaust condensate corrosion, external salt

corrosion does not depend on vehicle or engine operating conditions, localized corrosion continues after the automobile is turned off [43].

Commonly, only limited regions are affected by enhanced metal attack and penetration due to the formation of corrosion concentration cell on the surface. A concentration cell occurs when moisture reacts with the abundant NaCl creating a Cl-rich "drop" of water on the surface of exhaust components, behaving similar to the Evans Water Drop Experiment [34, 45]. Areas near the edge of the drop with abundant access to oxygen function as the cathode. The metal surface at the center of the drop has the least amount of access to dissolved oxygen as dissolved oxygen needs to diffuses through the volume of the drop, replenishing oxygen initially lost to the corrosion of the metallic surface. Therefore, there is a continuous deficit of dissolved oxygen at the metal surface ensuring the surface continues to function as the anode [34, 45]. Equation 4 and 5 demonstrate the anodic and cathodic half-cell reactions occurring in the drop

$$Fe_{(s)} \rightarrow Fe^{2+}{}_{(aq)} + 2e^- \quad (4)$$

$$O_{2\,(g)} + 2\,H_2O_{(l)} + 4e^- \rightarrow 4\,OH^-{}_{(aq)} \quad (5)$$
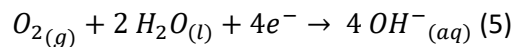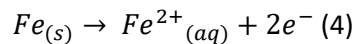
The constant changing temperature of the exhaust components and ambient air has an effect on the localized corrosion rate. As high temperatures are reached, the corrosion rate is increased due to increased rate of ion transfer, yet if the surface reaches a critical temperature, moisture is evaporated and, thus the corrosion rate is decreased. Once the temperature begins to cool down, moisture is restored and the concentration cell re-starts to corrode the material [43]. Therefore, whilst driving the automobile, salt corrosion does not affect hot end components. Only the tail pipe tends to experience a low enough temperature during service to maintain the required moisture content for concentration cell corrosion of the exterior surface to occur.

Type 409 has been tested against higher alloyed stainless steels in a NaCl-rich environment simulating the exterior environment. The chemical composition for each alloy is presented in Table IV.

The samples were heat treated at 650 °C for 1 h in air, followed by naturally cooling in air, and finally

exposed per ASTM B117 to 5% NaCl salt spray at 35 °C for 24 hours before cooling to room temperature,

completing the cycle. The results in Table IV, display the results after 100 cycles, showing that the best

results pertain to alloys with Mo present. The decrease in weight change, is expected as the PREN values

increase, signifying an increase in localized corrosion resistance.

Table IV: Alloy compositions and modified ASTM B117 weight change results [41]

	Typical Composition, Weight Percent			Weight Change (%)
Alloy (PREN)	Cr	Mo	Ni	Post 100 Cycles
Type 409 (11)	11	-	-	-57.4
Type 439 (18)	18	-	-	-28.9
Type 444 (24.6)	18	2	-	-8.1

A similar test was run at AK Steel, testing the corrosion resistance of Type 409 against a higher alloyed

ferritic stainless steel (Type 439) and aluminized ferritic stainless steels ("Aluminized-409" and

"Aluminized-439") in an exterior exhaust environment. Table V, presents the procedure and test results

can be seen in Figure 10.

Table V: Simulation of external exhaust environment procedure [46]

Steps	Procedure
1	Heat to 316 °C for 1 h (Monday Only)
2	Daily Dip 15 min. – 5% NaCl
3	Air Dry
4	Humidity – 85% RH, 60 °C
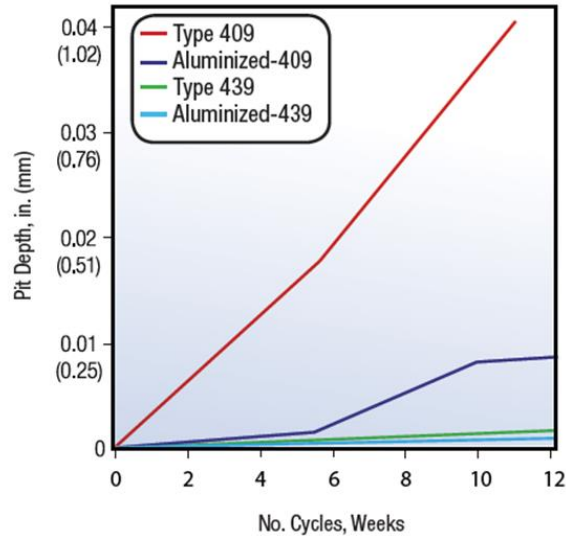
Figure 10: Results of exterior exhaust environment exposure test of untreated and aluminized ferritic stainless steels. [46]

Figure 10 demonstrates the positive influence of Cr and the effectiveness of an aluminized layer on the corrosion resistance of ferritic stainless steels in a Cl^--rich environment. The pit depth of Aluminized 409 drastically increased after week 6, due to the consumption of aluminized layer exposing the bare Cr-lean Type 409. This decrease in effectiveness is not seen in aluminized Type 439, due to consumption of the aluminized layer not affecting the corrosion resistance of the bare Type 439 in a Cl^--rich environment. An interesting result is that bare Type 439 outperformed Aluminized-409, signifying that increasing the Cr content is the more efficient method to increase the corrosion resistance, barring the increase in weight.

As different road salts have begun to be used, Type 409 and 439 samples were tested by Beom *et al.* [44] in both a NaCl (aq) and $CaCl_2$ (aq) solution, to measure the influence of both on the corrosion resistance of a low and highly alloyed ferritic stainless steel. The pH was measured for both solutions as the Cl^- concentration was increased from 5% to 30%, and it gradually decreased from 7.6 to 7.3 for NaCl (aq), yet it decreased from 7.2 to 6.0 for $CaCl_2$ (aq). As can be seen in Figure 11a and 11b, with the same

Cl⁻ concentration both samples exhibit a lower E_b in CaCl₂ (aq). This is caused by the increased acidity and corrosiveness of CaCl₂ (aq) compared to the NaCl (aq).
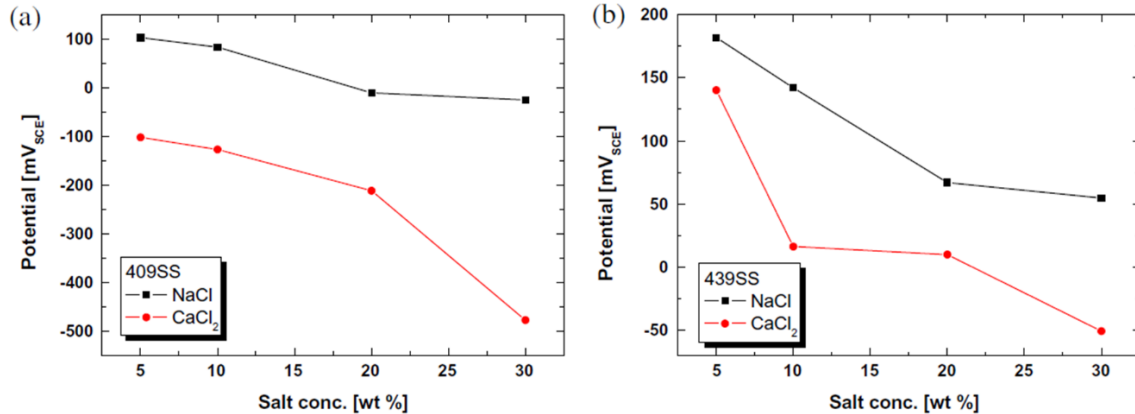
Figure 11: E_b of Type 409 and 439 polarized in a) 5% NaCl b) 5% CaCl₂ [44]

2.5 Internal Corrosion Performance

Internal exhaust condensate forms a solution containing different strong acids, which if left stagnant on exhaust components, can lead to general corrosion or localized corrosion. As exhaust gas is being removed, it begins to cool down before leaving the tail pipe [43]. During this cool down period, water vapor will react with acidic compounds forming an acidic gas, eventually condensing into an acidic solution. These compounds include, $SO_{x\ (g)}$ to make sulphuric acid and $NO_{x\ (g)}$ to make nitric acid [47].

Figure 12 plots the weight loss results of Type 409 against a higher alloyed ferritic stainless steel (Type 439) in a simulated exhaust system condensate solution containing 1000 ppm Cl⁻, 2000 ppm CO^{2-}_3, 3740 ppm NH^+_4, 5000 ppm SO^{2-}_4 and 100 ppm NO^-_3. The difference in Cr concentration has a clear influence on the corrosion resistance due to exhaust gas condensate, as time passes. The first ten cycles don't show an excessive difference in weight loss value, but after 20 cycles there is a clear difference between Type 409 and Type 439.

Table VI: Simulation of internal exhaust environment procedure

Steps	Procedure
1	Sample immersed in 100 mL of condensate solution
2	Heat from ambient Temp. to 250 °C in 1 h
3	Hold at 250 °C for 2 h
4	Cool to ambient Temp. over 3 h
5	As only solid residue remains from original test cycle Add 100 mL to beaker and repeat cycle
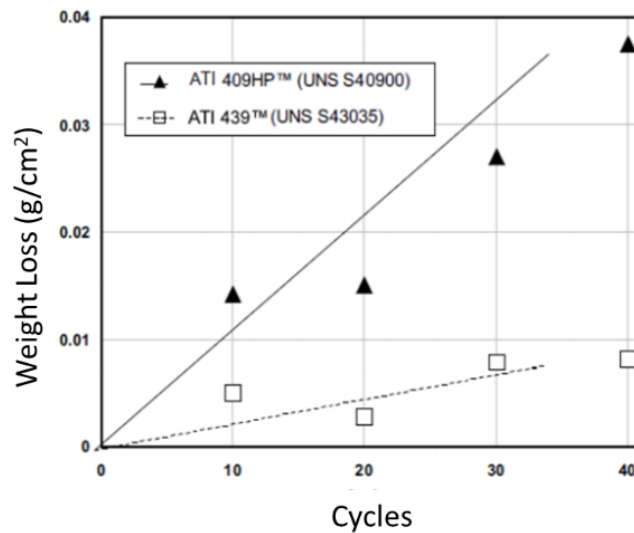
Figure 12: Exhaust gas condensate exposure test results [48]

Tests were also conducted at AK Steel, comparing ferritic stainless steels in an internal exhaust gas

condensate simulated solution. Table VI presents the procedure and the results from this can be seen in

Figure 13. This test compares untreated Cr-lean stainless steels (Type 409), highly alloyed stainless steels

(Type 436, 439) and aluminized stainless steels (Aluminized-409, Aluminized-439).
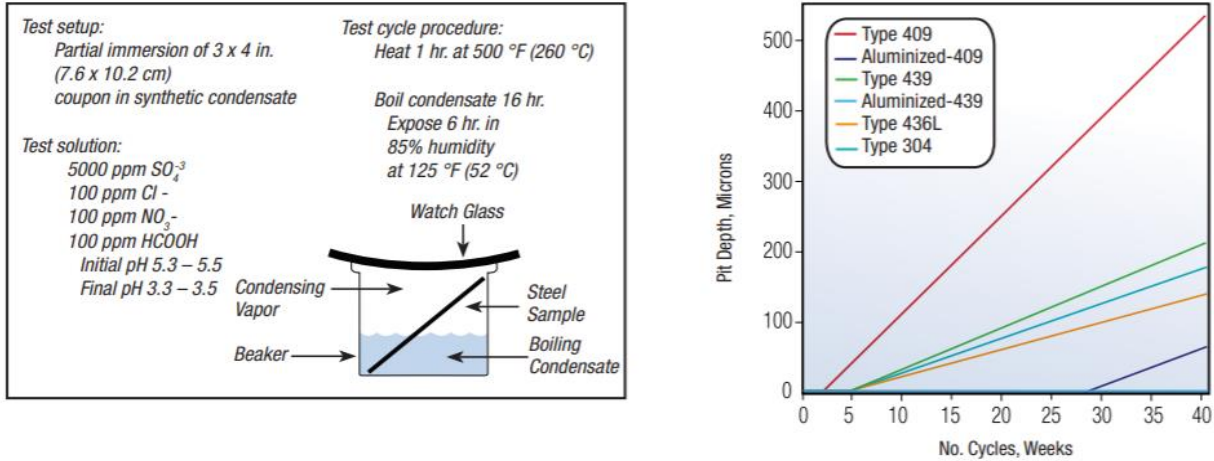
Figure 13: Procedure and results of internal exhaust gas condensate exposure test comparing untreated and aluminized ferritic stainless steels [46]

The results shown in Figure 13 suggest that an aluminized layer is highly effective in protecting the ferritic stainless steel substrate in an exhaust gas condensate solution, outperforming highly alloyed ferritic and austenitic stainless steels.

Testing conducted by Nippon steel compared the corrosion performance of bare Fe-11Cr, aluminized Fe-11Cr and aluminized carbon steel when exposed in a cyclic acid condensate exposure simulating an internal automotive exhaust environment. The cyclic test procedure is listed in Table VII.

Table VII: Muffler exhaust environment surface corrosion test method. Solution: 1100 ppm SO_4^{2-}, 150 ppm NO_3^-, 3000 ppm NH_4^+, 300 ppm Cl^-, 4000 ppm CO_3^{2-}, 1000 ppm CH_2O_2 and 1000 ppm CH_3COOH [2]

Cycle steps	1 week = 1 complete cycle
1	Two cycles of heating (300 °C), 2/3 immersion (pH 8, 80 °C, 150 min.)
2	Drying (100 °C, 24 h)
3	2/3 immersion (pH 3, 80 °C, 24 h)
4	Drying (100 °C, 24 h)
5	2/3 immersion (pH 3, 80 °C, 24 h)
6	Drying at room temperature (27 °C, 66 h)
Test Period	20 weeks

Figure 14 demonstrates the difference in corrosion observed after testing in the in the cyclic acid condensate exposure. Figure 14 clearly shows the beneficial effect of the aluminized coating on corrosion resistance of bare stainless steel. The coating behaves as a barrier coating protecting the carbon steel surface, yet the edges are unprotected and corrode rapidly leading to the high corrosion rate of aluminized carbon steel. The edges of aluminized Fe-11Cr are also exposed, yet are more resistant to corrosion firstly due to the Cr-rich oxide passive layer present on the surface and secondly due to the galvanic protection provided by the Al-10%Si coating. Bare Fe-11Cr showed no evidence of general corrosion, but reduction of the section thickness occurred due to pitting corrosion. Figure 14 also demonstrates the attractiveness of aluminized 11%Cr stainless steel, as it performs comparably to the highly alloyed stainless steels at a lower cost.
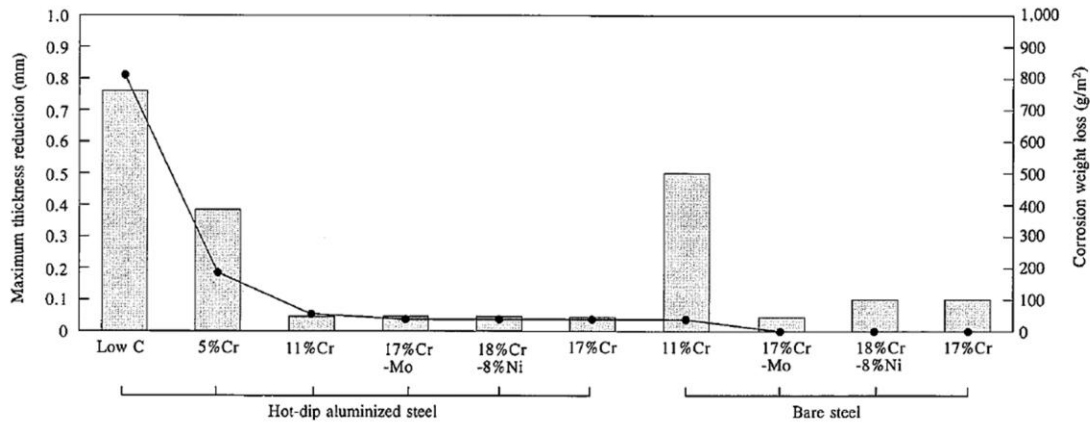
Figure 14: Results of muffler interior surface corrosion test [2]

2.6 Chromizing

Chromized steel is a carbon steel substrate with a Cr-rich layer/coating applied on the surface and has been investigated for many years dating back to the 1920s [49]. Interest in using chromized steel to build automotive exhaust components dates back to the 1960s [6, 7]. Chromizing can be achieved by several methods including electrodeposition, chemical vapour deposition vacuum powder-coating and pack cementation [49].

The pack cementation method of applying a Cr-rich surface layer to carbon steel, which is of particular interest to the research conducted for this thesis, was first reported by Kelley in 1923 [49], yet a major disadvantage was the high temperature of 1300 °C required. Weber and Marshall were able to overcome this problem by introducing a halogen carrier compound [49]. The compound provides a volatile source of Cr at the substrate surface, which required a lower temperature (as low as 1000 °C). Pack cementation consists of a pack of powders comprised of ferro-chrome powder mixed with inert filler (Al_2O_3), and an activator (NH_4Cl) [49, 50, 51]. Once the pack is created and the steel substrate is immersed in the pack, it is placed in the furnace and raised to a temperature dependent on the desired coating thickness usually ranging from 800 °C- 1200 °C. The environment consists of a gaseous mixture of H_2 and HCl, which promote reactions that provide the required volatile Cr compound at the substrate surface according to the following simplified reaction sequence (Equations 6-9) [51].

$$NH_4Cl_{(s)} \rightarrow NH_4Cl_{(g)} \rightarrow NH_{3(g)} + HCl_{(g)} \quad (6)$$

$$2NH_{3(g)} \rightarrow N_{2(g)} + 3H_{2(g)} \quad\quad\quad (7)$$

$$2HCl_{(g)} + Cr_{(s)} \rightarrow CrCl_{2(l)} + H_{2(g)} \quad\quad (8)$$

$$CrCl_{x(g)} + \frac{1}{2}x\,H_{2_{(g)}} \rightarrow Cr_{(s)} + HCl_{(g)} \quad\quad (9)$$
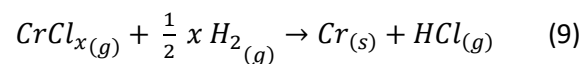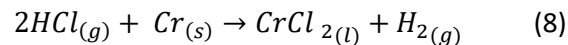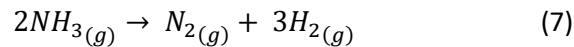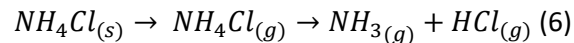
During the heating process the NH_4Cl is evaporated into a gas and decomposed into NH_3 and HCl, Equation (6). NH_3 is then decomposed into N_2 and H_2, Equation (7), whereas HCl reacts with the Cr powder to create the volatile $CrCl_x$ gas, Equation (8). $CrCl_x$ gas then reacts with H_2 to create solid Cr, which is then deposited onto and diffused into the steel substrate, Equation (9). The chromized coating consists of a granular structure that also contains Cr-rich carbides (($Cr,Fe)C_x$ and $M_{23}C_6$) , Al_2O_3 and pores [51].

The Fe-Cr phase diagram in Figure 15a displays the change in phase that occurs during the diffusion of Cr into the steel substrate. With a large Cr content at the surface of the substrate, the stable phase present in the microstructure at a typical diffusion temperature (800 °C- 1200 °C) is ferrite, due to the ferrite-stabilizing Cr. Cr diffusion profiles are shown in Figure 15b, demonstrating that even though there may be a difference in coating thickness, the change in diffusion rate always occurs at approximately 12%. This abrupt change in the profile is consistent with the predicted change in the stable phase from (Fe, Cr) ferrite to austenite and the associated order of magnitude difference in the Cr diffusion rate in the two phases:

a)   b)
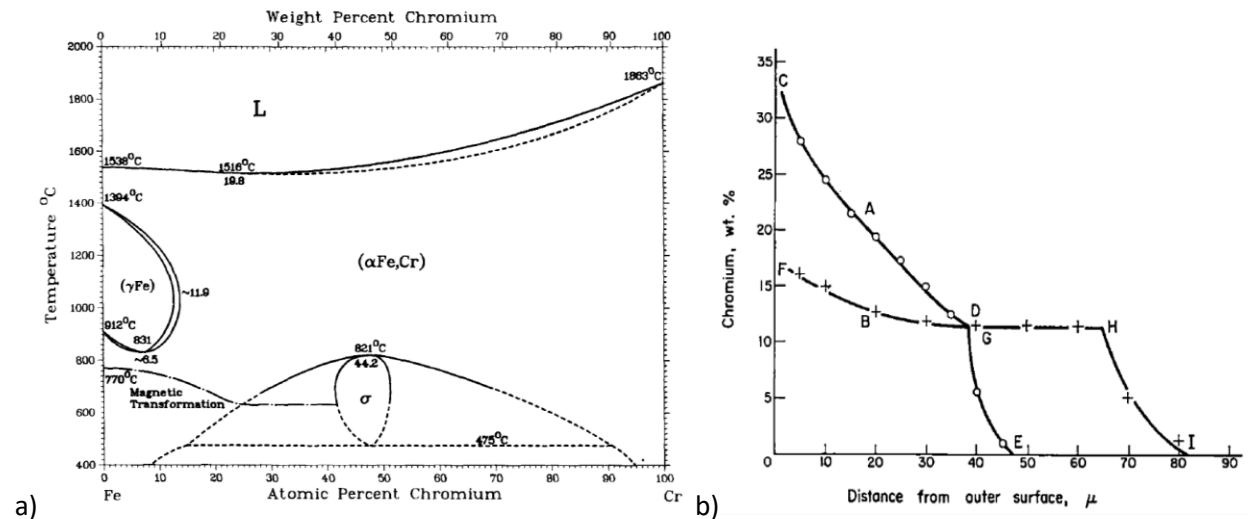
Figure 15: a) Fe-Cr Phase diagram [52] b) Cr diffusion profile through chromized steel before and after 18 h heat treatment at 950 °C [50]

C in the steel substrate can affect the formation (extent) of a chromized surface layer in two important ways. First, the tendency for C to diffuse out of the steel surface (into the environment) produces a decarburized layer, which forms at the substrate surface. Second, a carbide layer tends to form on the surface, which serves as an effective barrier to Cr diffusion. The addition of carbide forming elements such as Ti, Nb, Mo and V serve to reduce C activity, limiting the formation of a surface carbide

layer. Other elements present in the steel substrate that can affect the chromizing process include S and P, which can influence the formation of the coating by altering the rate of diffusion or modifying surface reactions [49].
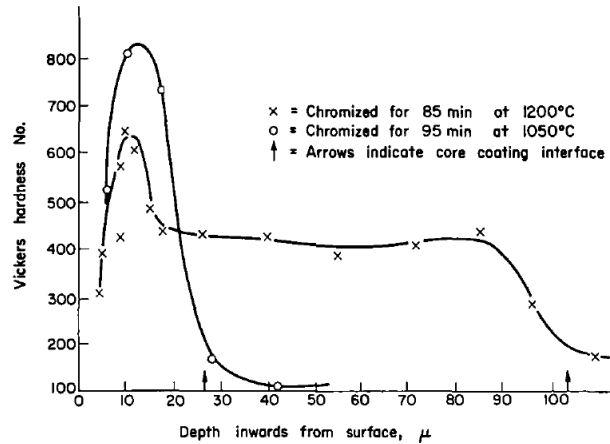
Figure 16: Hardness measurements across chromized coating [50]

Figure 16 shows the effect of process parameters on the resultant micro hardness and thickness of a chromized layer applied on a carbon steel substrate [50]. The different coating temperatures 1200 °C and 1050 °C result in different hardness and thickness values. The sample heat treated to 1050 °C, has a thinner coating due to the lower temperature causing a shorter diffusion length. Due to Cr not diffusing as far, a higher concentration of Cr is retained near the surface resulting in higher hardness values. An interesting aspect of these profiles is the initial increase in micro hardness near the surface of the coating. It was concluded that this increase is due to localized yielding of the coating near the surface.

Blandy Jr, [10] measured the corrosion resistance of chromized steel for 820 h fully immersed in a muffler condensate solution heated to 85 °C and concluded that the chromized steel performs comparably to that of Type 409 (Fe-11% Cr), as shown in Figure 17. The cut edges of chromized steel are assumed to be protected during immersion as cut edge corrosion does not seem apparent in the as-tested condition.
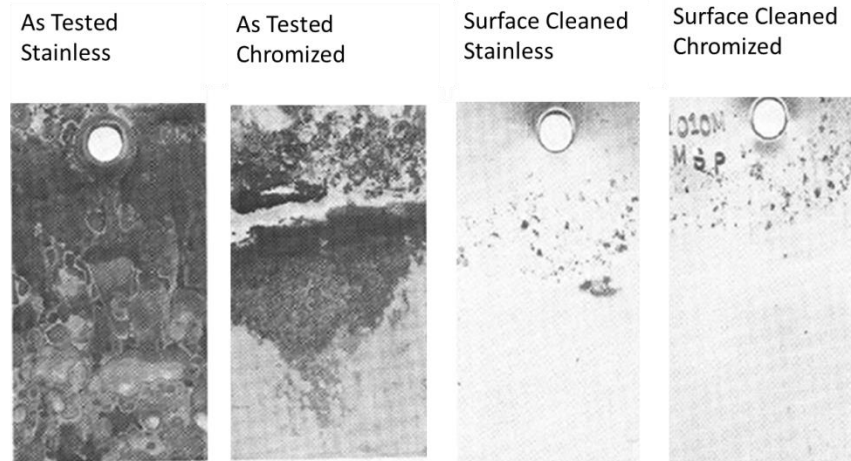
Figure 17: Chromized steel and Fe-11Cr Alloy post 820 h immersion in exhaust condensate solution [10]

To determine the corrosion resistance of chromized steel in a real-life application, chromized mufflers were tested by assembling mufflers on a vehicle for 5 years. Due to the cathodic nature of the noble ferritic stainless steel coating, the steel substrate is subject to galvanic corrosion when the cut edge is exposed. Yet corrosion of the unprotected edge perforations in the muffler were confined to a thousandth of an inch (25 μm). The corrosion products that formed between the layers restricted further attack, behaving as a plug blocking the corrosive solution from contacting the steel substrate, impeding further corrosion [10].

Arcanum Alloys has patented a novel way of chromizing steel, which involves chromizing an entire coil of steel rather than of pre-manufactured components. This method allows the fabrication of exhaust components from a pre-chromized sheet metal. This process is advantageous because it requires no extra steps by exhaust manufacturers and does not affect the already in place assembly line. This process includes the application of a Cr-rich slurry on one surface of an uncoiled steel sheet, which is then re-coiled and annealed to induce diffusion, creating a stainless steel coating. The slurry is a solution containing a solid and liquid phase, comprised of an alloying agent (Cr), a solvent (H_2O), an inert species (Al_2O_3) and an activator (NH_4Cl) [53]. Halide activators are selected depending on their

contribution to the green strength, as the slurry-coated substrate needs to withstand handling and/or machining before fully cured. The alloying agent may have a particle size of 100 μm or smaller where the inert species may have a particle size of 75 μm or smaller. The purpose of the inert species is to control the viscosity of the slurry, preventing the alloying agent from dropping out of suspension as well as preventing "stickers" from forming during annealing [53]. Stickers are regions on the coil, pressure welded to adjacent bare metal through a sintering process. These regions require an uncoiling force exceeding the yield strength of the material, leading to kinks formed on the surface due to plastic deformation [54]. The slurry is applied to the substrate by roll coaters. First, the steel coil is uncoiled and then fed through the roll coaters. The steel may be fed through roll coaters multiple times to achieve the desired thickness of slurry; different slurry formulations can also be used during the multiple passes through roll coaters, as well as different coating patterns. After the slurry is applied the solvent is evaporated by heating the coil, and then the coated steel is re-coiled. Gaseous HCl is mixed in with the annealing gas to prevent loss of the activator in the slurry during annealing. Minimizing the partial pressure of the activator at high temperatures, maintains a low deposition rate essential to preventing Kirkendall voids. The annealing temperature may range from 800 °C – 1300 °C, and the annealing time may range from 5 h – 200 h depending on coating thickness requirements [53]. Figure 18 demonstrates an example of a possible surface finish, appearing striated with light and dark bands. The light bands correspond to regions containing Cr-rich carbides and the dark bands correspond to regions free of Cr-rich carbides. The surface finish is dependent on the substrate composition, specifically the concentration of elements such as C. This striation pattern is caused by C migrating from the substrate to the surface layer during annealing and forming a carbide layer.
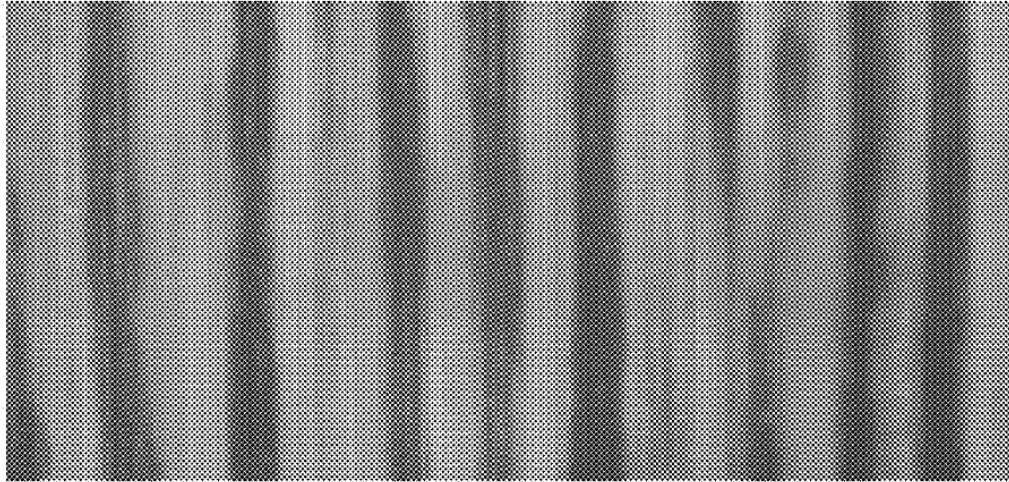
Figure 18: Striation pattern on chromized steel demonstrating light regions (with chromium carbides) and dark regions (without chromium carbides) [53]
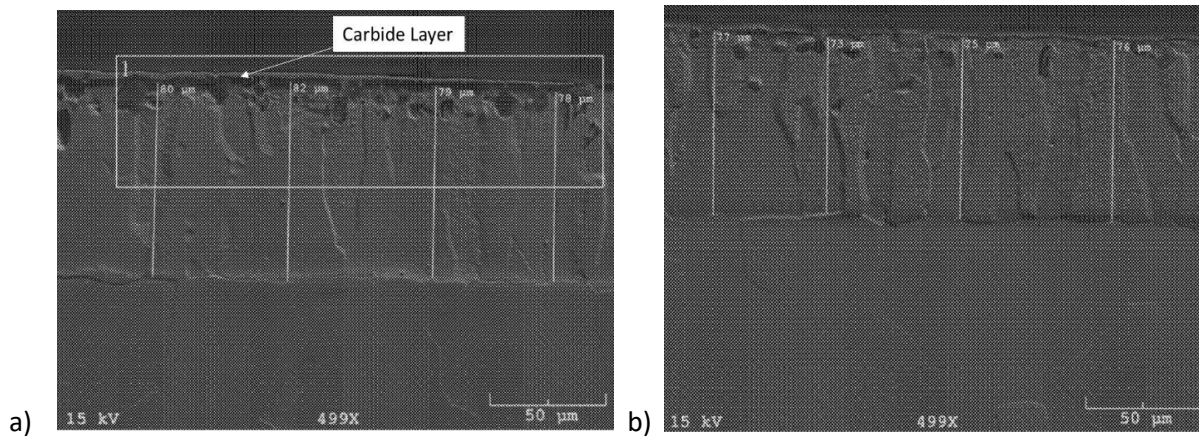
Figure 19: Cross section of chromized coating a) with chromium-rich carbide layer present b) without chromium-rich carbide layer [53]

The carbide layer is shown in Figure 19a, representing the lighter region on striated surface finish and Figure 19b represents the darker region on the striated surface finish free of this carbide layer. This figure also demonstrates the columnar grains which occur due to the quick diffusion of Cr through ferrite grains, and pores which are present 10 μm from the surface.

3. Experimental Procedures

3.1 Material Characterization

Two major types of materials were used in this study: commercially available monolithic ferritic stainless thin gauge sheet product and multi-layered (surface-treated) thin gauge sheet materials. The monolithic ferritic stainless sheet products include: Type 409 (Fe-11Cr, t=1.3mm), Type 439 (Fe-17Cr, t=1.6 mm) and Type 436 (Fe-17Cr-1Mo, t=1.2 mm): all of which were supplied by AK Steel through Tenneco Automotive (Cambridge, ON). The multi-layered sheet materials include aluminized Type 409 ferritic stainless steel (Al-10%Si, t=1 mm), which was supplied by AK Steel through Tenneco Automotive, and the XHOM materials (chromized interstitial free (IF) steel, t=1.3 mm), which was supplied by Arcanum Alloys (Kentwood, MI) through Tenneco Automotive.

Induced coupled plasma – optical emission spectroscopy (ICP-OES)) was used to determine the bulk composition of the three monolithic ferritic stainless steels. Three standard solutions were made for each major alloying element of interest: one containing a minimum amount expected, a second solution containing a maximum amount expected and a third solution with an amount in the middle of the range. The concentration of each standard solution is listed in Table VIII. The volume of each standard solution was chosen to be 100 mL so that the milliliter amount of each element would be equal to the percentage in the bulk of the material. Both HCl (TraceMetal Grade 37%) and HNO_3 (TraceMetal Grade 70%) were added to each standard solution since these are the acids that were used to dissolve the sample. Only 8 mL of Fe was added to each of the three standard solutions since Fe was selected as the base element in the ICP-OES program, where roughly 10% of the actual amount is needed in the standard solution.

Table VIII: Composition of Standard Solutions for ICP-OES Analysis

Solution	Blank (mL)	Standard 1 (mL)	Standard 2 (mL)	Standard 3 (mL)
HCl	5	5	5	5
HNO_3	3	3	3	3
Fe	8	8	8	8
Al	N/A	0.01	0.05	0.1
Cr	N/A	5	10	20
Cu	N/A	0.1	0.5	1
Mn	N/A	0.1	0.5	1
Mo	N/A	0.05	0.5	1
Ni	N/A	0.1	0.5	1
Si	N/A	0.1	0.5	1
Ti	N/A	0.1	0.5	1
H_2O	86.00	78.44	70.95	57.90

A small sample of each ferritic stainless steel was cut-out from the supplied sheet, mechanically-abraded down to ~0.1 g in mass and then dissolved in a mixed acid solution containing 5 mL of HCl (TraceMetal Grade 37%) and 3 mL of HNO_3 (TraceMetal Grade 70%). Double distilled water was used to fill the remainder of the 100 mL beaker. The standard solutions were then analyzed using the optical emission spectroscopy, which involves spraying the solution as an aerosol through an argon plasma to ionize the solution and the emitted wavelengths (colour) are separated and the light intensity is measured. The dissolved alloy sample solution was then analyzed using the same process. Analysis was conducted using the Varian Vista-Pro CCD Simultaneous ICP-OES model located in the MSE department at McMaster University. The measured composition is listed in Table IX.

Table IX: Monolithic stainless steel composition determined by ICP-OES (wt.%)

Element	Cr (%)	Mo (%)	Mn (%)	Si (%)	Ti (%)	Cu (%)	Ni (%)	Al (%)	C (%)	Fe (%)
Type 409	11.3	0.1	0.3	0.3	0.2	0.1	0.2	0.01	0.01	Bal
Type 439	17.5	0.1	0.3	0.3	0.4	0.1	0.2	0.01	0.02	Bal
Type 436	17.1	0.9	0.3	0.3	0.4	0.1	0.2	0.02	0.01	Bal

Analysis of the IF steel substrate of the XHOM material was analyzed using the ICP-OES technique at Arcanum Alloys, results shown in Table X.

Table X: XHOM IF steel substrate composition determined by ICP-OES

Element	Mn	Si	Ti	Al	V	P	S	C	Fe
Wt. %	0.7	0.43	0.22	0.03	0.01	0.01	0.001	0.006	Bal

The reported C content in Table IX & X was measured separately. This was done by combusting a 1 g samples in a pure oxygen atmosphere. The sample was cut from a steel sheet mechanically-abraded until a mass of 1 g was achieved. The off-gas from such a combustion consists of carbon and sulphur reacting with oxygen to form SO_2 and CO_2. The concentration of carbon is measured using infrared cells. This test was conducted using the LECO CS230 located in the MSE department of McMaster University.

3.2 Starting Material Characterization

A set of three small rectangular (approximately 1 cm x 0.5 cm, thickness dependent on material) samples were cut from each monolithic ferritic stainless steel sheet. Three samples of each were cut so that the three orthogonal planes could be separately cold-mounted in epoxy as the working surface from which to acquire metallographic images. The orthogonal planes are defined by the three orthogonal directions, which are referred to as the rolling direction (RD), transverse direction (TD) and normal (through-thickness) direction (ND). Only the two orthogonal cross-section planes (RD-ND and TD-ND) were prepared from the two multi-layered sheet materials. All working surfaces were first mechanically abraded to 4000 grit surface finish using SiC abrasive paper and water as a lubricant and then polished using a 9 μm, 6 μm, 3 μm and 1 μm clothes. Polished surfaces were etched using a modified aqua regia (15 mL HCl, 15 mL CH_3COOH, 10 mL HNO_3, 5 mL $C_3H_8O_3$) to expose grain boundaries. A cotton ball was submerged in etchant and swabbed over the working surface for 10 s, and then rinsed

with distilled water. This etching procedure was repeated until grain boundaries were fully exposed when viewed using a light optical microscope (LOM).

A light optical microscopy (Keyence VHX-6000) was used to image the microstructure of each orthogonal plane of the three monolithic ferritic stainless steels in both the as-polished and as-etched condition. As-etched images were then used to determine the average grain size and distribution of secondary phase particles. XHOM coating thickness was measured using LOM.

SEM coupled with X-ray energy dispersive spectroscopy (EDS) was used to acquire secondary and backscattered electron images and elemental composition information from the as-polished and as-etched working surfaces at higher magnification. A JEOL 6610LV SEM coupled with an Oxford Silicon Drift Detector (SDD) and associated Aztec software was used for this purpose. Images were taken at different magnifications, using 20 kV energy and a working distance of 10 mm. EDS maps used to identify the major elements that comprised the various secondary phase particles observed in the as-polished surfaces of the monolithic stainless steels and the substrates of the multi-layered materials. EDS line scans were performed to determine the concentration profile of each major alloying element through the Cr-rich diffusion coating of the XHOM material (on both the prime and non-prime surfaces) and the Al-10%Si coating on the aluminized Type 409 stainless steel material. The EDS maps were also used to quantify the thickness of the coatings on both materials.

A small rectangular (approximately 20 mm x 10 mm x 1.3 mm) sample was cut from the XHOM material for a subsequent surface analysis for elemental composition using Auger Electron Spectroscopy (AES). The non-prime surface was analyzed to determine the depth of the alumina particles, effecting the surface chromium concentration and corrosion resistance. Sample was cleaned ultrasonically for 30 min in ethanol, and preserved in a vile of isopropanol to avoid oxidation, as Auger is sensitive to surface contamination. A JEOL JAMP-9500F AUGER/FE-SEM scanning Auger microscope was used for this

purpose. Secondary electron and backscattered electron images were taken before and after a light

argon ion etch of the working surface, using an acceleration voltage of 10 kV and working distance of

23 mm. Ar^+ ions were used to remove 500 nm from the surface through sputtering to allow for an

elemental depth profile acquired using AES. Once 500 nm of material were removed, secondary phase

particles were revealed and analyzed using EDS point spectrum.

3.3 Electrochemical Polarization Tests

Working electrodes consisted of 1 cm x 1 cm samples that were cut from the starting sheet

materials using the precision cutter (Struers Secotom-50). Working surfaces (RD-TD plane) of the

monolithic stainless steels were prepared by cold mounting the square sample such that the RD-TD plan

was exposed and a copper wired aluminum taped to the non-exposed side. Working surfaces (RD-TD

plane) of the multi-layered materials were prepared in the same way ensuring samples with both the

prime and non-prime surface of the XHOM material were prepared.

Typically, the electrochemical polarization measurements were made using the sheet material in

the as-received condition. However, as discussed in Chapter 2, ferritic stainless steels may become

sensitized from exposure to high temperatures, either through the formation of Cr-depleted or C-

enriched zones adjacent to grain boundaries [16]. Considering this, a set of ferritic stainless steel and

XHOM (1 cm x 1 cm) square samples were given a sensitizing heat treatment in a vacuum tube furnace

at 650 °C for 12 h. Aluminized 409 was not included in this experiment as sensitization would only occur

in the Type 409 substrate which was already being tested. The vacuum tube consisted of a fore line,

roughing line to lower pressure and a diffusion pump to achieve the desired pressure of 10^{-5} atm. The

heat-treated disks were cleaned ultrasonically for 30 minutes in ethanol and subsequently dried using a

hair dryer before cold mounting in epoxy exposing the RD-TD plane with a copper wire attached to the

back using aluminum tape.

All electrochemical measurements were performed using a conventional three electrode electrochemical cell. A photographic image of a typical cell set up for an electrochemical polarization measurement is shown in Figure 20. As mentioned earlier, the working electrode consisted of a square sample connected to the potentiostat via a copper wire aluminum taped to the non-exposed surface. Two graphite rods served as the counter electrode (CE) and a saturated calomel electrode (SCE) was used as the reference electrode (RE). SCE was placed in a salt bridge containing potassium chloride (KCl) solution decreasing the distance between RE and WE surface. A computer-controlled Gamry Reference 600 potentiostat/galvanostat was used to carry out the electrochemical measurements.
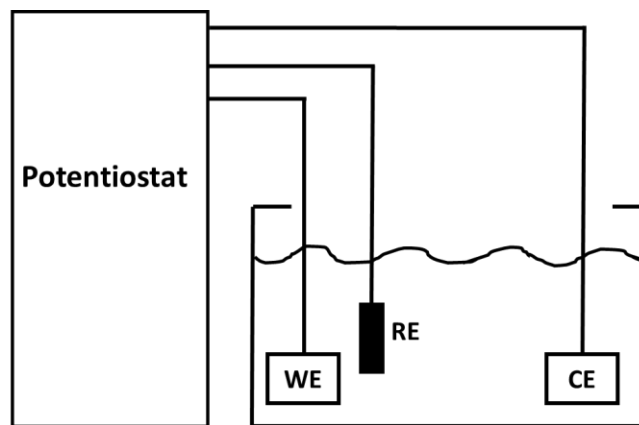
Figure 20: Three electrode cell schematic

3.4 Double Loop Electrokinetic Potentiodynamic Testing

Double loop electrochemical potentiodynamic reactivation (DLEPR) curves were acquired for the ferritic stainless steels in the as-received and sensitized (heat-treated) condition to determine relative differences in the degree of sensitization. Each alloy was tested in triplicate for reproducibility purposes. The degree of sensitization is determined by the ratio of the reactivation current density (i_r) to the activation current density (i_a), where a value above 1% is considered sensitized. A schematic comparison of a sensitized curve verse a non-sensitized curve is shown in Figure 21. The curves were acquired using a 0.5 M H_2SO_4 + 0.01 M KSCN solution at room temperature. The polarization measurement was

conducted after conditioning the working electrode at the open-circuit potential (OCP) for 1 h. Anodic

polarization was conducted at a scan rate of 1 mV/s starting at the OCP. Once the passive region was

attained, polarization was reversed back down to the original OCP at the same scan rate.
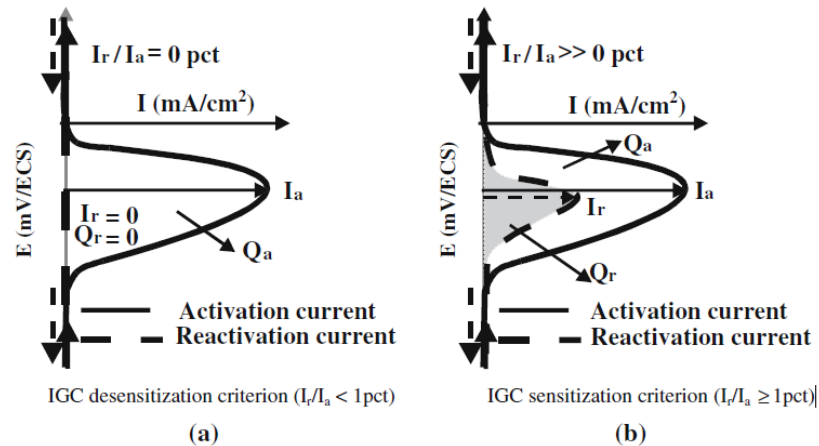
Figure 21: A schematic representation of a DLEPR curve measured for (a) non-sensitized material and (b) sensitized material *[38]*.

3.5 External Environment Potentiodynamic Procedure

Potentiodynamic polarization curves were acquired for the ferritic stainless steels in the

as-received condition to determine relative differences in the pitting susceptibility. Each alloy was tested

in triplicate sets for reproducibility purposes. With this type of measurement, the pitting susceptibility is

determined by the two characteristic potentials (breakdown potential, E_b, and corrosion potential, E_{corr})

and the relative differences between them. A schematic polarization diagram identifying these two

characteristic potentials is shown in Figure 22. The curves were acquired using a 5 wt.% NaCl (aq)

solutions held at 35 °C. This environment was chosen to match the atmospheric environments used to

evaluate the pitting susceptibility of the external surfaces of cold end exhaust components, as described

in more detail later. These measurements were made to help interpret the results from these longer

term atmospheric corrosion tests. The polarization measurement was initiated after conditioning the

working electrode at the open-circuit potential (OCP) for 1 h. Potentiodynamic polarization curves were

conducted at a scan rate of 1 mV/s starting cathodically, 300 mv below the OCP. Once an applied potential of 1 V_{SCE} was reached, the test was complete. Anodic polarization curves were acquired for both monolithic and multi-layered materials.
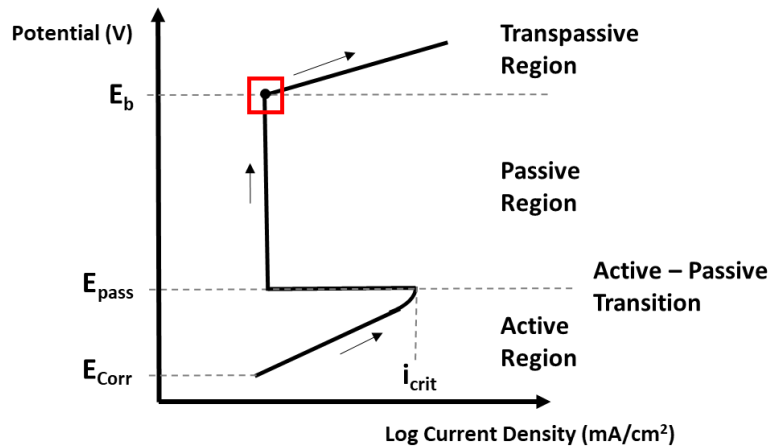
Figure 22: Schematic showing cyclic polarization curve with the characteristic potentials identified.

3.6 Continuous Near-Neutral Salt Fog Exposure Testing

The localized (pitting) corrosion susceptibility of the external surfaces on the cold end exhaust components was evaluated using the ASTM B117 Standard Practice for Operating Salt Spray (Fog) Apparatus [55]. The specific apparatus used for this purpose is an Ascott 450 CCT chamber, shown in Figure 23a. A calibration procedure was first conducted. This involved exposing five test panels (76 x 127 x 0.8 mm), made from SAE 1008 commercial-grade cold-rolled carbon steel. These test panels were cleaned by degreasing the surface using acetone. The mass of each panel was measured to the nearest 0.1 mg using a digital balance and placed in chamber at a 30° angle relative to the normal direction of the chamber, shown in Figure 23b. 250 mL beakers with a collection area of 80 cm^2 were placed near each of the samples. The panels were subjected to a continuous near neutral salt fog consisting of 5 parts NaCl and 95 parts distilled H_2O, for 48 h at 35 °C. Collection rate fell between 1 mL to 2 mL per hour, as specified in ASTM B117 Standard Practice. After the 48 h exposure period, the panels were

removed and cleaned first using distilled water, and second using a 1000 mL HCl (aq)+ 1000 mL H_2O +

10 g $C_6H_{12}N_4$ (hexamethylene tetramine) solution at room temperature. Panels were reweighed and

compared to initial mass. A mass loss of 0.817 g was achieved, which falls within specified range of

ASTM B117 calibration standard [55]. This confirmed the atmospheric chamber was calibrated for use

on research materials.

A)   B)
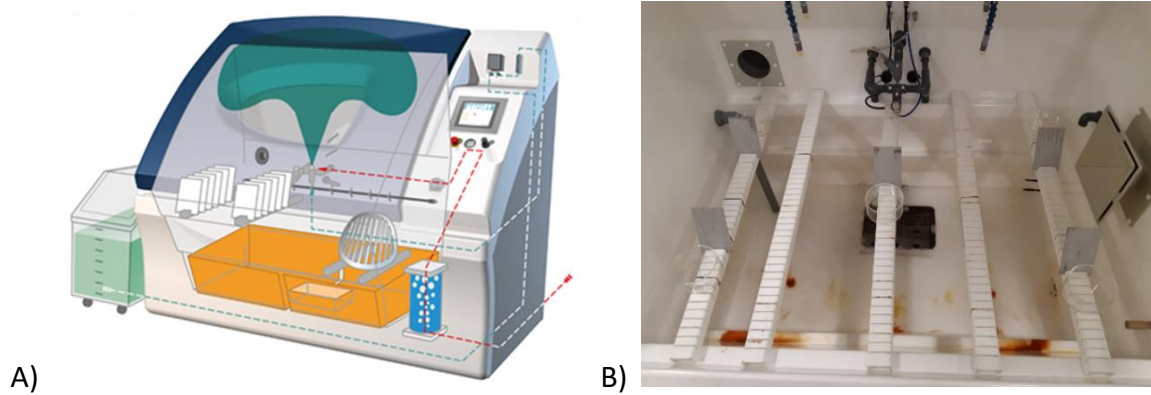
Figure 23: A) Schematic image of the Ascott 450 CCT chamber that was used to conduct the atmospheric-controlled environments used in this study *[56]* B) ASTM B117 Calibration set-up
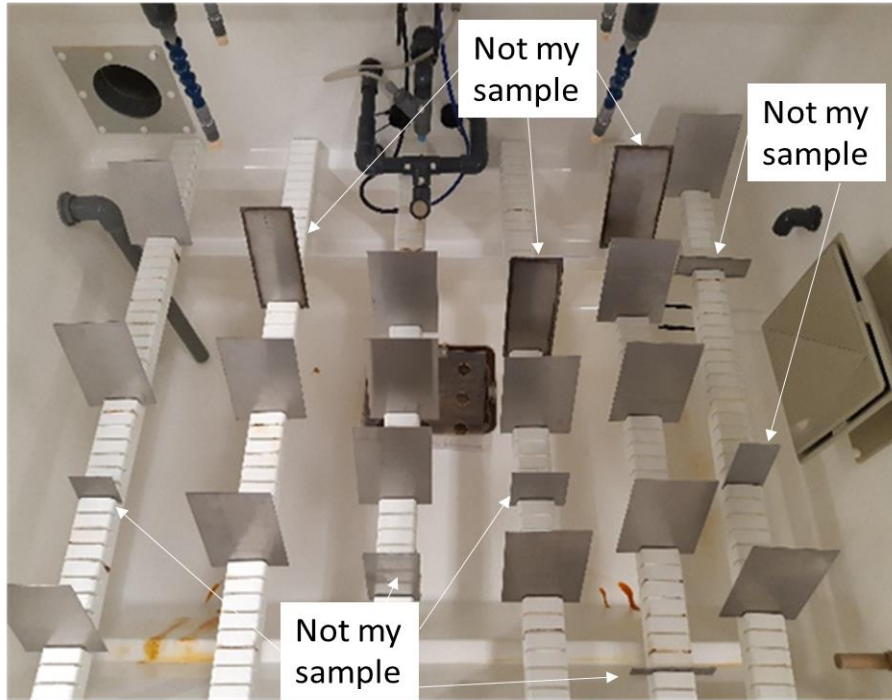
Figure 24: Image showing the placement of the coupons for the ASTM B117 exposure.

A set of triplicate coupons (15 cm × 10 cm) were prepared from each material. Smaller samples

shown in Figure 24, belong to other researchers conducting the same test. One triplicate set of XHOM

coupons were tested with the cut-edges exposed and a second triplicate set was tested with the cut

edges masked off with a silicone adhesive. An additional triplicate set of Type 409 and XHOM coupons

were included to determine the corrosion resistance of a cut edge, as associated with drain holes in cold

end components. A set of two simulated drain holes (3.2 mm in diameter) were introduced into the

triplicate set of coupons of each material: one drilled and one punched. Figure 25 shows a schematic

diagram and a photographic image of one such coupon prepared with two adjacent simulated drain

holes (one drilled and the other punched). The cut-edges of the triplicate sets of XHOM coupons were

masked off using silicone adhesive, leaving the cut edge of the drain holes exposed. All coupons were

cleaned ultrasonically in ethanol for 30 minutes, weighed using a digital balance with a precision of 0.1

mg and photographed before being placed into the atmospheric chamber sample holder, which placed

the coupons at an angle of 30° relative to the normal direction of the chamber. The prime side of the XHOM material was boldly exposed, and the non-prime side was shielded. The 1000 h exposure was interrupted on a weekly basis (after 143 h) to permit a mass measurement and a photograph to document the progression of corrosion with time.
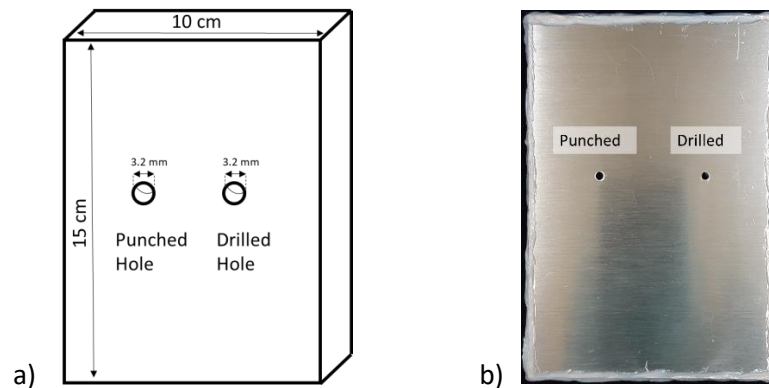
Figure 25: a) Schematic diagram b) photographic image of a coupon prepared with two adjacent simulated drain holes
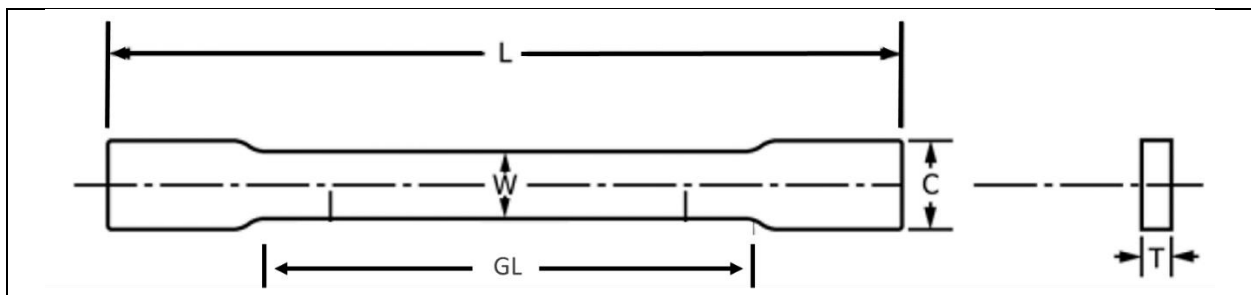
After completion of 1000 h, all coupons were imaged and weighed to permit a mass gain calculation. Surface deposits (salt and corrosion products) were then mechanically removed by sandblasting. Care was taken to include an unexposed coupon of each material as a control for mass loss during this sandblasting step. Coupons were then imaged again and re-weighed to permit a mass loss calculation. Images of coupons after sandblasting were analyzed using ImageJ software to determine a pitting corrosion density. Once a minimum pit diameter was chosen, ImageJ software was able to count each individual pit and divide this value by total surface area. One coupon from each triplicate set of coupons exposed was then cut in cross section, cold-mounted in epoxy, polished to a 1 μm surface finish using standard metallographic procedures and imaged using light optical microscopy.

3.7 Effect of Strain Testing

Due to a lower corrosion resistance found on the edge of Type 409, strain during shearing was considered as a main contributor. To investigate the influence and progression of strain, Type 409 and

XHOM samples were pulled to 5% and 10% strain at a cross head speed of 2mm/min, using the MTS 100 KN testing frame. The gauge length was then cut into 1 cm x 1 cm squares, and cold mounted in epoxy with a copper wire aluminum taped to the back of the metal surface exposing the RD-TD plane. Samples were then anodically polarized above the E_b value at a rate of 1 mV/s in a 5% NaCl (aq) solution held at 35 °C. Dimensions of tensile coupon can be seen in Table XI.

Table XI: Tensile coupon dimensions

| L = 200 mm |
| W = 12 mm |
| C = 18 mm |
| t(409) = 1 mm, t(XHOM) = 1.3 mm |
| GL = 160 mm |

As the effect of strain on the corrosion resistance of the XHOM coating was the target of this experiment, only Type 409 was tested of the benchmark materials.

3.8 Cyclic Acid Condensate Exposure Testing
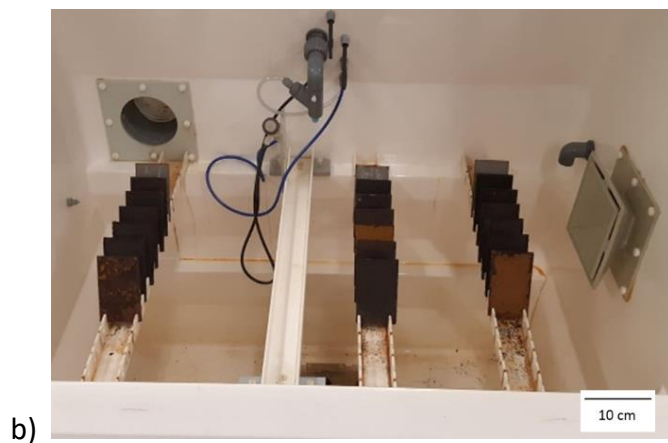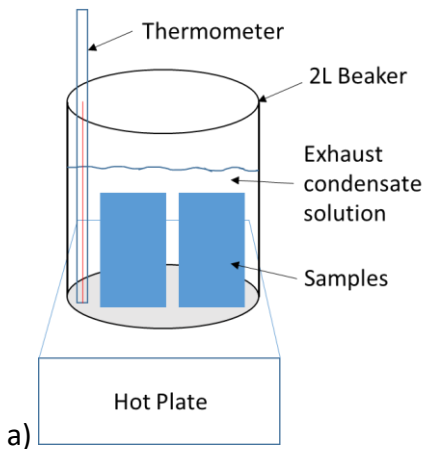
Figure 26: Photographic image of a) Exhaust gas condensate bulk immersion schematic b) Coupons arranged on racks placed within the atmospheric chamber.

43

A triplicate set of coupons (10 cm × 8 cm) were prepared from each material, with the long direction parallel to the rolling direction. All coupons were ultrasonically cleaned in ethanol for 30 minutes, weighed using a digital balance with a precision of 0.1 mg and photographed before testing. The cyclic experiment was run for nine cycles: each cycle has been designed to simulated one full year in service [57]. The cyclic exposure procedure is an in-house procedure developed by Tenneco Automotive containing the following 6 steps:

1) Heat treat coupons for one hour at 650 °C in air and then air cool to room temperature

2) Submerge coupons in synthetic condensate solution** at 43 °C and soak for 15 minutes

   a. Solution heated using hot plate shown in Figure 26a.

3) Remove coupons and rinse with 5 wt.% NaCl (aq), then place coupons in a drying oven held at 65 °C for 1 h

4) Place coupons in an atmospheric chamber held at 60 °C and 85% RH for 24 h.

5) Repeat steps 2-4 each day for 5 days

6) Leave coupons in atmospheric chamber for two additional days after day 5

   ** Synthetic Condensate Solution: 5000 ppm SO_4^{2-} as $(NH_4)_2SO_4$ (aq); 100 ppm Cl^- as NH_4Cl (aq); acidify to pH between 2.0 - 2.2 with H_2SO_4 (aq); solution made using Type 4 RO Water, reused and replenished as needed.

Once nine cycles were complete, samples were imaged and weighed to permit a mass gain calculation. Surface deposits were then mechanically removed by sandblasting. Care was taken to include an unexposed coupon of each material as a control for mass loss during this step. Coupons were then imaged again and re-weighed to permit a mass loss calculation. Due to the high amount of pits and corroded surfaces, ImageJ is not accurate enough to provide an accurate pitting density. Maximum pit depth and mass loss was used as material property comparisons. As well due to the large amount of pits on the surface, laser profilometry would have difficulty differentiating between pits when attempting to

obtain a pit depth analysis. For this reason coupons were cut into four sections and observed under the

LOM. When the deepest pit was found, a cross-section was removed, cold mounted in epoxy, polished

to a 1 μm surface finish using standard metallographic procedures and imaged using light optical

microscopy.

4. Results and Discussion

4.1 Starting Microstructure

Images of typical microstructures were taken of each monolithic material in all three orthogonal

planes (RD-TD, RD-ND, TD-ND). Due to comparable microstructures of each plane only the ND-TD plane

is shown in Figures 27-29. Through LOM imaging, a single phase (ferrite) microstructure with an average

grain size of about 40 μm and randomly distributed TiC, TiN and TiCN particles were observed. These

intermetallic types were confirmed though EDS mapping, as shown in Figures 27-29. A higher density of

TiCN particles was observed and easily located due to their elongated shape. TiN particles tend to

precipitate in molten steel forming a cube shaped particle and eventually TiC particles form around the

TiN particles breaking up the cube into an elongated intermetallic particle [42]. A large quantity of Ti-

rich precipitates form due to the high concentration of Ti added for the purpose of grain refinement, as

well as tying up free C and N. Commonly 6 x (%C) of Ti is added [40], yet these materials contain up to 40

x (%C) demonstrated in the composition analysis in Section 3.1. Ti-rich precipitates can range up to 20

μm in size. This set of observations is consistent across all monolithic materials.
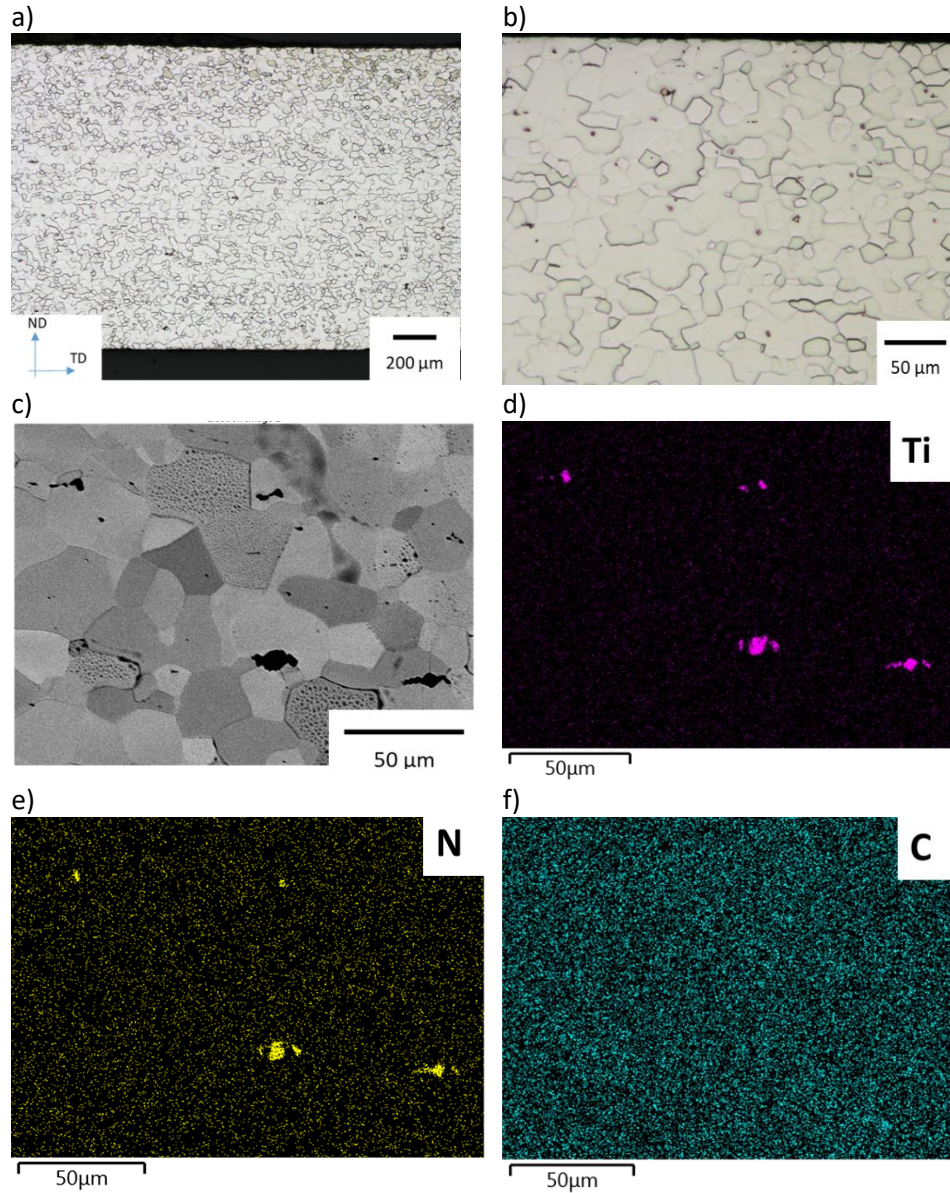
Figure 27: Starting microstructure of Type 409 a) Low Mag LOM Image b) High Mag LOM Image c) SEM-BSE Image d) Ti EDS Map e) N EDS Map f) C EDS Map
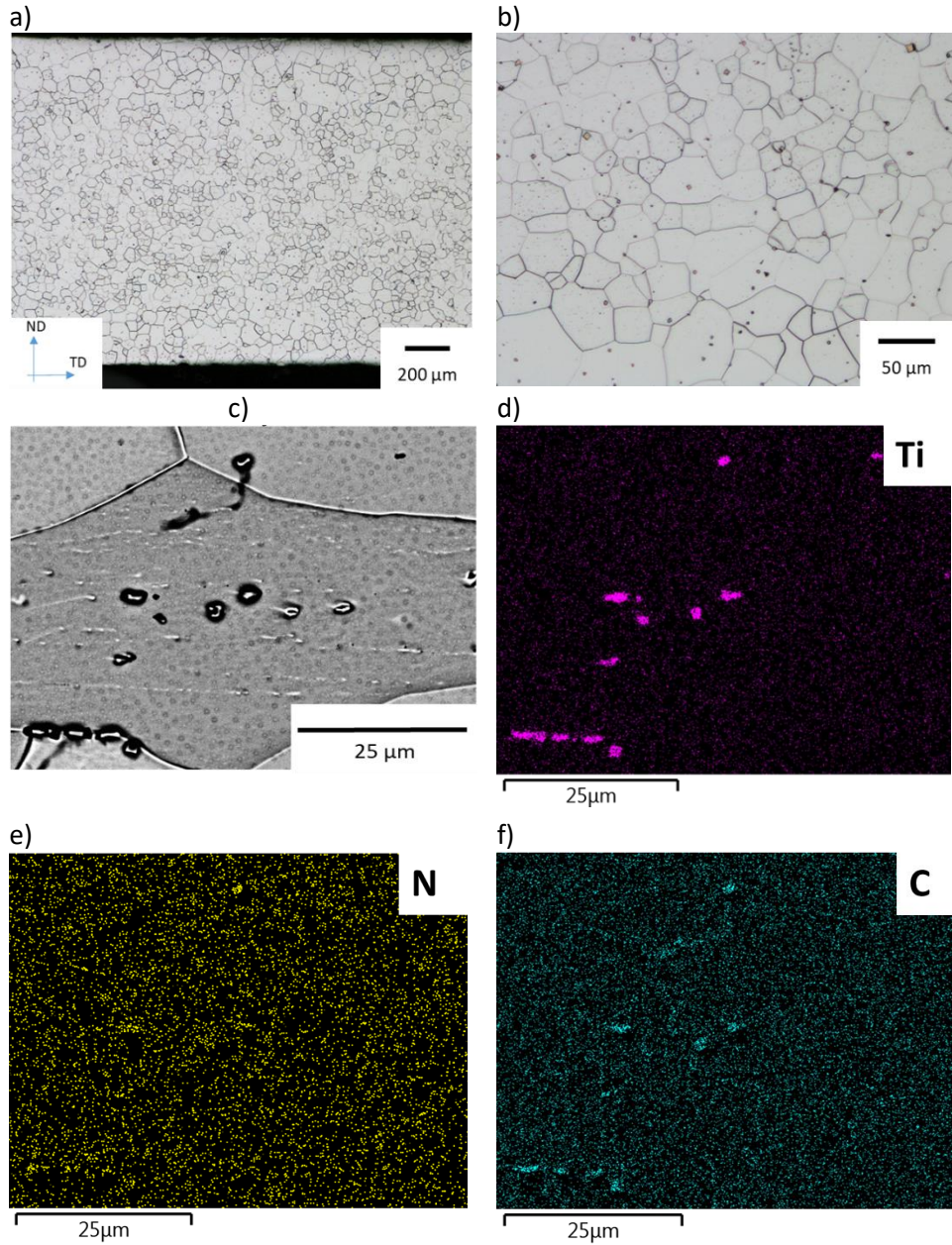
Figure 28: Starting microstructure of Type 436 a) Low Mag LOM Image b) High Mag LOM Image C) SEM-BSE Image d) Ti EDS Map e) N EDS Map f) C EDS Map
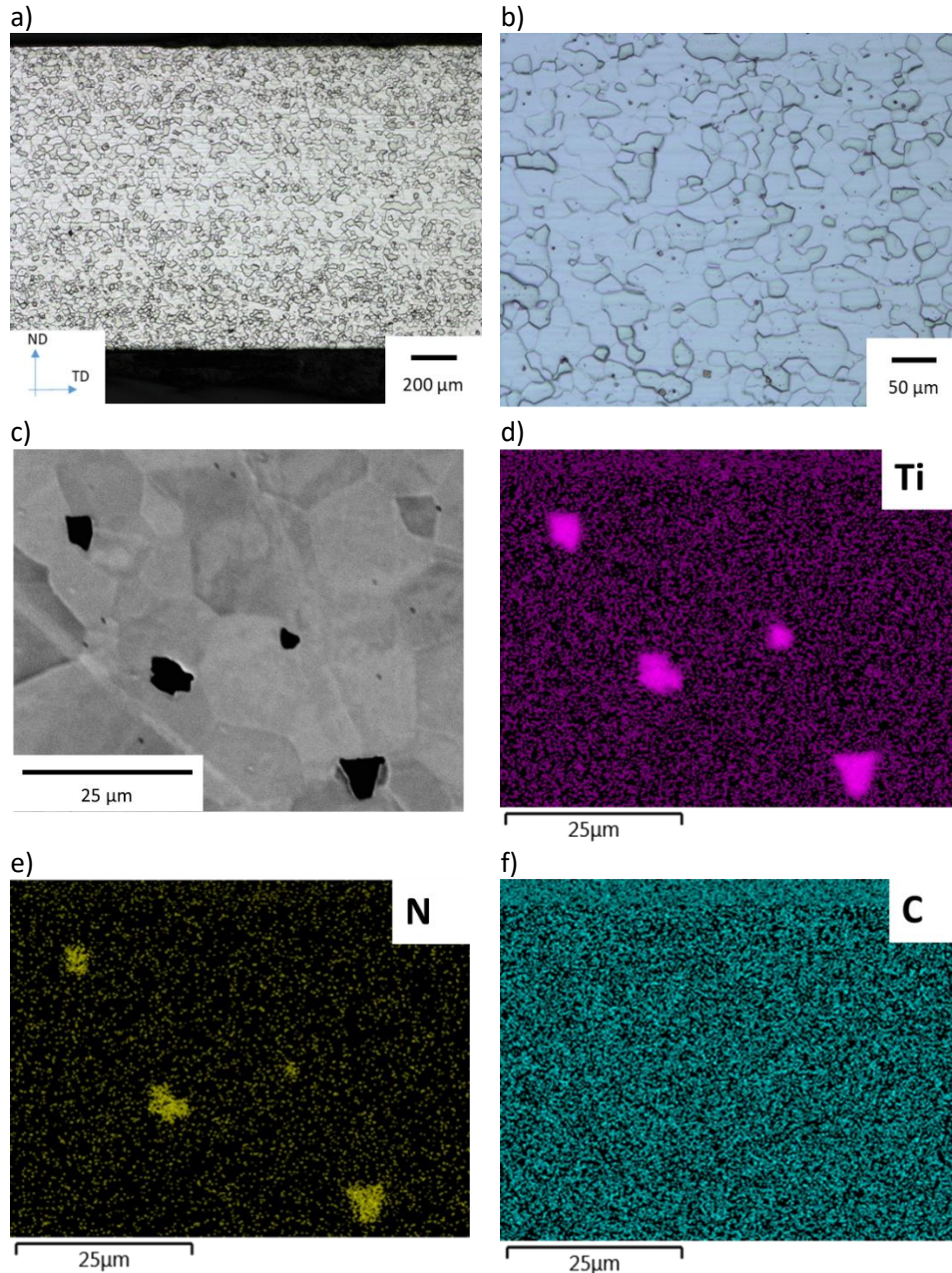
Figure 29: Starting microstructure of Type 439 a) Low Mag LOM Image b) High Mag LOM Image c) SEM-BSE Image d) Ti EDS Map e) N EDS Map f) C EDS Map

Due to the Al-10%Si coating being very thin, it is invisible in the low mag LOM image in

Figure 30a, but visible in the high mag LOM image in Figure 30b. The sub-layer visible below the

Al-10%Si coating is likely the interdiffusional layer (IDL) that is caused by the rapid diffusion of Fe and Cr

in to the coating during the hot dip process. Si is added to the molten Al bath to impede the runaway

growth of this intermetallic diffusional phase, which does not provide galvanic protection to the Type

409 substrate. The IDL is very distinct in Figure 30c. Using SEM-EDS mapping, the IDL was found to be comprised of Fe and Cr from the Type 409 substrate, as well as Al and Si from the coating (Figure 30d, 30e and 30f). Moreover, the Si map in Figure 30c indicates Si segregates within the coating (towards the top surface), Si-rich phases and the IDL.
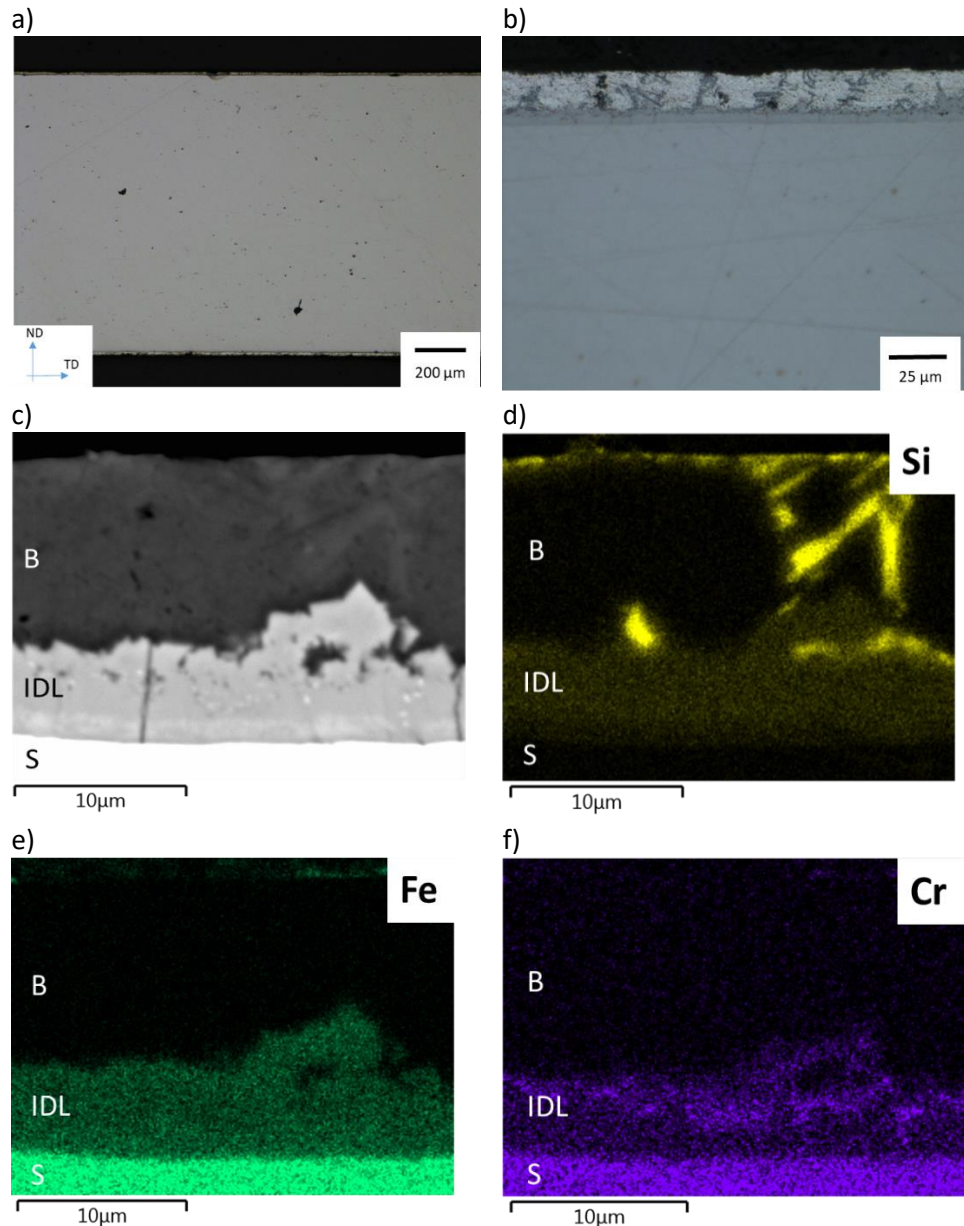
Figure 30: Starting microstructure of Type 409Al a) Low Mag LOM Image b) High Mag LOM Image c) SEM-BSE Image d) Ti EDS Map e) N EDS Map f) C EDS Ma. B = Bulk, IDL = Interdiffusional layer, S = Substrate

The linescan in Figure 31 illustrates the diffusion of Fe and Cr into the coating that occurred during the hot dipping process. Cr has segregated to the bulk coating/IDL interface, shown by the spike in the diffusion profile in Figure 31, and the elemental map in Figure 30f. There is a drop from 11% Cr in the bulk to 5% Cr in the IDL that is followed by an increase to 8% Cr in the Cr-rich layer at the bulk coating/IDL interface. Silicon is shown again to segregate to the IDL, drop in the bulk coating and increase to 20% near the coating surface. Fe drops from 88% in the bulk to 25% within the IDL, whereas Al drops from 90% in the bulk coating to 60% within the IDL, and then to 0% at the IDL/substrate interface.
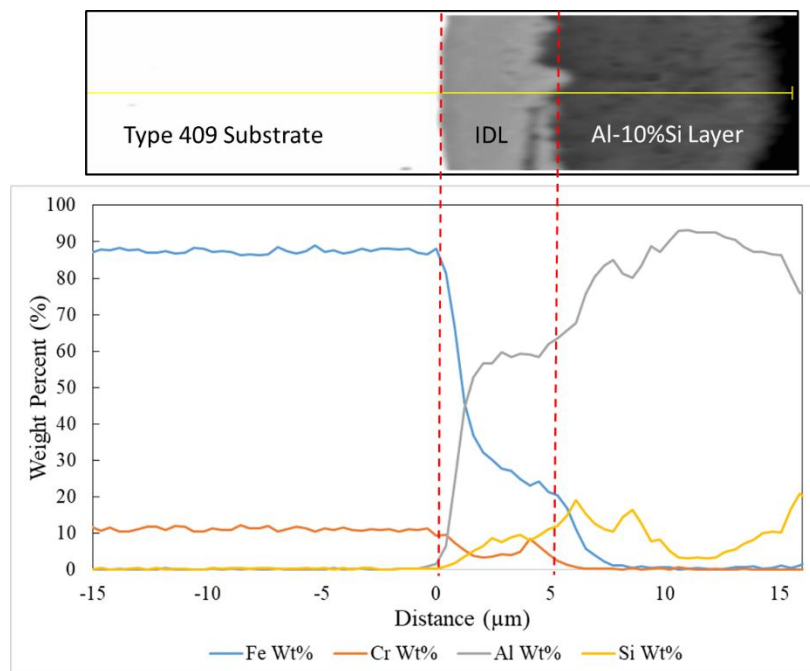
Figure 31: EDS line scan through aluminized coating

The XHOM chromized layer can be seen in Figure 32. The coating is broken down into two sections: skin layer and bulk layer. The skin layer is comprised of the top 10 μm of the chromized layer and contains equiaxed grains, whereas the bulk layer (about 70 μm thick) contains columnar grains. Pores 2-4 μm in size are visible at the skin/bulk interface, as shown in Figure 32c and 32d. The pores could be due to Al_2O_3 particles that were removed during polishing. However, from Figure 32g and 32k, Al_2O_3 particles

are more prominent within pores on the non-prime side compared to prime side. These particles are

likely the Al_2O_3 particles added to the Cr-slurry to avoid "stickers" from occurring during the chromizing

process. Figure 33 and 34 show elemental maps of the XHOM prime and non-prime side, illustrating the

difference in Al_2O_3 distribution on the chromized surface.
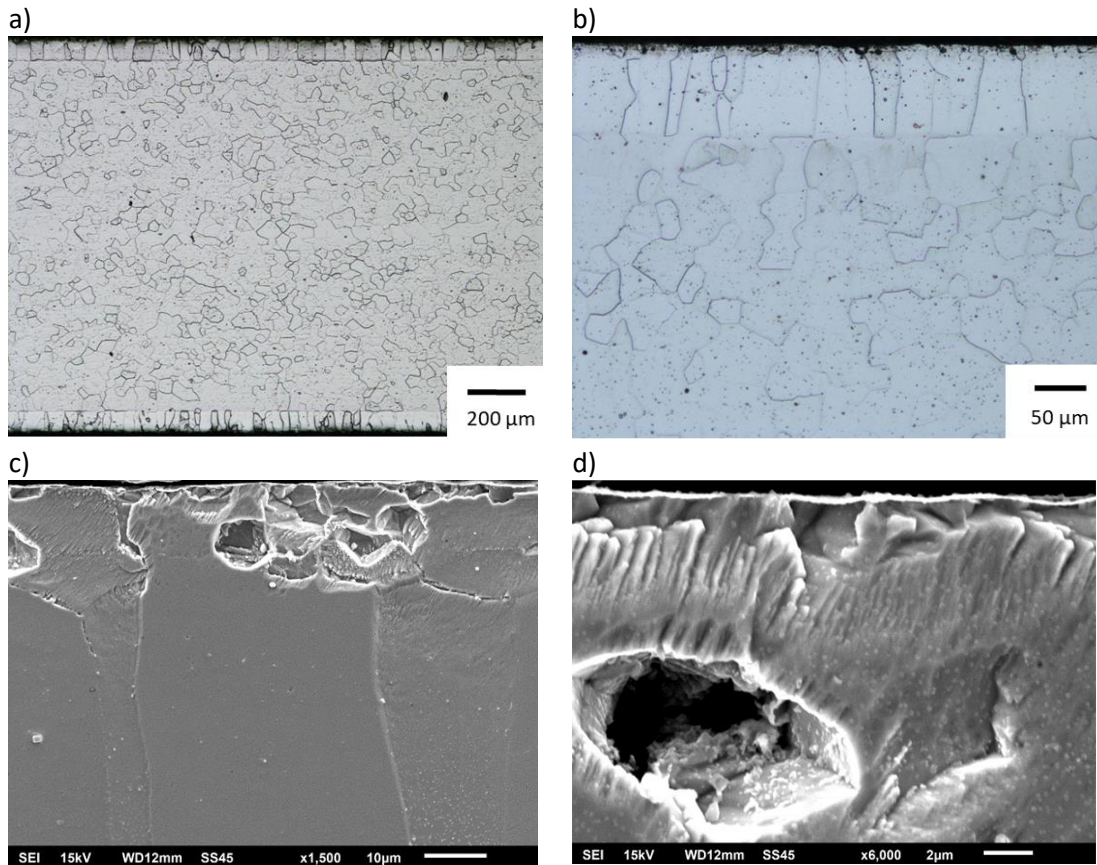
Figure 32: Images of XHOM starting microstructure a) Low mag LOM image b) High mag LOM image c) SEM-SEI image d) High mag SEM-SEI image
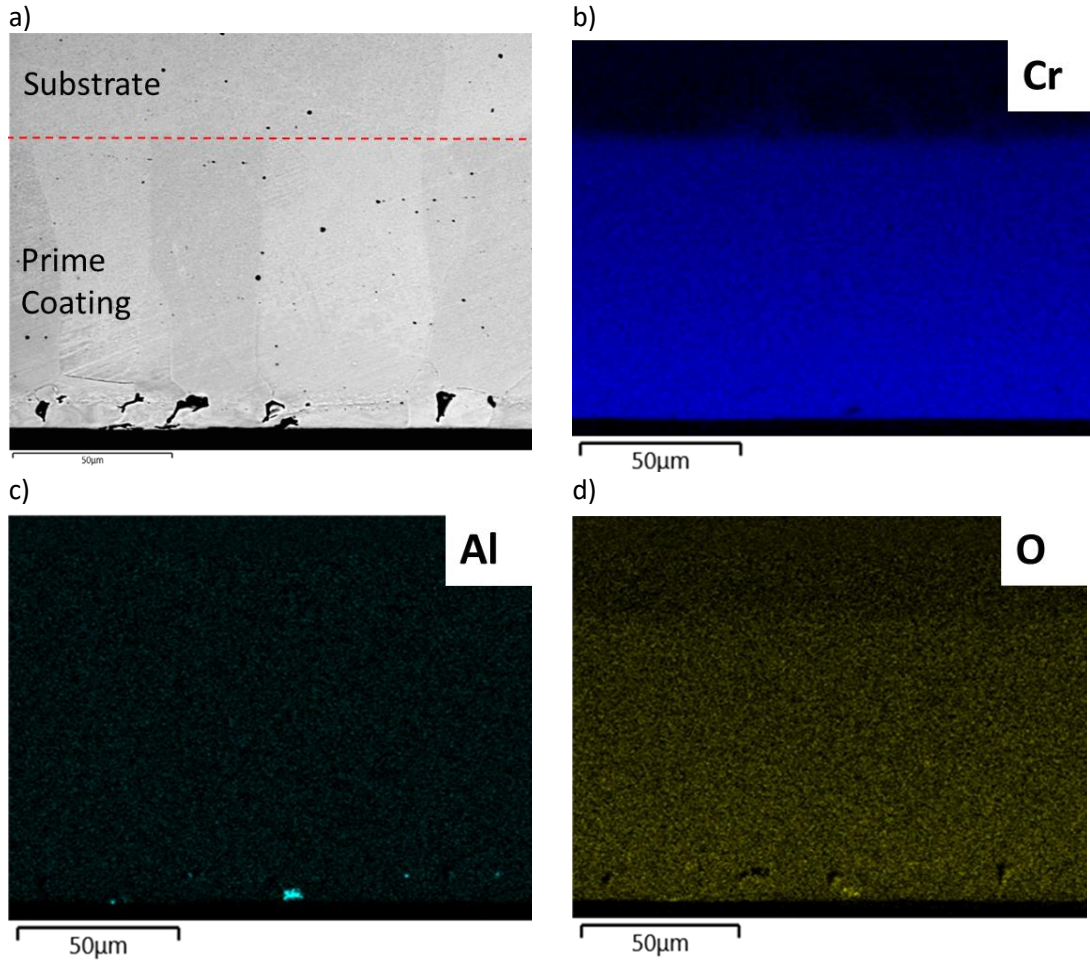
Figure 33: XHOM Prime SEM-EDS maps a) SEM-BSE image b) Cr elemental map c) Al elemental map d) O elemental map
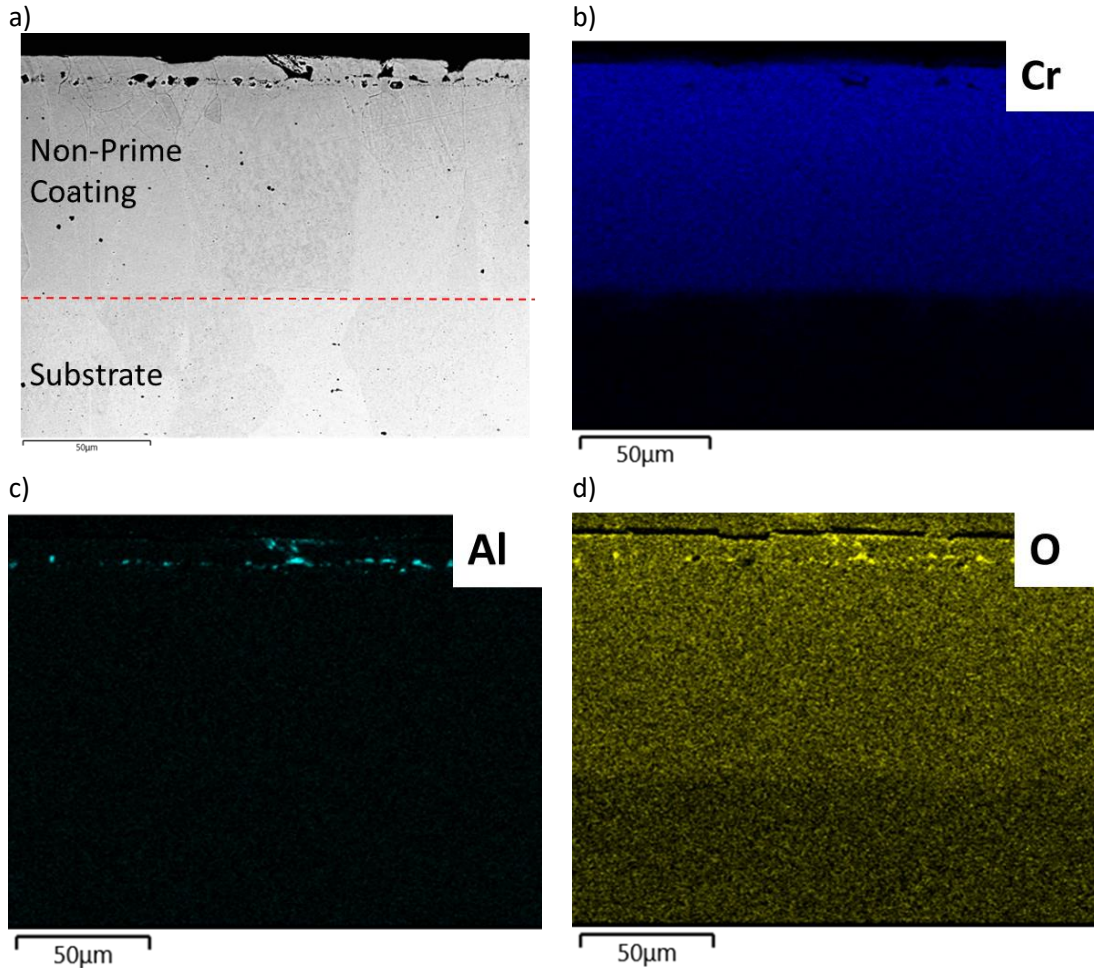
Figure 34: XHOM Non-prime SEM-EDS maps a) SEM-BSE image b) Cr elemental map c) Al elemental map d) O elemental map

To obtain Cr diffusion profiles through the coating, EDS linescans were acquired through the XHOM prime side and non-prime side, shown in Figure 35 and 36. Although the cross section of the prime and non-prime side seems identical, Figure 35 and 36 confirms there are elemental differences between the coatings. The Cr diffusion profile in Figure 35 is linear due to the rapid diffusion of Cr into α-ferrite. Yet in Figure 36 there is a decrease and subsequent increase in the Cr diffusion profile. This initial decrease is a result of the line scan crossing an Al_2O_3 particles on the surface, increasing the percentage of Al whilst decreasing the Fe and Cr concentrations. At a depth of 1 μm, the Cr and Fe profile matches that of the prime side. The surface roughness of the non-prime side is greater than that

of the prime side, which is to be expected due to the higher density of pores found on the non-prime

surface, as shown in Figure 37.
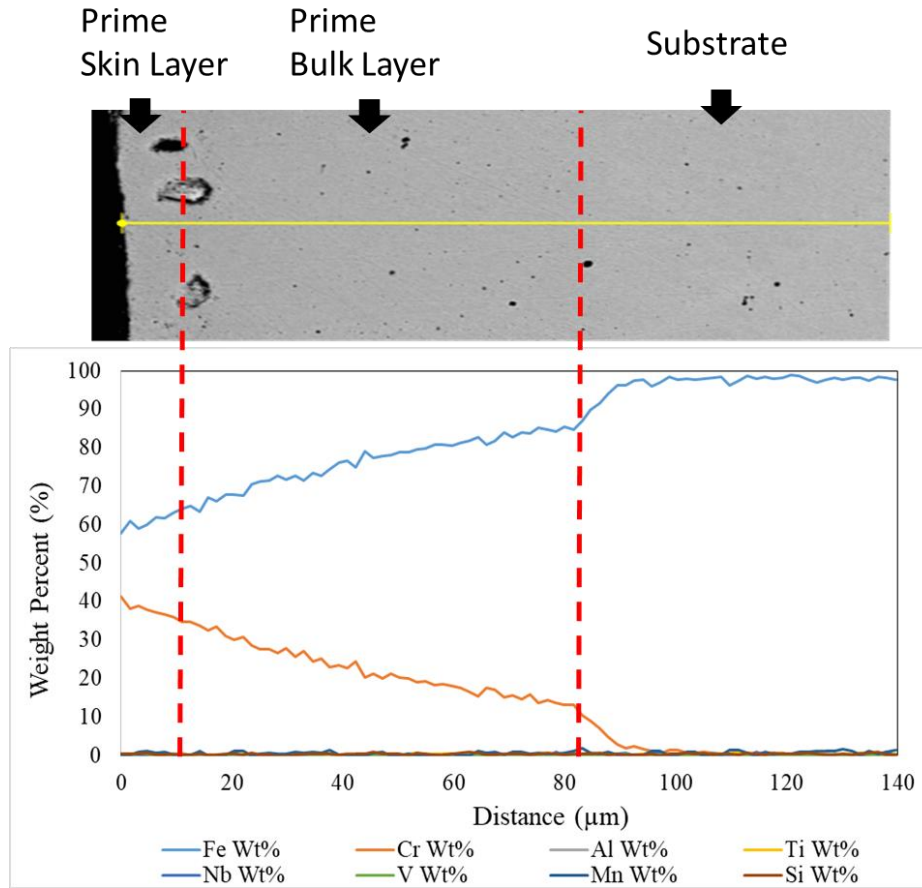
Figure 35: EDS Line scan through XHOM prime layer
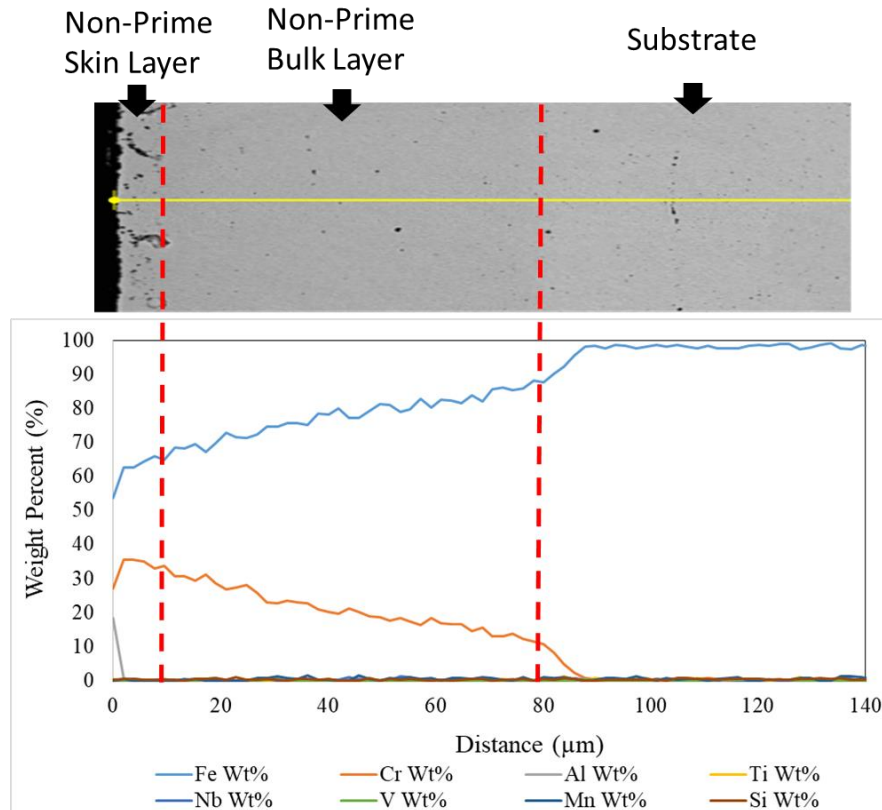
Figure 36: EDS Line scan though XHOM Non-Prime layer

SEM-EDS maps were acquired on the plan surface of both the XHOM prime and non-prime side. After imaging, the surface of the sample was then Ar etched *in-situ* within the AES chamber, removing approximately 500 nm of material. Due to the slower etching rate of Al_2O_3 compared to the chromized layer, the Al_2O_3 particles remained on the surface, whereas the chromized layer was preferentially sputtered away. At first glance, the black spots across the entire surface were assumed to be Al_2O_3 particles, based on the acquired elemental maps shown in Figure 37. Post etching, the Al_2O_3 particles are shown protruding from the surface as white spots, Figure 37h. This observation reveals that the black spots seen distributed across the surface were pores on the surface with Al_2O_3 particles embedded within, and appeared dark due to the shadowing effect of the pore. These pores are believed to be formed during the temper rolling step after the chromizing process. The pores created also behave as crack initiation sites, as shown in Figure 37a.
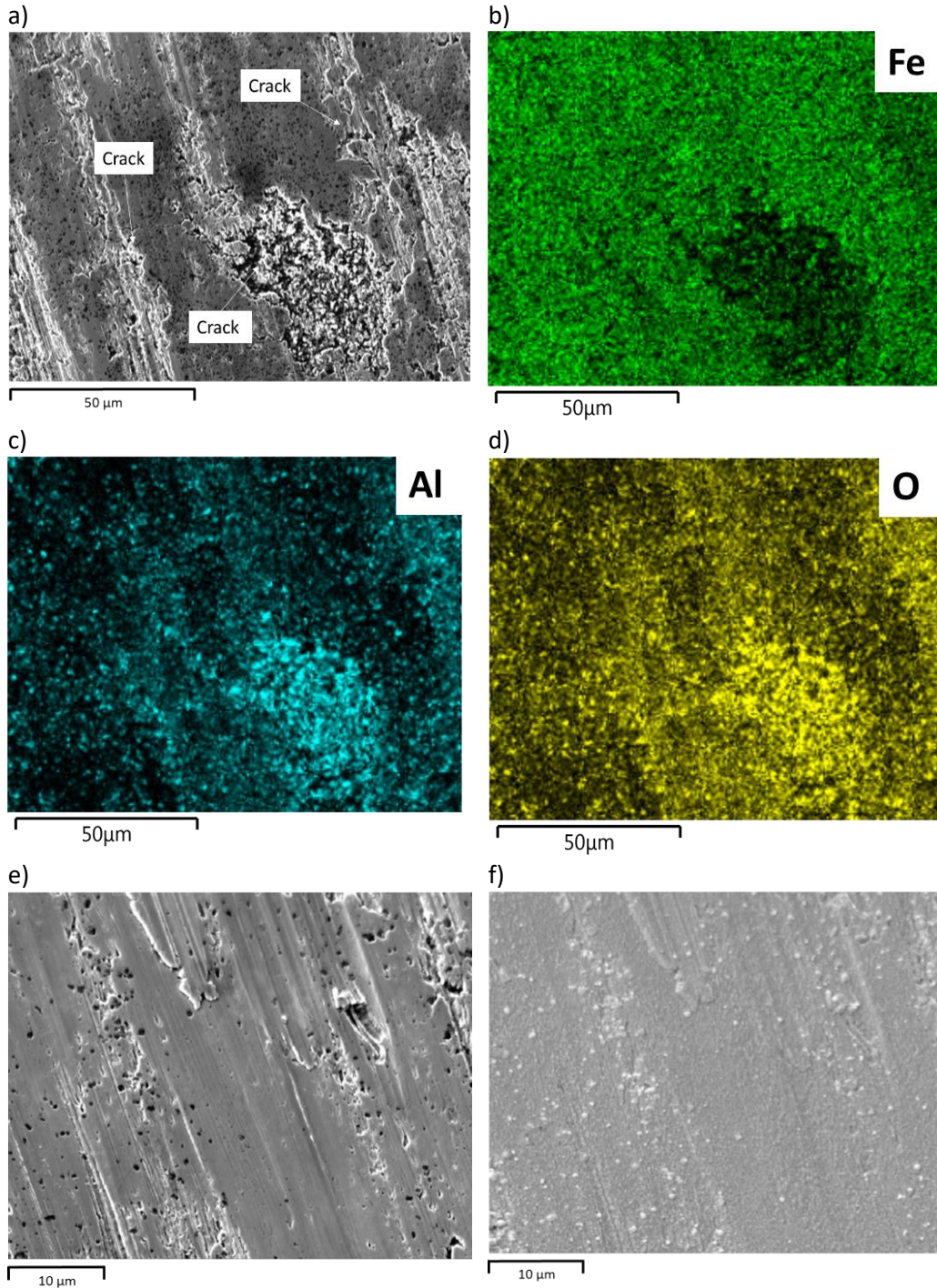
Figure 37: SEM-BSE plan view of XHOM non-prime side A) SEM-BSE Image B) Fe EDS map C) Al EDS map D) O EDS map e) SEM-SEI image f) SEM-SEI image g) Pre Ar etch h) Post Ar etch

The distribution density of Al_2O_3 particles on the chromized surface is different when comparing the prime and non-prime side. More Al_2O_3 particles are present on the non-prime side, Figure 37, than the prime side, Figure 38, due to the placement of the Cr-rich slurry, leading to more crack initiation sites.

This increases the dislocation density of the non-prime chromized surface decreasing the corrosion resistance, according to Lv et al. [27].
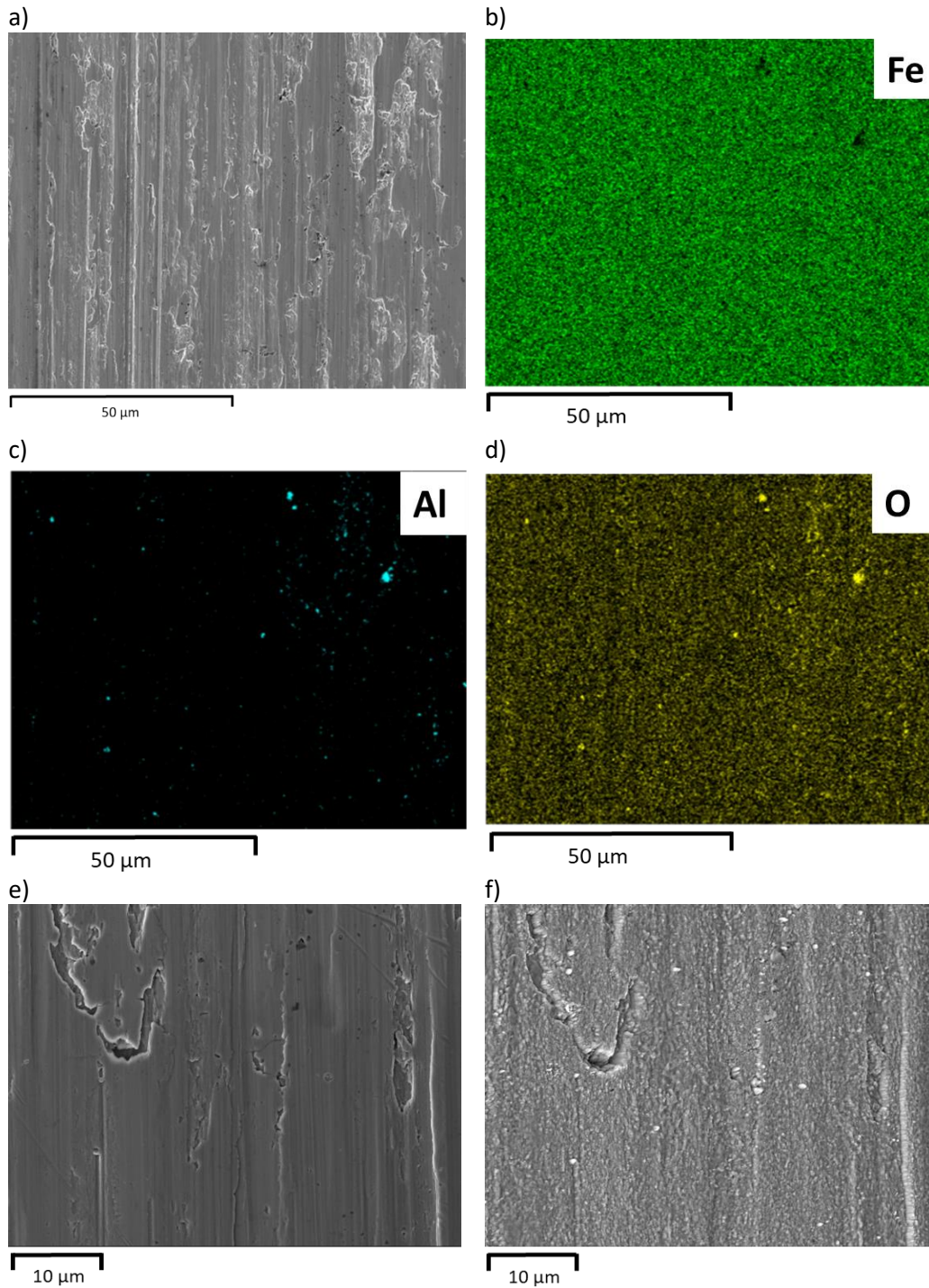
Figure 38: Figure 8: SEM-BSE plan view images of XHOM prime side A) SEM-BSE Image B) Fe EDS map C) Al EDS map D) O EDS map e) g) Pre Ar etch h) Post Ar etch

4.2 Double Loop Electrokinetic Potentiodynamic Reactivation (DLEPR)

As exhaust components in the cold end reach temperatures ranging from 100 °C – 650 °C, as illustrated in Figure 1, sensitization is likely to occur. To combat this corrosion mode, a high concentration of Ti is added to exhaust components up to 40 x (%C). The results shown in Figure 39, prove this method is successful in impeding sensitization. Type 409 shows evidence of sensitization prior to the 12 h heat treatment, implying sensitization occurred during the smelting and/or hot rolling process at the steel mill. Interestingly, no further sensitization occurred within the material during the 12 h 650 °C heat treatment. Type 439 also shows evidence of sensitization prior to 12h heat treatment, yet it is significantly less sensitized than Type 409. This result can be explained by Figure 6 in section 2.3, which illustrates a linescan across a grain boundary containing a Cr-rich $M_{23}C_6$ particle. The Cr concentration in Figure 6 decreases below the critical Cr concentration required for passivity. Therefore a Cr-lean alloy such as Type 409 that has a bulk composition of Fe-11Cr is more likely to contain regions in which the Cr content drops below the critical Cr content required for passivity compared to Type 439 that has a bulk composition of Fe-17Cr. Subsequently Type 439 also shows no evidence of further sensitization after the 12 h 650 °C heat treatment as well. Type 436 shows no evidence of sensitization in the as-received state, signifying this alloy is resistant to sensitization during the smelting and/or hot rolling step, unlike Types 409 and 439. As well, the i_r/i_a ratio is unchanged after the 12 h 650 °C heat treatment, signifying this material is unaffected by this heat treatment. XHOM shows no evidence of sensitization in as-received state, as well as after the 12 h 650 °C heat treatment, similar to that of Type 436 exemplifying its sensitization resistance. The i_a, i_r and i_r/i_a ratio for each material in the as-received state and heat treated state can be seen in Table XII.
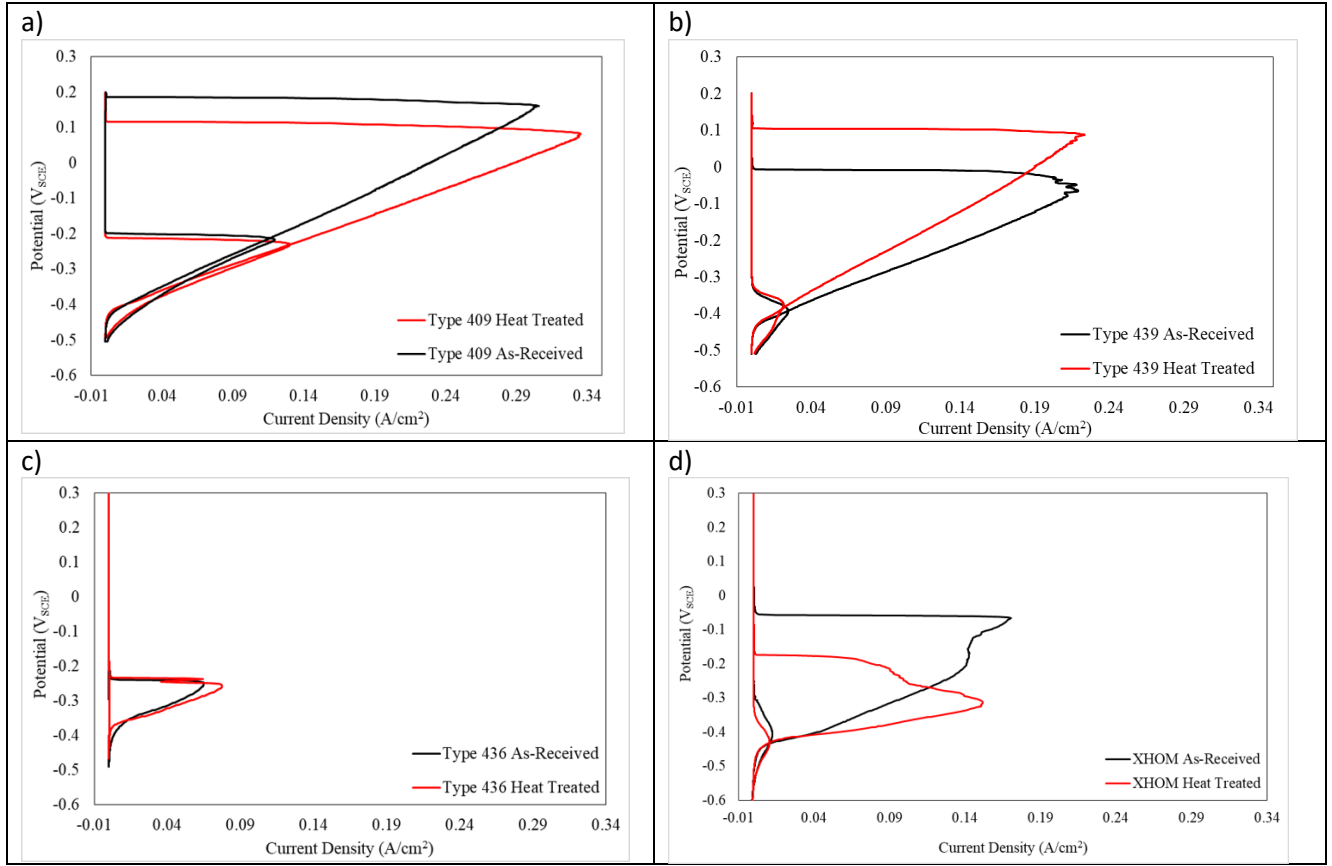
Figure 39: DLEPR Curves before and after 12 h 650 °C heat treatment a) Type 409 b) Type 439 c) Type 436 d) XHOM

Table XII: DLEPR sensitization data

Samples	i_a (A/cm^2)	i_r (A/cm^2)	i_r/i_a (%)
Type 409 As-Rec	0.306	0.118	39
Type 409 Heat Treated	0.315	0.129	41
Type 439 As-Rec	0.229	0.0236	11
Type 439 Heat Treated	0.223	0.0213	10
Type 436 As-Rec	0.067	0.0002	0.3
Type 436 Heat Treated	0.077	0.0002	0.3
XHOM As-Rec	0.12	0.0027	2
XHOM Heat Treated	0.152	0.00105	1

4.3 External Environment Corrosion

4.3.1 ASTM B117 Polarization Results

The results of the monolithic curves in Figure 40a show the difference in E_b between the monolithic stainless steels. The trend of increasing E_b mirrors the trend in increasing PREN values that are listed in the legend. The increase in E_b from Type 409 to Type 439 is a result of the increase in Cr

concentration, and the Mo addition is responsible for the increase in E_b from Type 439 to Type 436. To compare the performance of the monolithic alloys and multi-layered materials, Type 436, which exhibits the highest E_b among the monolithic alloys, served as the comparative baseline for the multi-layered materials. The XHOM prime and non-prime surface both contain a higher Cr containing surface than Type 436 and this is evident in their higher PREN and subsequent E_b value. The difference in the E_b value of the XHOM prime and non-prime is also consistent with the difference in Cr content at each surface. The E_b is also influenced by the embedment of Al_2O_3 particles causing defects on the surface of the non-prime side as seen in Figure 37 and 38. The Type 409Al curve shows no evidence of passivity, signifying that the aluminum coating will not form a passive film, corroding rapidly due to the galvanic couple as well as poor corrosion resistance of the coating.
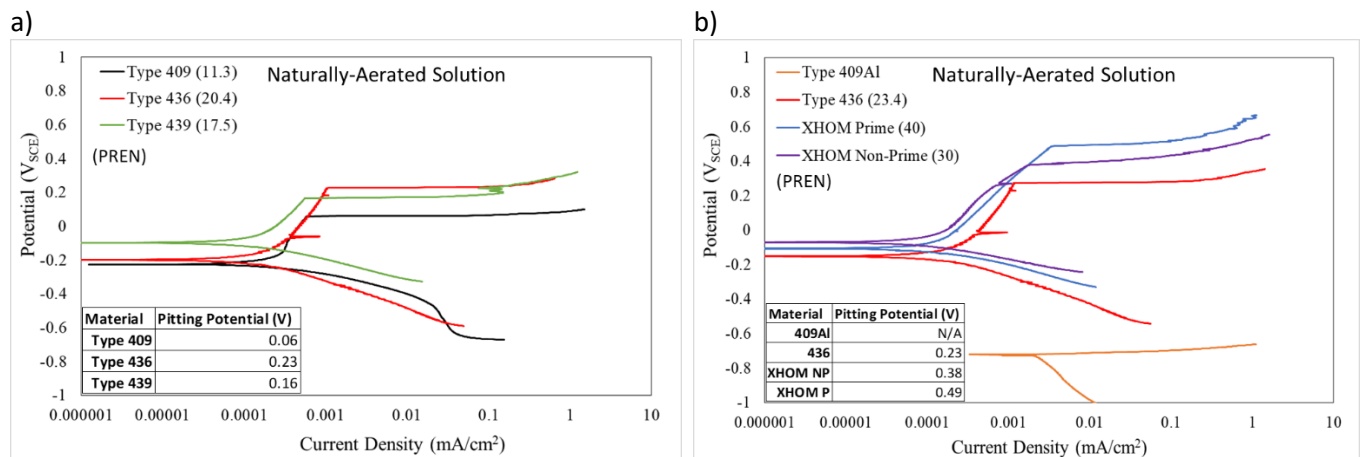
Figure 40: Potentiodynamic curve in 5% NaCl solution heated to 35 °C a) monolithic material b) multi-layered material

4.3.2 ASTM B117 Exposure Results

Images of each material, before exposure, after exposure and after cleaning can be seen in Figure 42. The Cr-lean alloy, Type 409 began corroding at the top cut edge of the panel, with corrosion product migrating down the surface, as shown in Figure 42a. With the corrosion product sandblasted off, localized corrosion sites are only evident in regions that were covered by the migrated corrosion product. This phenomena was reported by Suleiman *et al.*, as discussed in Section 2.2. The metal surface

below the corrosion product behaves anodically, whereas the outer surface of the corrosion product

behaves cathodically, reducing H_2O [33]. Therefore, the Type 409 surface is resistant to the ASTM B117

corrosive environment for the time considered, barring a rust deposit forming. The cause for corrosion

of the cut edge is explained by two possible methods. The first being a result of the mechanical

deformation applied during the shearing of the sheet metal leading to an increase in the local

dislocation density. This increase in local dislocation density may give rise to an increase in the reactivity

of Fe atoms on the metal surface [26]. The second being due to micro-galvanic corrosion involving TiN

precipitates boldly exposed on the cut edge surface. According to Ludlow [58], TiN grow in size the

further from the surface, implying that there should be larger TiN particles present on a cut edge (cross-

section) surface compared to the RD-TD surface. These theories imply a lower corrosion resistance at

the cut edge, which is evident by the Type 409 ASTM B117 results. This is further proven by the

potentiodynamic curve in Figure 41, illustrating the difference in the E_b value of the Type 409 plan

surface and the cut edge (ND-TD) surface.
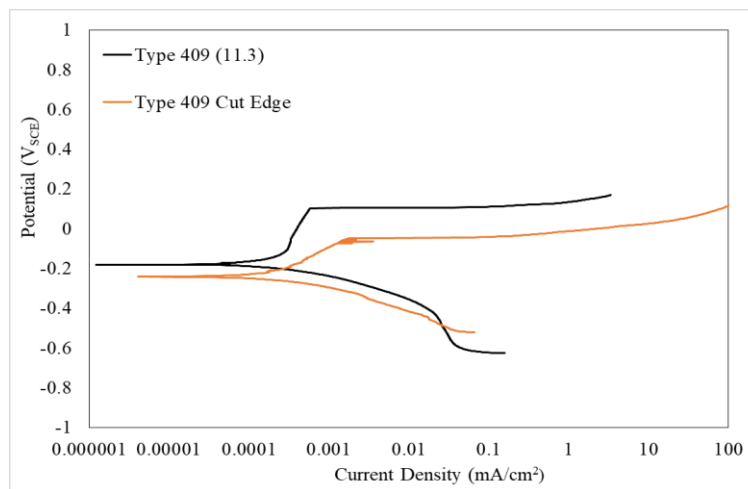
Figure 41: Potentiodynamic curve in 5% NaCl heat to 35 °C

This cut edge corrosion phenomena is not replicated by Type 439 and Type 436, which implies

even though both factors (increase in dislocation density and size and distribution density of cathodic

TiN particles) apply, the passive layer present on the higher alloyed ferritic stainless steels is resistant enough to impede corrosion. Some staining is present on both samples surfaces as seen in Figure 16d and 16e, yet no pits were evident after sandblasting.

As-Received	Post 1000 h Exposure	Post Sandblasting
a)		
b)		
c)		
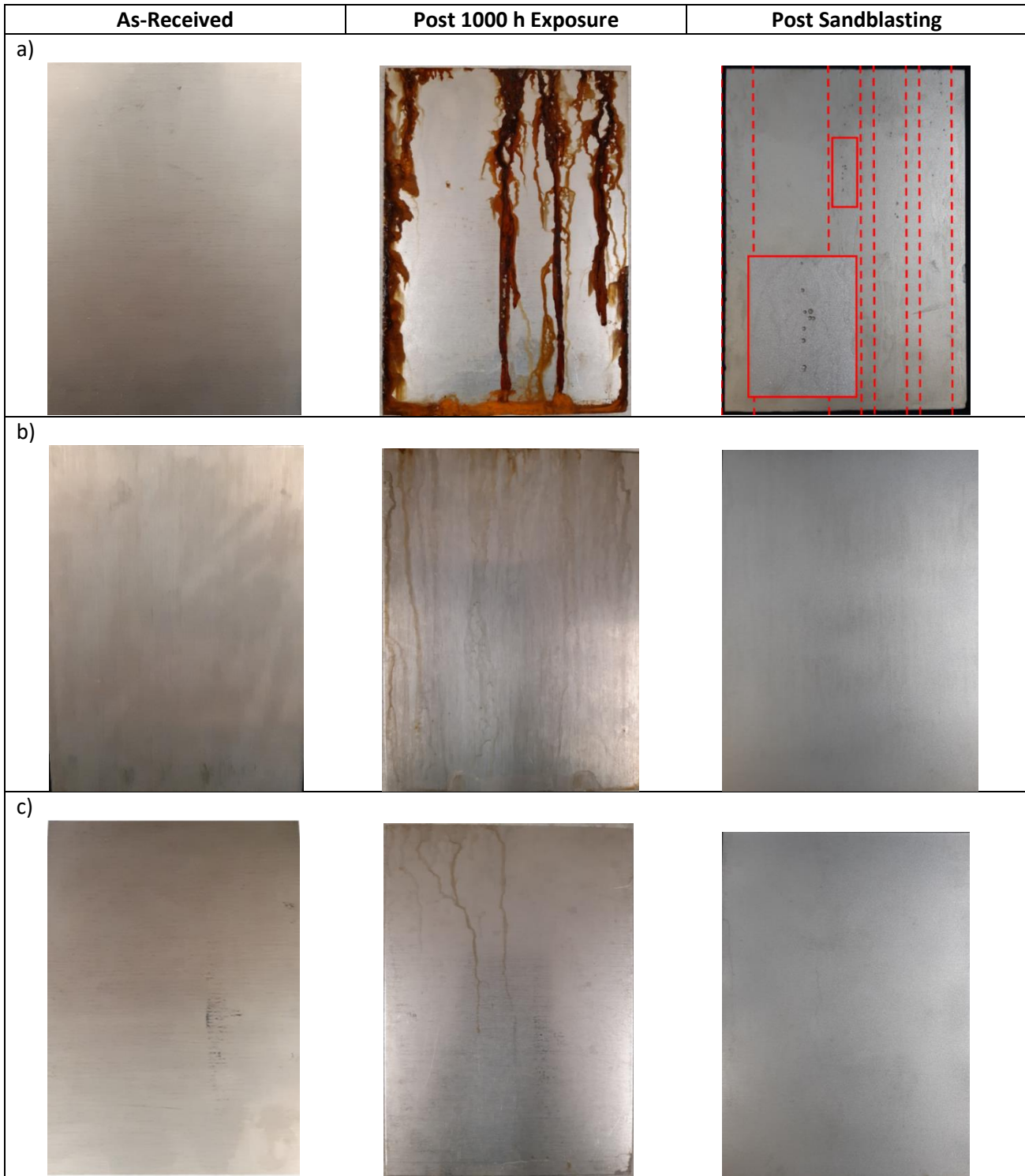
Figure 42: Images of monolithic panels before, during and post ASTM B117 1000 h exposure a) Type 409 b) Type 439 c) Type 436

Figure 43a depicts the Type 409Al surface after 500 h and 1000 h exposure. The white corrosion

product prominent on the surface after 500 h is presumably $Al(OH)_3$, demonstrating the sacrificial

dissolution of the Al-10%Si coating. Once the Al-10%Si coating was completely consumed, corrosion of the Type 409 substrate initiated, as evident by the red rust present after the 1000 h exposure. Only two pits were found on the Type 409 substrate after sandblasting, which is explained by the fact $Al(OH)_3$ is not conductive similar to $Fe(OH)_3$ [59], and, therefore underdeposit corrosion does not occur. The XHOM samples shown in Figure 43b initiated corrosion at the edge due to the galvanic couple between the noble chromized surface layer (cathode) and the much less noble IF steel substrate (anode). This cut edge corrosion, similar to Type 409, led to corrosion product migrating down the samples surface. After removal of the corrosion product via sandblasting, one singular pit curiously surrounded by a depressed ring was found on the surface under the migrated corrosion product. The corrosion resistance of XHOM with masked edges was also tested, isolating the prime surface in this measurement. As can be seen in Figure 43c, the surface was unaffected by the 1000 h exposure to 5% NaCl salt fog. This result is suggests that the pit found on the surface of the unmasked XHOM, was solely due to the underdeposit pitting caused by the corrosion product which migrated from the cut edge.

As-Received	Post 1000 h Exposure	Post Sandblasting
a)	500 h / 1000 h	
b)		XHOM 3
c)		
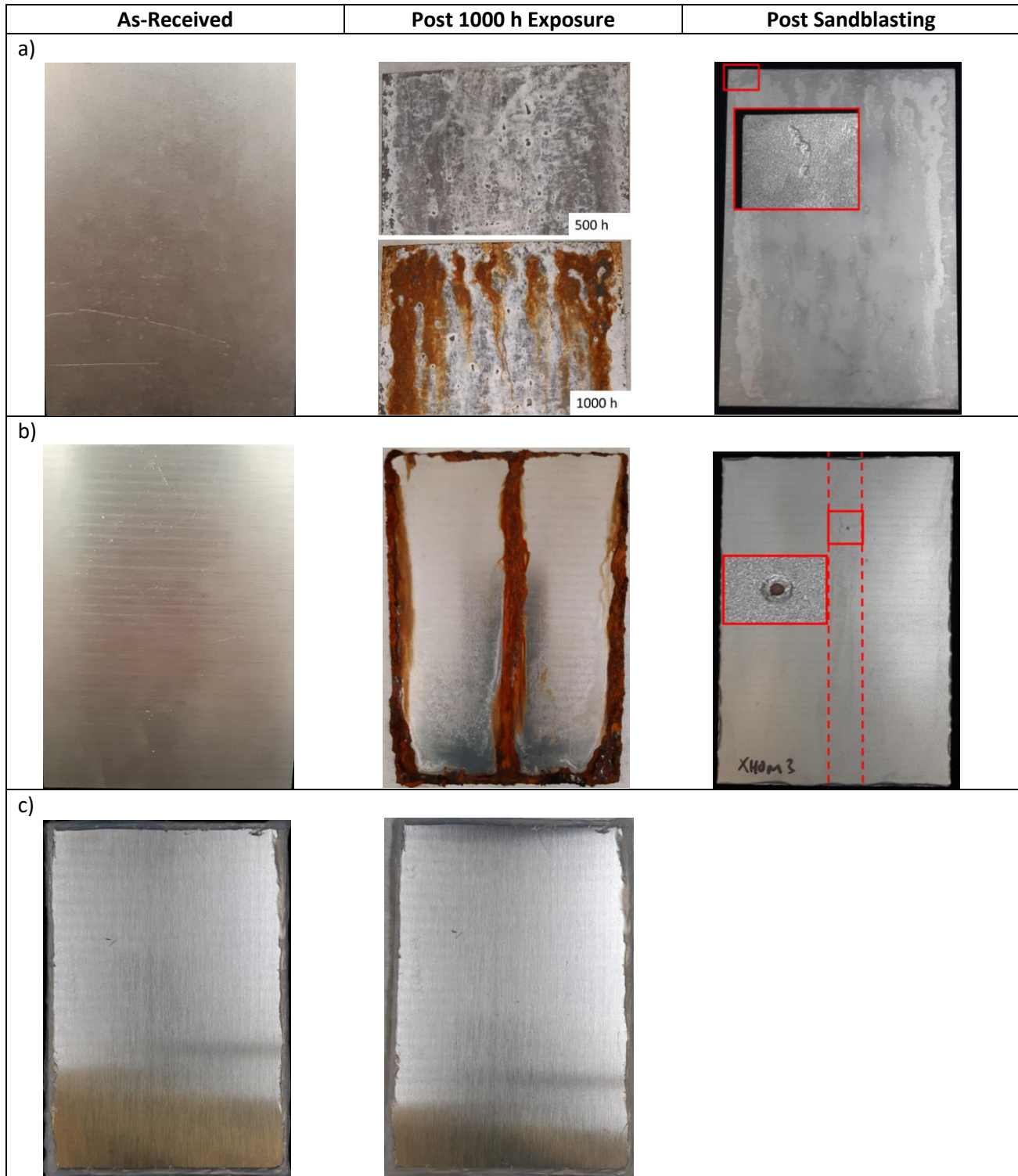
Figure 43: Images of multi-layered panels before, during and post ASTM B117 1000 h exposure a) Type 409Al b) XHOM c) XHOM Masked

Drain holes that are present in the outer shell of the muffler to allow exhaust gas condensate to escape, provide a cut edge exposed to both salt corrosion from the exterior environment and exhaust

gas condensate from the interior environment. Two methods are commonly used to manufacture the drain holes including drilling and punching. To determine if the influence of either manufacturing method plays a role in the corrosion resistance of the cut edge, samples containing both a drilled and punched hole, complete with masked panel edges, were tested. The images of XHOM presented in Figure 44a show that both drain holes corroded, yet at first glance the punched hole produces more corrosion product implying a lower corrosion resistance, yet this was not case when analyzing the sandblasted surface. After sandblasting, the diameter of the depressed ring (corrosion) surrounding the drilled hole was larger than that of the punched hole. The Type 409 sample containing a drilled and punched drain hole is shown in Figure 44b. At first glance the drilled hole seems to produce more corrosion product than then punched drain hole, and after sandblasting this initial observation holds true.

As-Received	Post 1000 h Exposure	Post Sandblasting
a)		
b)		
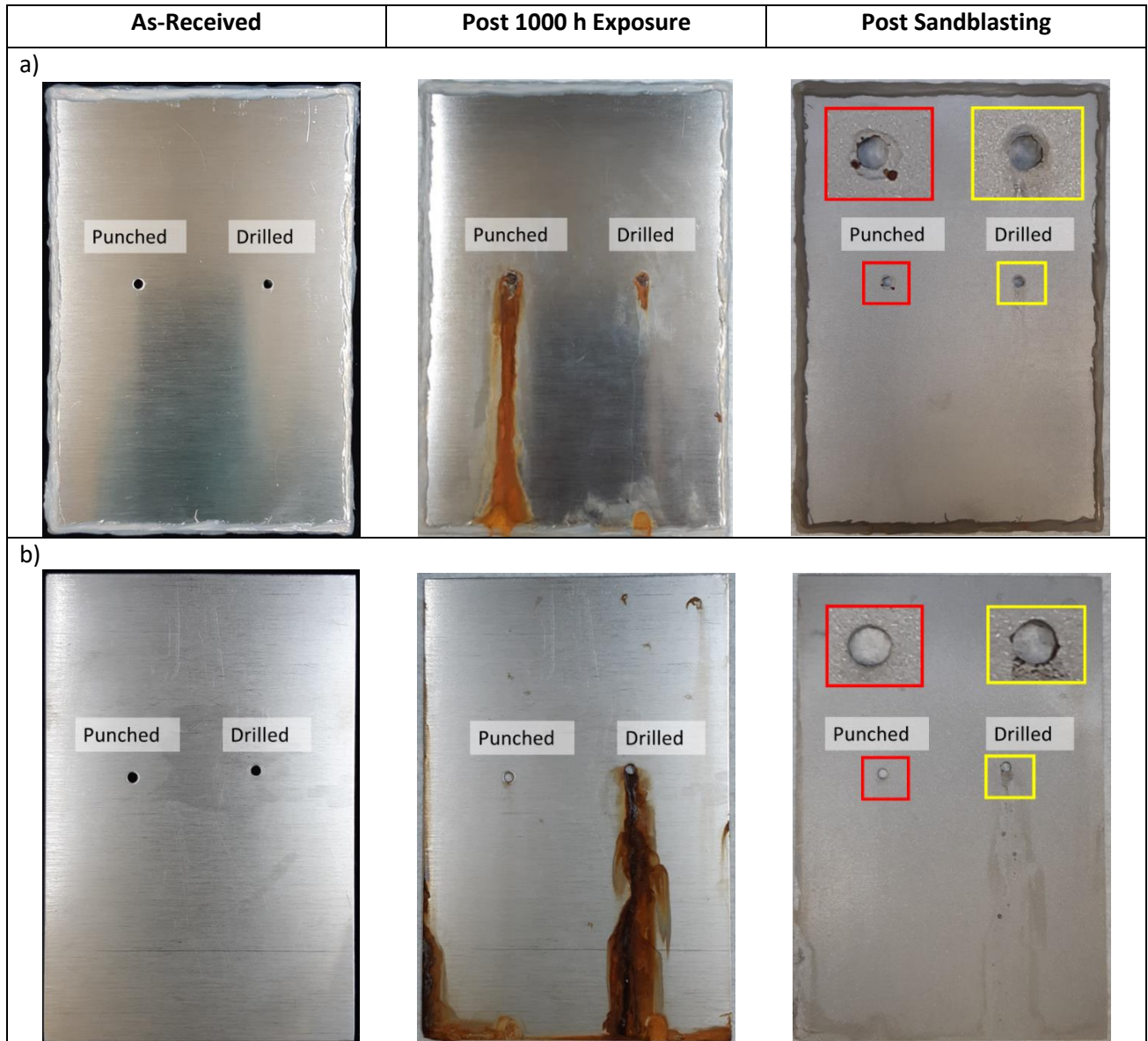
Figure 44: ASTM B117 panel post ASTM B117 1000 h exposure a) XHOM with drain holes b) Type 409 with drain holes

Cross-sectioned samples of the ND-TD plane and ND-RD plane are shown in Figure 45, illustrating both pit shape and depth. Figure 45a presents the cross section of the deepest pit found on the Type 409 surface located underneath the corrosion product, which migrated from the top edge. The pit on the surface has a shallow depth of 309 µm, compared to the cut edge pit with a depth of 700 µm. This difference in pit depth is expected due to the time difference in pit growth, as the cut edge pit initiated first leading to the migration of corrosion product initiating underdeposit pitting. The shape of

the pit on the surface is unlike those typically found on stainless steels in the presence of Cl⁻, yet similar

to those found after underdeposit pitting [34]. Type 436 and 439 show no evidence of localized

corrosion, which is consistent with the panel images in Figure 42.

Material	Type 409	Type 439	Type 436
Surface cross section	a)	b)	c)
Edge plan view			
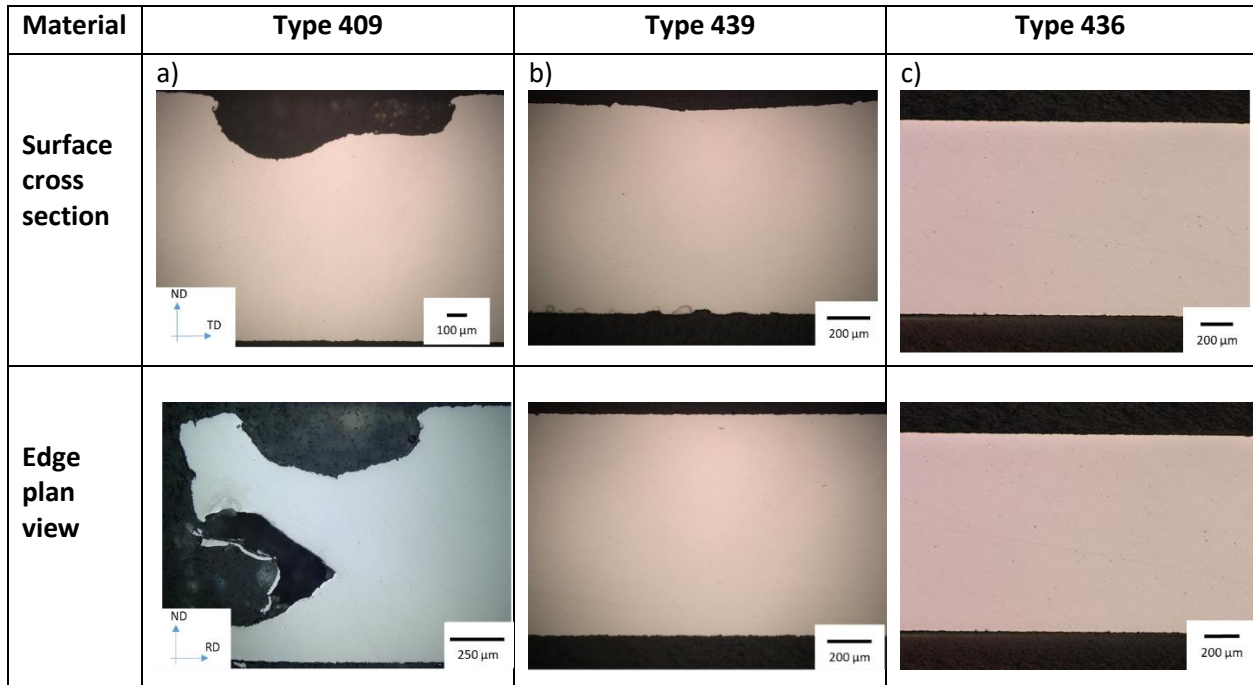
Figure 45: Cross-sections of monolithic alloy samples exposed to ASTM B117 for 1000 h a) Type 409 b) Type 439 c) Type 436

Type 409Al shows evidence of shallow pits on the surface of only 90 µm, in Figure 46a. This is expected

as corrosion of the Type 409 substrate, when exposed, is impeded by the cathodic protection of Al-

10%Si coating. After approximately 500 h of exposure, the coating was completely consumed by the

production of $Al(OH)_3$ and corrosion of the substrate began. As $Al(OH)_3$ is not conductive [59],

underdeposit pitting did not occur on the Type 409Al surface until a sufficient volume of $Fe(OH)_3$

formed, which can be seen in Figure 43a. The XHOM materials experience corrosion in a different way

than Type 409Al, as a result of the different roles in the galvanic couple. The cross section of the sole pit

that formed on the XHOM surface is shown in Figure 46b. The pit penetrated the coating, reaching the

substrate and due to the galvanic couple between the coating and the substrate, corrosion began

attacking the coating/substrate interface. This finding is interesting as it may prove beneficial for an exhaust component by extending component life. A though thickness pit is detrimental to an exhaust component as harmful gases as well as noise pollution can escape. The depth of attack on the cut edge shown in Figure 46b is severe as over a 1 mm of the IF steel substrate has been removed from each edge of the panel. The cause of the depressed rings surrounding the surface pit and drain holes became clear, as it is due to corrosion of the IF steel substrate leaving the remaining coating held up by its own structural integrity. Therefore, once the surface was sandblasted, the applied force caused the depression of the coating.

Material	Type 409Al	XHOM
Surface cross section	a)	b)
Edge plan view		
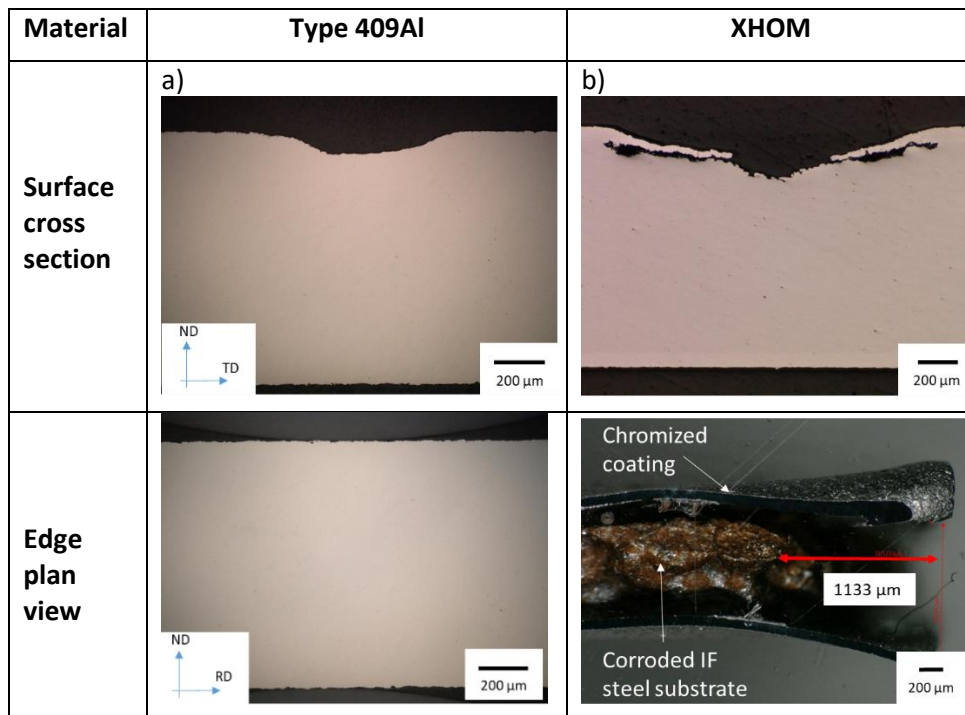
Figure 46: Cross-sections of multi-layered samples exposed to ASTM B117 for 1000 h a) Type 409Al b) XHOM

A corrosion rate for each material was calculated using the mass loss data (Equation (10)) and plotted in Figure 47. For the calculation, W represents the mass loss (g) measured after completion of exposure, D represents the density (g/cm^3), A represents the surface area (cm^2) and t represents the exposure time (h).

$$r = 87.6 * \left(\frac{W\ (g)}{D\left(\frac{g}{cm^3}\right) * A(cm^2) * t(h)} \right) \ (10)$$

XHOM exhibits the highest corrosion rate due the cut edge corrosion shown in Figure 20b, yet when the

edges are masked, XHOM exhibits a corrosion rate comparable to the highly alloyed ferritic stainless

steels, Type 439 and 436. This illustrates the high corrosion resistance of the XHOM surface depicted in

the polarization curves in Figure 40 where the cut edge was not exposed. The corrosion rate of Type

409Al is higher than that of bare Type 409, which reflects the uniform dissolution of the Al-10%Si

coating and the pitting corrosion on the bare Type 409. A better representation of the difference in

corrosion resistance between Type 409Al and 409 is the maximum pit depth. The maximum pit depth of

Type 409 is 7× that of Type 409Al and the pitting density is 25× that of Type 409Al. These properties

exemplify the real difference in corrosion resistance between the bare and aluminized Type 409.

Material	Maximum Pit Depth (µm)	Pitting Density (# of pits/cm²)
Type 409	700	0.175
Type 409Al	90	0.007
XHOM	272	0.003
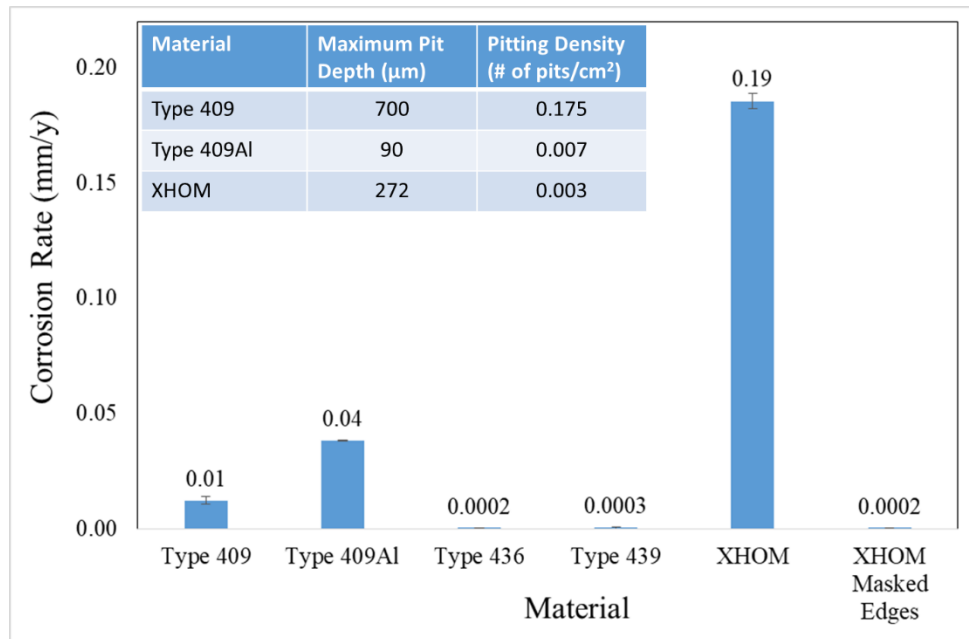
Figure 47: Corrosion rate of materials calculated from ASTM B117 results

4.3.3 Influence of Drain Hole Manufacturing Method

To investigate the cut edge corrosion effect of the two drain hole manufacturing methods applied to the

XHOM material, samples were mounted, etched and imaged using LOM and SEM seen in Figure 48 and

Figure 49. The punching method is shown to deform the drain hole edges inward leading to the chromized coating stretching across the exposed cut edge. The SEM-EDS Cr map in Figure 48d illustrates the depth of the stretched coating, covering nearly the entire cut edge, yet exposing a small region displayed in Figure 48f. This exposed region ensures contact of the corrosive solution with the IF steel substrate, and thus subsequent cut edge corrosion will occur. The drilled hole is not protected by a thin Cr-rich coating stretched across the cut edge therefore exposing more surface area of the cut edge to the corrosive solution. SEM-EDS Cr maps shown in Figure 49d & 49f, illustrate the larger exposed area of the drilled cut edge compared to the punched cut edge. These maps indicate the drilled cut edge is not protected and, therefore will corrode at a faster rate than that of the punched hole.
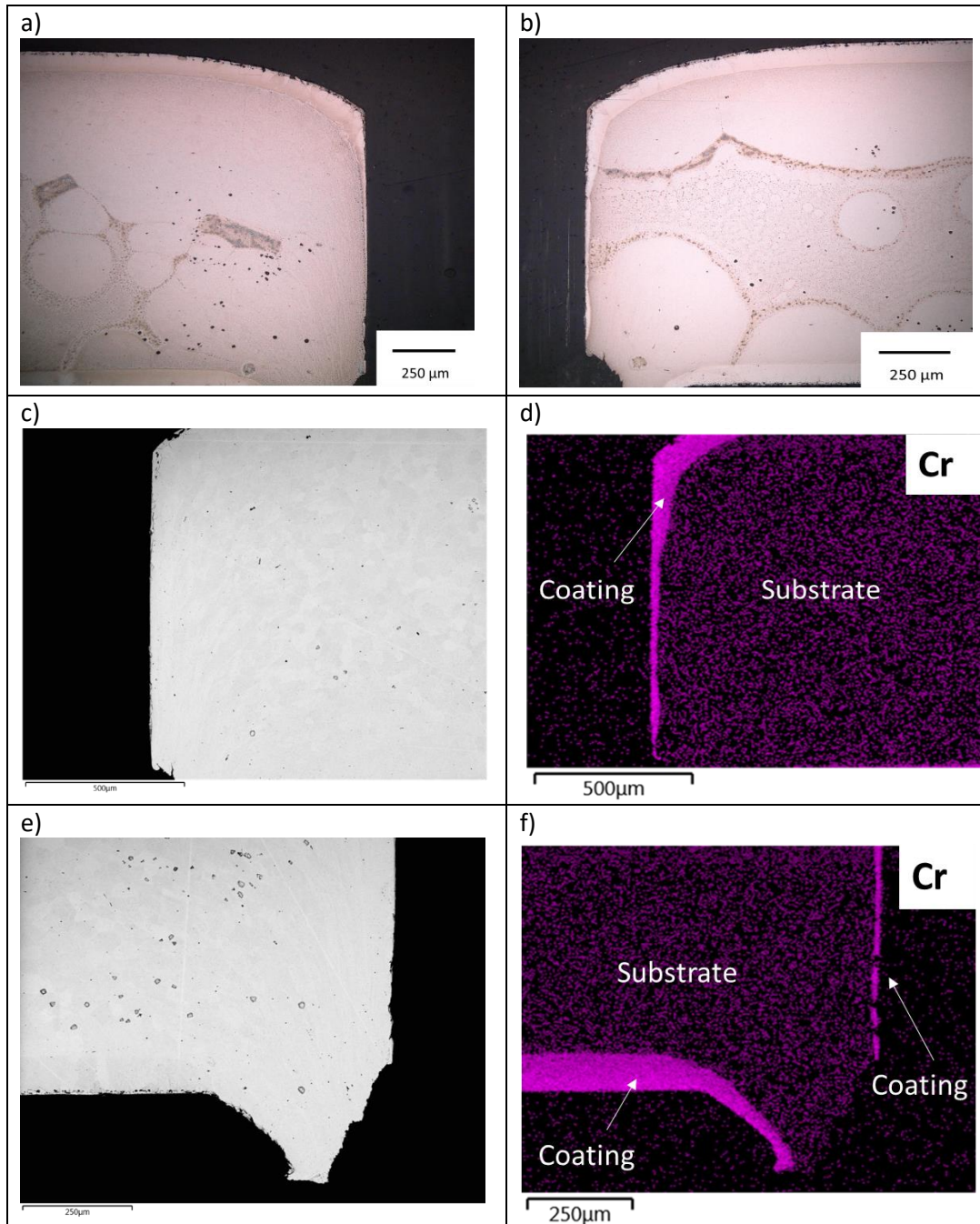
Figure 48: Images of punched drain hole cross-section a) LOM image of cross-section b) LOM image of cross-section c) SEM image of cross-section d) SEM-EDS Cr map of punched hole cross-section e) SEM image of punched hole cross-section f) SEM-EDS Cr map of punched hole cross-section
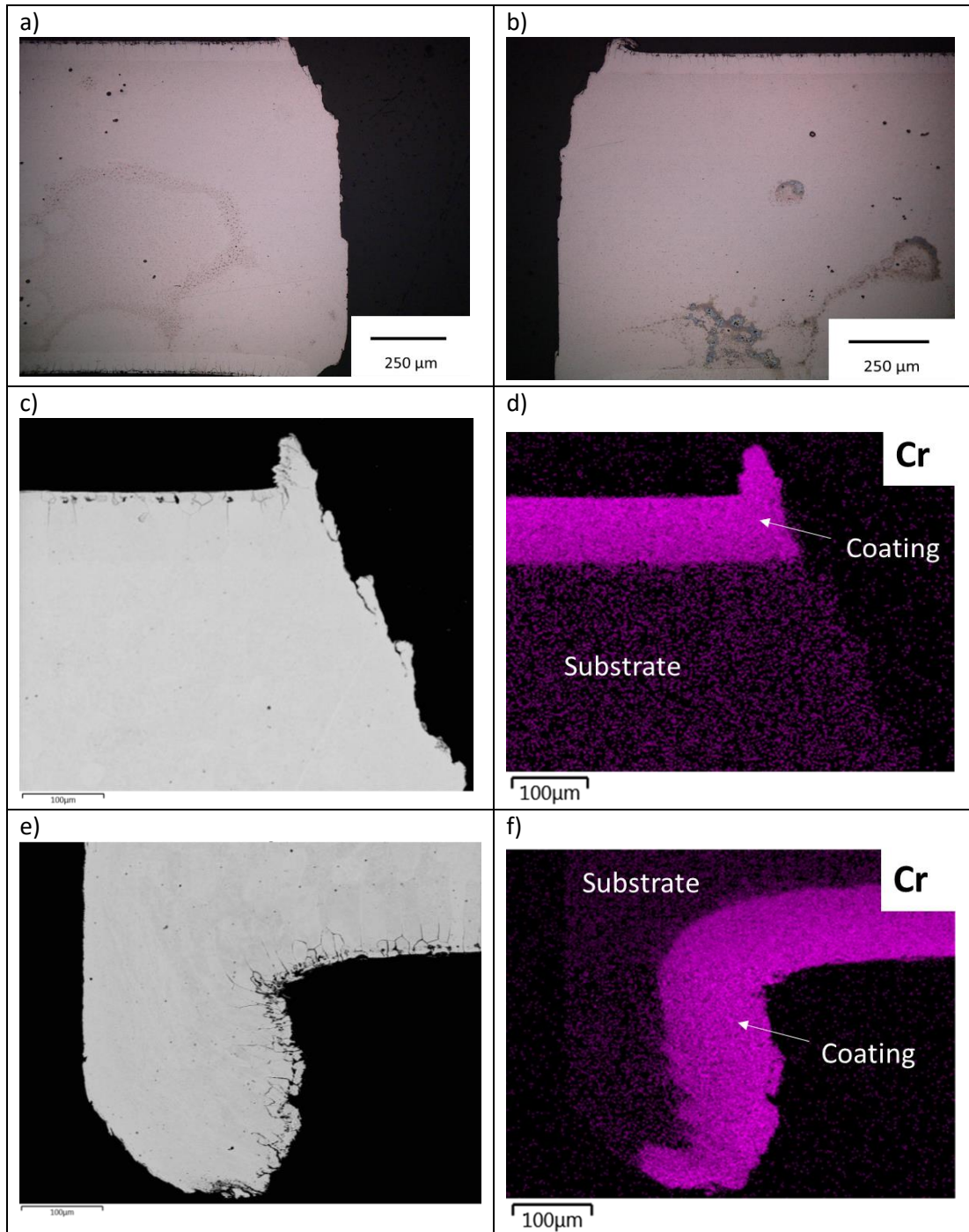
Figure 49: Images of drilled drain hole cross-section a) LOM image of cross-section b) LOM image of cross-section c) SEM image of cross-section d) SEM-EDS Cr map of drilled hole cross-section e) SEM image of punched hole cross-section f) SEM-EDS Cr map of drilled hole cross-section

The thin stretched coating covering the cut edge of the punched hole proves to retard the corrosion of

the IF steel substrate evident by a depth of corrosion difference of 300 µm experienced by the punched

drain hole cut edge compared to the drilled drain hole cut edge. Regions near the coating/substrate

interface corrode more rapidly than the central region of the substrate. This is likely caused by the high

driving force for corrosion at the interface due to the galvanic couple, similar to the attack seen at the

interface after the penetration of the surface pit in Figure 46b. The drilled cut edge does not experience

this phenomenon to the same degree as the punched cut edge, which is most likely due to the faster

corrosion rate of the substrate in the absence of a thin stretched chromized coating retarding corrosion.

This effect is highlighted by a red square on each of the images in Figure 50.
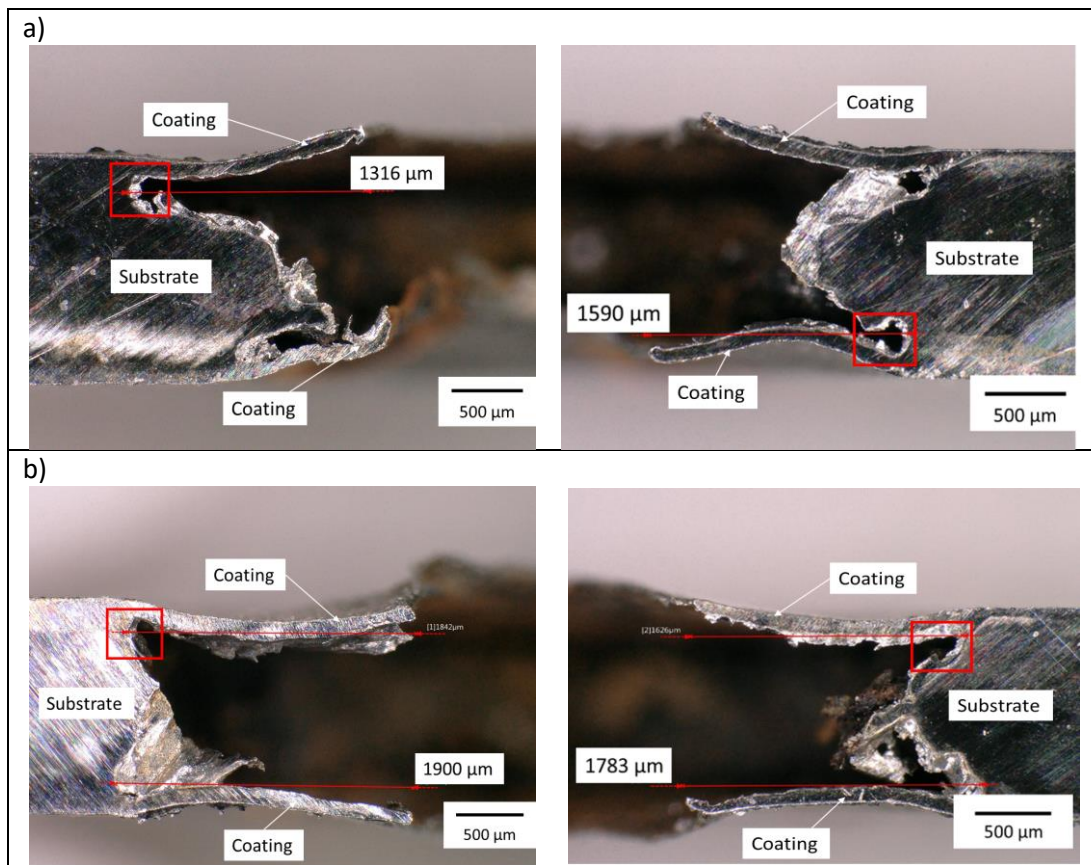
Figure 50: LOM images of XHOM drain hole cross-sections after ASTM B117 exposure a) punched drain hole b) drilled drain hole

Type 409 samples containing drain holes were analyzed as well after salt spray exposure, depicting the

difference in corrosion resistance between the XHOM cut edge and Type 409 cut edge. Both drain holes

of the Type 409 sample exhibit less significant attack compared to XHOM, yet there is a clear difference

between the punched and drilled drain hole of the Type 409 sample, shown in Figure 51. The drilled

drain hole experiences a more aggressive attack resulting in the migration of corrosion product down

the sample, causing underdeposit pitting of the surface. Once the corrosion product was removed,

localized corrosion was visible similar to that seen in Figure 42a. The punched hole experienced merely

staining of the cut edge demonstrating the difference in induced strain caused by drilling and punching a

drain hole. From these results punching seems like the clear manufacturing choice for manufacturing

drain holes on the outer shell of the exhaust muffler.

	Type 409 Punched Hole	Type 409 Drilled Hole
Cross-Section	a)	b)
Plan View		
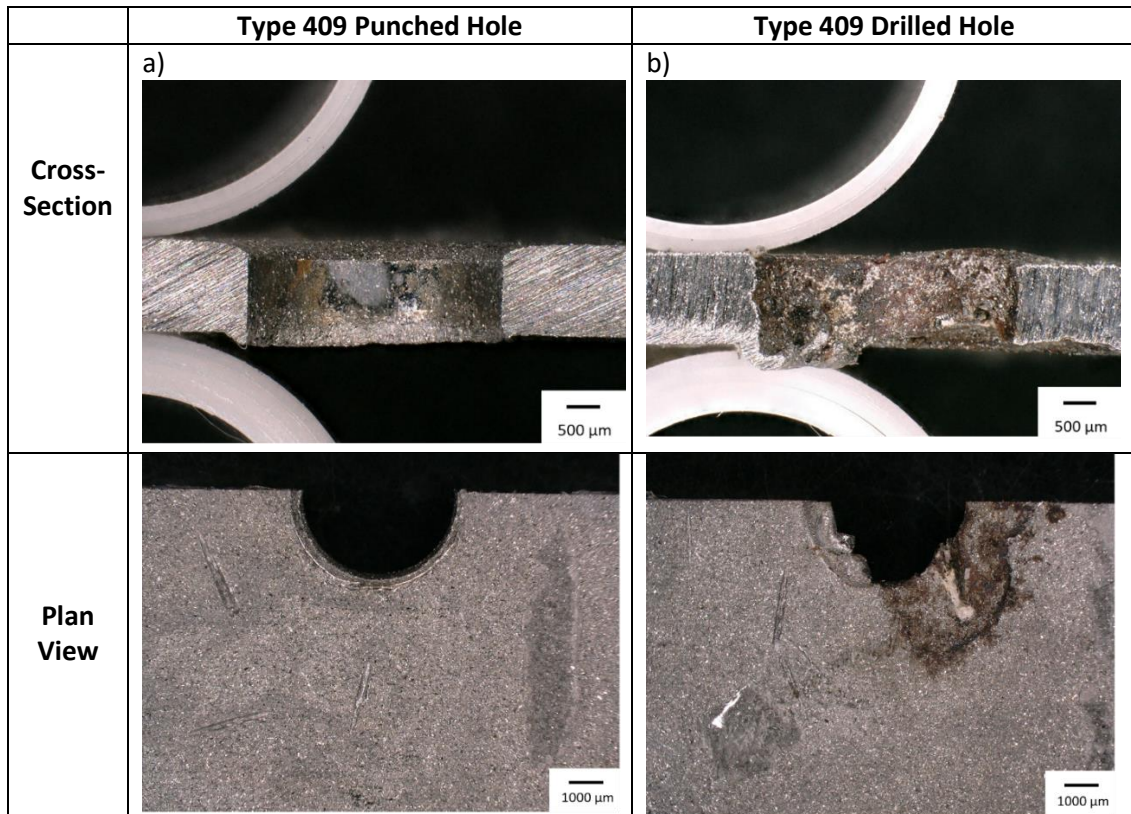
Figure 51: LOM images of Type 409 drain holes after ASTM B117 exposure a) Punched drain hole b) Drilled drain hole

4.3.4 Effect of strain

The above results indicate that strain has a large effect on the corrosion resistance of Cr-lean

ferritic stainless steels. According to G. Lu *et al.* [25], strain can influence the corrosion resistance

stainless steel by the occurrence and movement of dislocations leading to plastic deformation and

defects on the surface. The applied stress decreases the corrosion resistance of cut edge by increasing

the stored Gibbs energy, decreasing the electrochemical potential and, therefore increasing the driving

force for corrosion, Equation 11 [26]. Equation 12, demonstrates the effect of dislocations on the donor

density within the passive film. M represents metal, $V_{\ddot{O}}$ represents oxygen vacancy and T is defined as

the dislocation formed at the metal/oxide interface. Hence, 1 mol of point defects (dislocations) forms

(x/2) mols of vacancies, therefore the more dislocations created through applied strain, the more

vacancies effecting the compactness of the passive film and the corrosion resistance [27]. According to

the PDM, the more oxygen vacancies formed, the more cationic vacancies can potentially form and

condense at the metal/oxide interface creating voids [21].

$$\Delta G = -Z * F \left(\frac{C}{mol}\right) * e(V) \quad (11)$$

$$M + T \rightarrow M_M + \frac{X}{2}V_{\ddot{O}} + Xe' \quad (12)$$
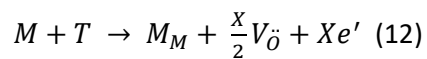
To measure the effect of strain on the corrosion resistance, XHOM and Type 409 were both strained to

different values and polarized in a 5% NaCl solution heated to 35 °C. First, Type 409 and XHOM tensile

samples were pulled to fracture as shown by the stress-strain results in Figure 52. As the UTS of each

material occurs at 20% strain, 5% and 10% were the strain values chosen at which to perform the

polarization curves. The polarization curves were then compared against the as-received curves shown

in Figure 40 curves to illustrate the effect of strain.
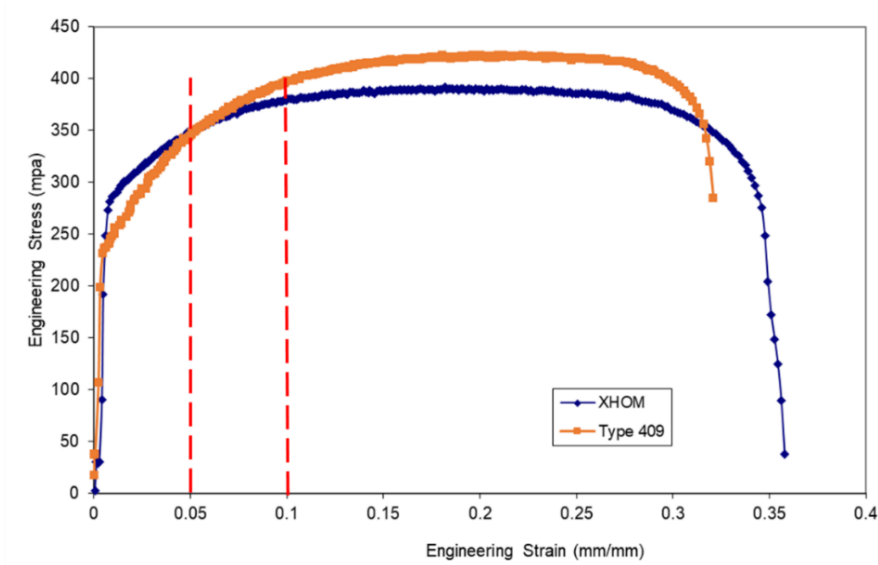
Figure 52: Stress-strain curve for XHOM and Type 409

Strained XHOM samples were first cross-sectioned, mounted, polished and are shown in Figure 53. The

XHOM prime and non-prime coating experience different surface treatments caused by the applied

strain. The XHOM prime surface is unaffected by the strain, whereas the non-prime surface is missing

sections of the skin layer due to the coalescence of pores. The pores present 10 μm below the surface

coalesce during pulling and sections are eventually removed. This phenomenon occurs at 5% and 10%

strain. The Type 409 surface is unaffected by the 5% and 10% strain, shown in Figure 54.

	5% Strain	10% Strain
Prime side	a)	b)
Non-prime side		
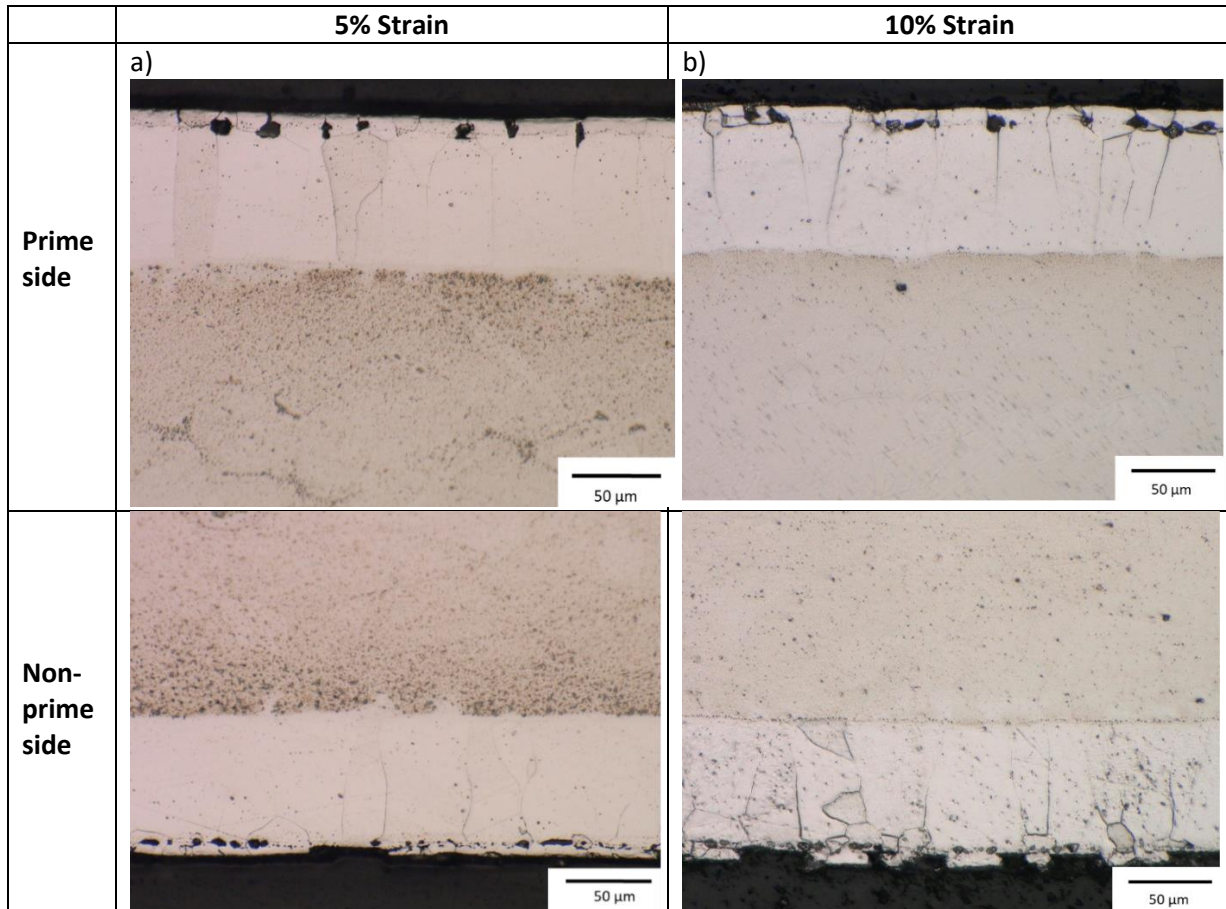
Figure 53: LOM cross-section images of strained XHOM a) 5% strain b) 10% strain

5% Strain	10% Strain
a)	b)
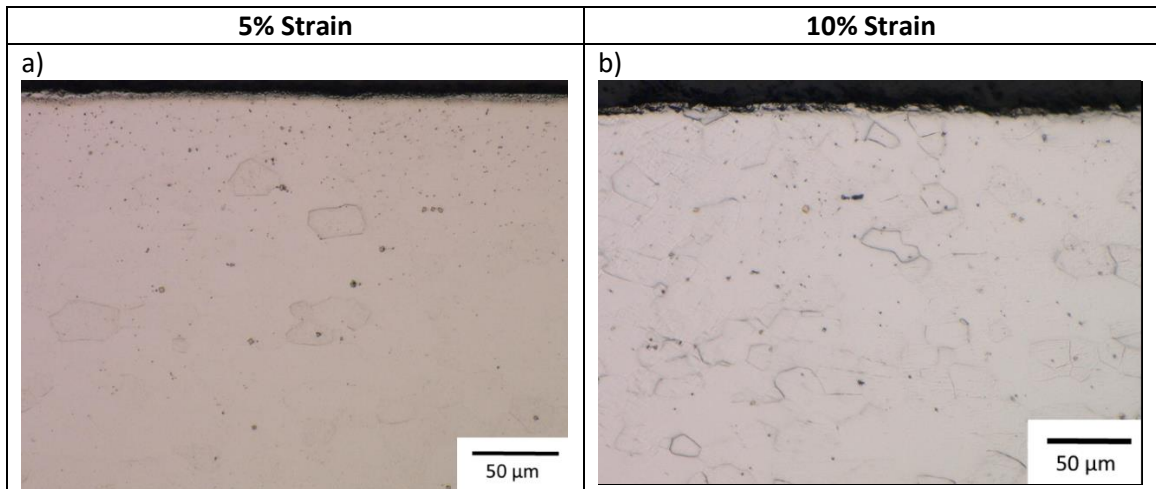
Figure 54: Cross section images of strained 409 a) 5% strain b) 10% strain

The polarization curves in Figure 55, illustrate the influence of strain on the localized corrosion resistance of the XHOM coating. Though the XHOM prime side cross-section appeared unaffected by strain, the E_b drops drastically after 5% and 10% strain. The drop in E_b of the XHOM prime side seems to

equal that of the non-prime side implying, the added surface roughness of the non-prime side is not the dominant cause of the E_b drop. One possible cause for the drop in E_b, may be due to cracking of the equiaxed grains induced during pulling, exposing the lower columnar grains which provide a direct path for corrosion to IF steels substrate. These polarization curves provide evidence that strain will play a major role in the cause of pitting on strained XHOM exhaust components.

a)   b)

Material	Pitting Potential (V)
XHOM P As-Rec	0.53
XHOM P 5%	0.23
XHOM P 10%	0.007

Material	Pitting Potential (V)
XHOM NP As-Re	0.42
XHOM NP 5%	0.19
XHOM NP 10%	-0.14
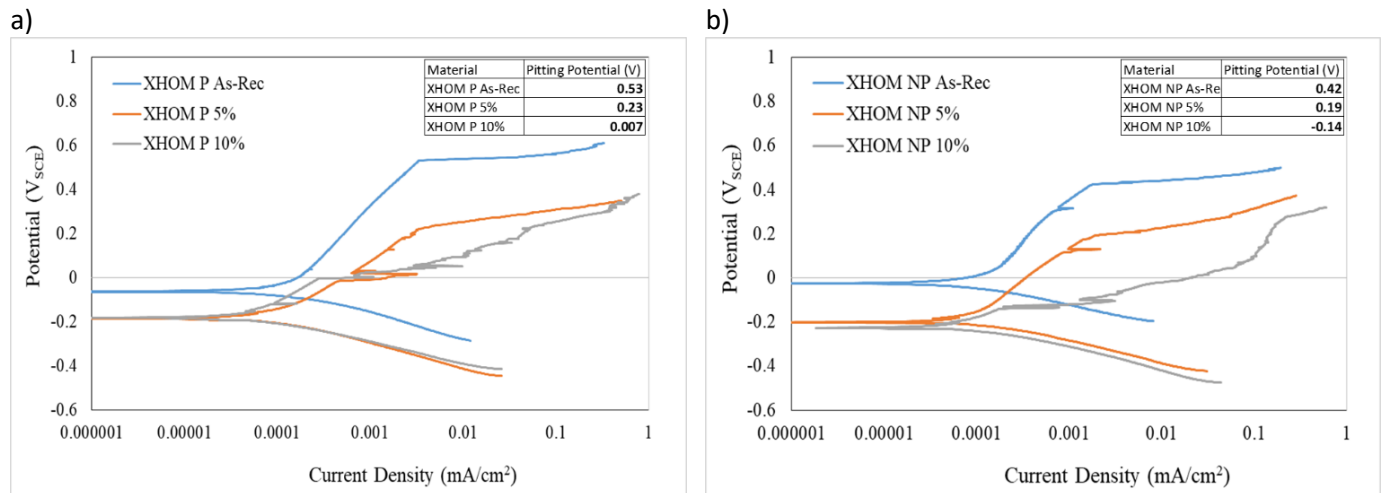
Figure 55: Polarization curve of strained XHOM in 5% NaCl solution heated to 35 °C a) Prime side b) Non-prime side

Figure 56 illustrates the polarization curve of Type 409, demonstrating the stability of the passive film at 0%, 5% and 10% strain. According to X. Si *et al.* [60], the pitting potential of Type 2205 (duplex stainless steel) is negligibly affected by deformation in a neutral 3.5% NaCl solution. Following this, it is concluded that an increase in dislocation density is not the cause of the decreased corrosion resistance of the Type 409 cut edges, the drop in E_b is solely due to the increased size and distribution of TiN particles.
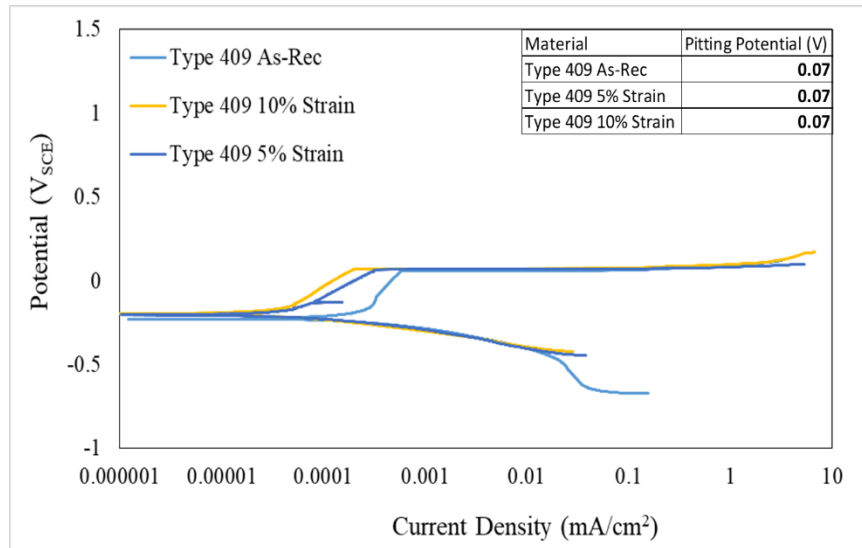
Figure 56: Polarization curve of strained Type 409 in 5% NaCl solution heated to 35 °C

When comparing the influence of strain on the corrosion resistance of XHOM and Type 409, it is clear

XHOM is affected where Type 409 is not. This phenomena is not well understood, yet is likely influenced

by the thickness of the passive film. As the Cr content increases, the thickness of the passive film

decreases, and therefore is more likely to be susceptible to plastic strain affecting performance. This

phenomena has been reported for a higher Cr content alloy, Type 430 [61].

4.4 Internal Corrosion Environment

As samples were heat treated for 1 h at 650 °C before testing in exhaust condensate exposure

environment, the Type 409Al as-received (Type 409Al-A) coating was affected as this heat treatment

surpasses the Al melting temperature. Type 409Al-A and heat treated Type 409Al (Type 409Al-H) were

analyzed using the SEM and XRD. SEM images of the Al-10%Si coating before and after the 1 h 650 °C

heat treatment can be seen in Figure 57a and 57b. The as-received coating is comprised of three distinct

layers: Type 409 substrate, IDL and Al-10%Si coating. After the heat treatment only two layers are

present: intermetallic phases and Type 409 substrate. Due to the multiple intermetallic phases present

within the heat treated coating, XRD was conducted to analyze which phases were present. As the

coating is only 15 μm thick, the electron beam penetrated through the coating picking up X-ray signals

from the substrate. This is shown by the high percentage of ferrite in the as-received coating. Elemental

Al and Si are present within the as-received coating, which is not unexpected as Si was shown to

segregate from the Al coating into Si-rich phases in Figure 30d, resulting in a fraction of coating

containing only Al. A complex $Al_9Fe_4MnSi_2$ phase is also present, most likely within the IDL. After the heat

treatment, similar phases to those discussed in Chapter, 2.1 $FeAl_3$, Fe_2Al_5 and $Fe_{2.7}Cr_{0.3}Si$ form due to the

rapid diffusion of Fe and Cr during the 650 °C heat treatment, causing the micro-cracks in the coating.

Micro-cracks are caused by the difference in thermal expansion coefficients of the intermetallic phase

[4], and can be seen penetrating the substrate in Figure 57b.
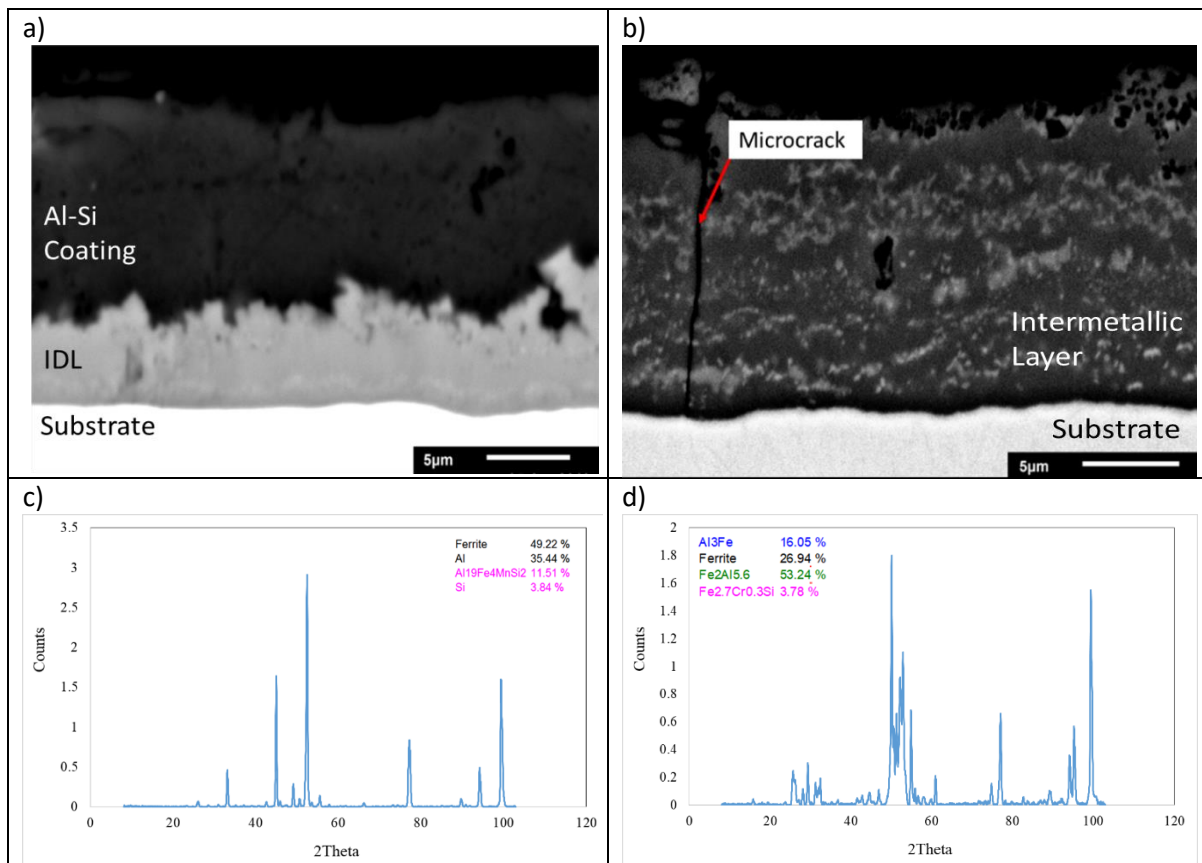
Figure 57: Type 409 Al before and after 1 h 650 °C heat treatment a) SEM-BSE image of as-received coating b) SEM-BSE image of heat treated coating c) XRD results of as-received coating d) XRD results of heat treated coating

4.4.1 Cyclic Exhaust Gas Condensate Exposure Results

Images of the monolithic samples, as-received, post exposure and after sandblasting can be seen in Figure 58. Type 409 corroded on all surfaces compared the ASTM B117 test where corrosion initiated solely at the cut edges. After sandblasting, pits can be seen distributed uniformly on the surface. Both Type 436 and Type 439 samples show evidence of corrosion along each surface, yet a handful of uncorroded regions are present. In Section 4.3.2, ASTM B117 samples corroded due to under deposit pitting, Type 436 and 439 samples in Figure 58b and 58c exhibit surface regions absent of oxide, which in turn are absent of pits. This indicates that the pitting which occurred on the Type 436 and 439 surface, was caused due to the same under deposit pitting phenomena which attacked Type 409 in the ASTM B117 environment.

As-Received	Post Exhaust Condensate Exposure	Post Sandblasting
a)		
b)		
c)		
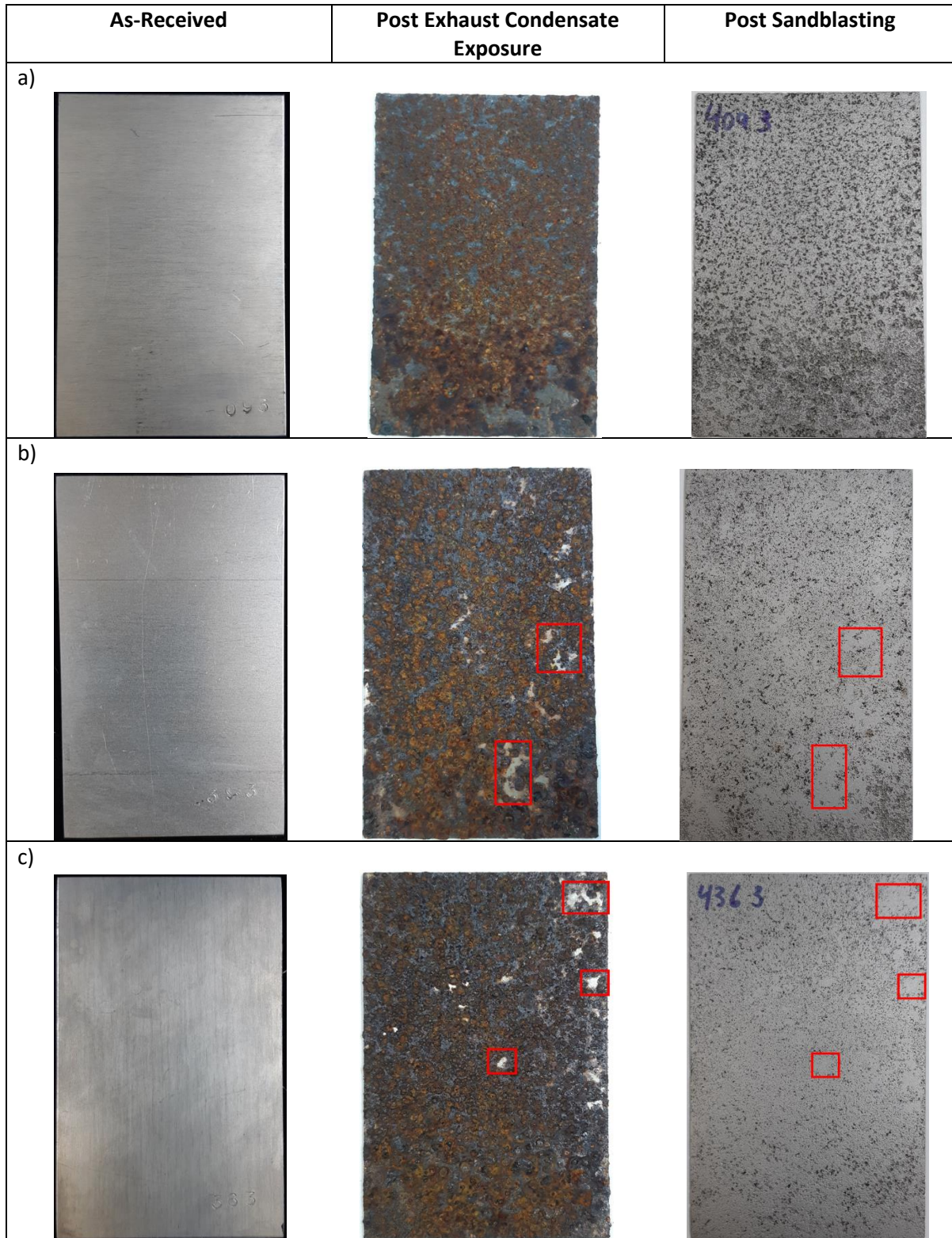
Figure 58: Monolithic panels before, during and post exhaust condensate exposure a) Type 409 b) Type 439 c) Type 436

As-received Type 409Al, shown in Figure 59, exhibits a high corrosion resistance with minimum pitting on the surface, compared to the heat treated aluminized material, which resembles Type 409. This result implies the heat treated Al-10%Si surface no longer provides galvanic protection for the Type 409 substrate, explaining the similarity in the pitting densities between Type 409Al-H and Type 409. XHOM corroded heavily similar to Type 409, leaving no regions absent of corrosion product or absent of pits after sandblasting.

As-Received	Post Exhaust Condensate Exposure	Post Sandblasting
a)		
b)		
c)		
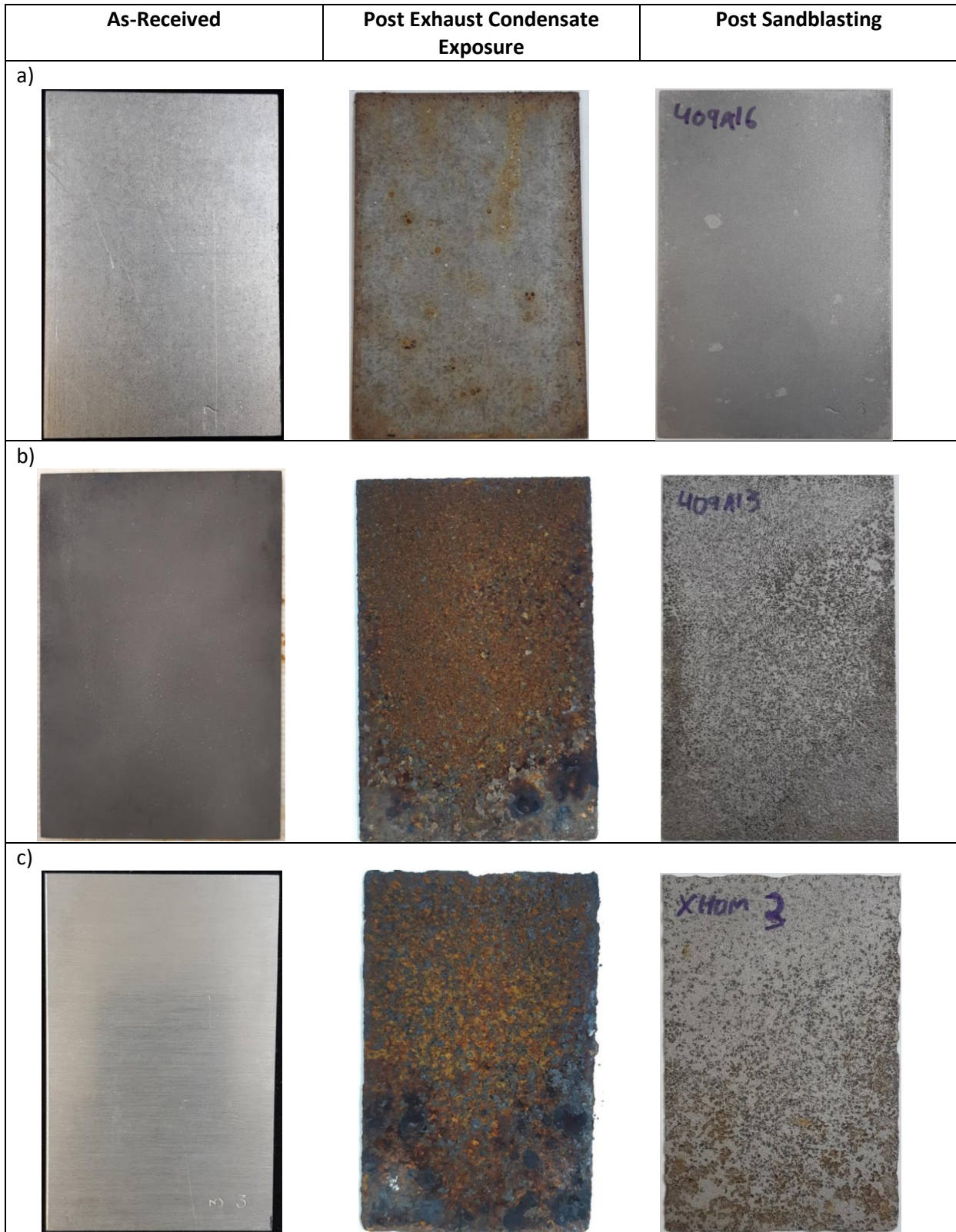
Figure 59: Images of as-received, post 9 week exposure and post sandblasting samples a) Type 409Al-A b) Type 409Al-H c) XHOM

Low and high mag LOM images of monolithic cross-sections are shown in Figure 60, illustrating the maximum pit depth of each material. Type 409 exhibits the deepest pit of the monolithic materials, which is expected due to lower Cr content, while Type 436 outperforms Type 439 due to the Mo addition, impeding pit growth.

Low Mag LOM image	High Mag LOM image
a)	
b)	
c)	
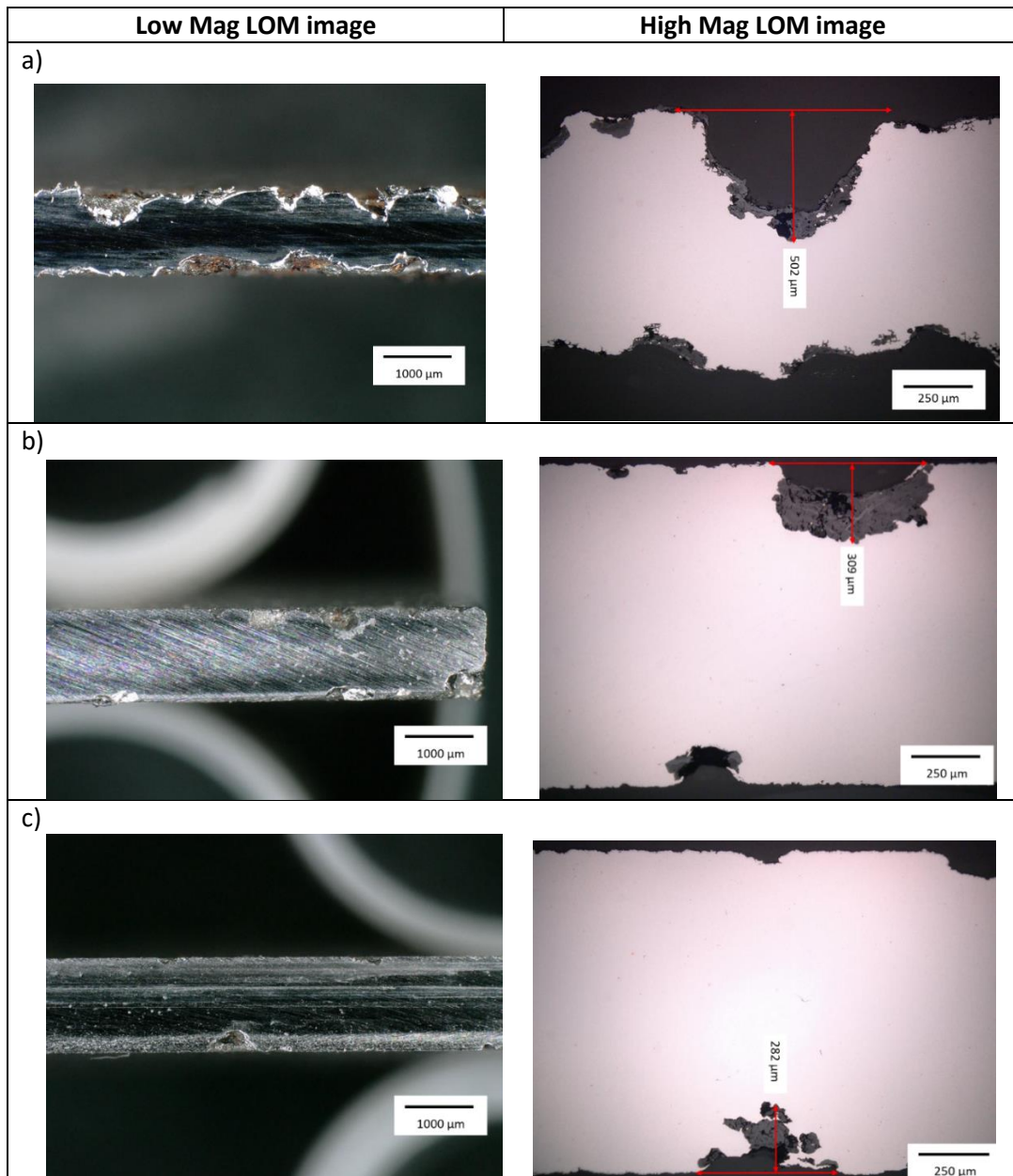
Figure 60: LOM images of monolithic cross-sections post exhaust gas condensate exposure a) Type 409 b) Type 439 c) Type 436

Images of the multi-layered material cross sections are shown in Figure 61, illustrating the difference in maximum pit depth between the as-received and heated Type 409Al. The maximum pit depth of Type 409Al-H is 200 μm deeper than bare Type 409, which could be due to the loss of the galvanic protection by the aluminum coating as well as micro-cracks in the heat treated Al-10%Si coating, behaving as crevices inducing crevice corrosion. XHOM does not exhibit similar corrosion behaviour to the delamination which occurred in the ASTM B117 environment, due to the aggressiveness of this test. Once pits penetrate the substrate, the substrate is attacked and not galvanically protected by the driving for corrosion at the substrate/coating interface, as shown in Figure 46b.

Low mag LOM Image	High mag LOM Image
a)	
b)	
c)	
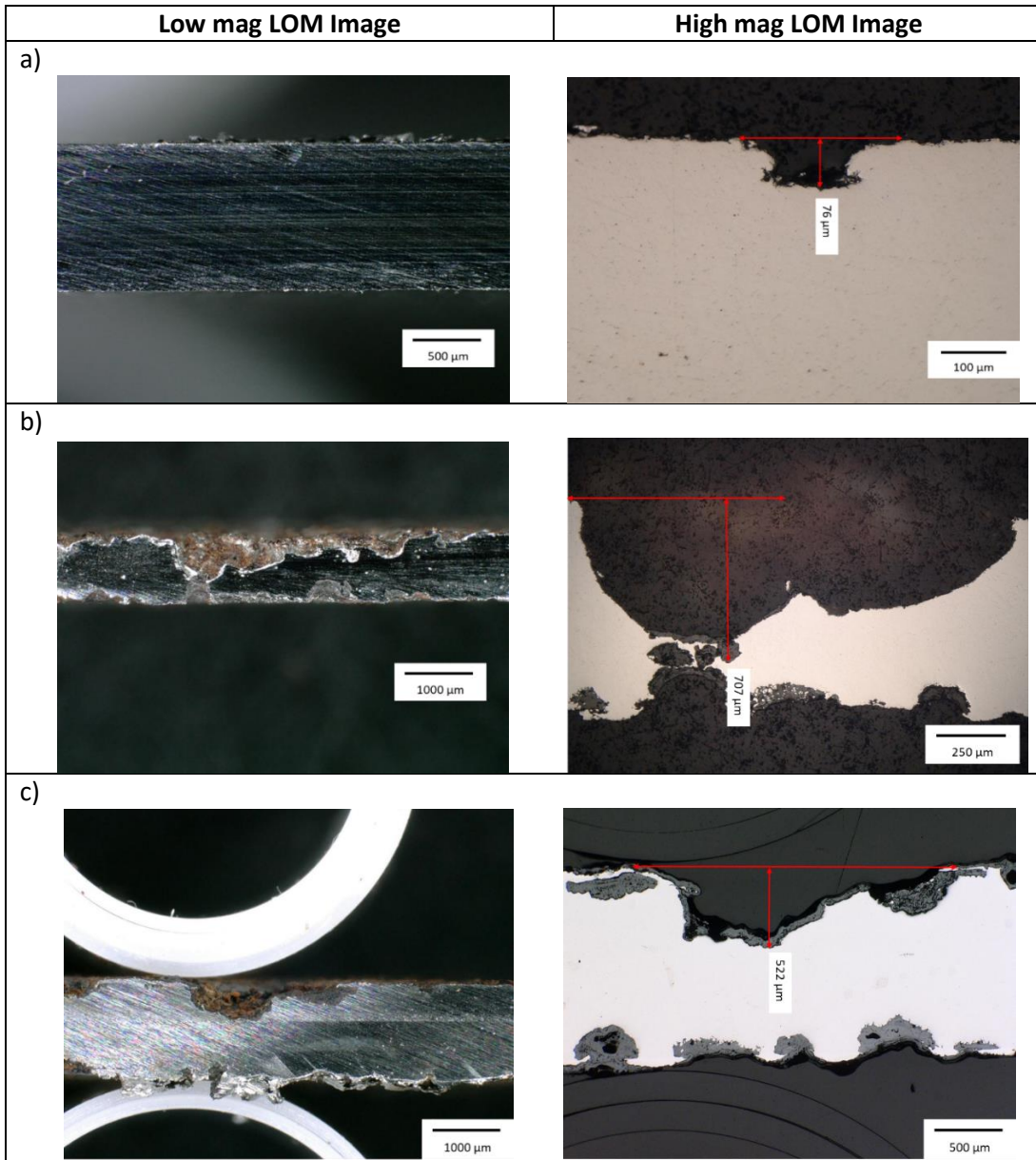
Figure 61: LOM images of multi-layered material cross-sections post exhaust gas condensate exposure a) Type 409Al (As-received) b) Type 409Al (heat treated) c) XHOM

The corrosion rate of each material was calculated using Equation 10, and is plotted along with the corresponding maximum pit depth in Figure 62. The performance of Type 409Al-A indicates the high corrosion resistance of an aluminized coating in an acidic environment, compared to the poor performance in a Cl^--rich environment. Type 409Al-A outperforms Type 409Al-H due to the loss of the galvanic protection via the intermetallic formation within the Al-10%Si coating. The performance of Type 409Al-H, is comparable to that of bare Type 409 implying the Al-10%Si coating no longer protects the

Type 409 substrate allowing corrosion to occur unimpeded. The corrosion rate and the maximum pit depth of XHOM is similar to that of Type 409, with the cut edge exposed, which is a promising result. This is promising because with the edges exposed in the external environment, XHOM performed inferior to the benchmark materials, yet with the edges with exposed in the internal environment, XHOM performs comparable to Type 409. Type 436 outperforms Type 439 in corrosion rate and maximum pit depth, which is due to the Mo addition retarding pit growth.

Material	Maximum Pit Depth (µm)
Type 409	502
Type 409Al-A	76
Type 409Al-H	707
XHOM	522
Type 439	309
Type 436	282
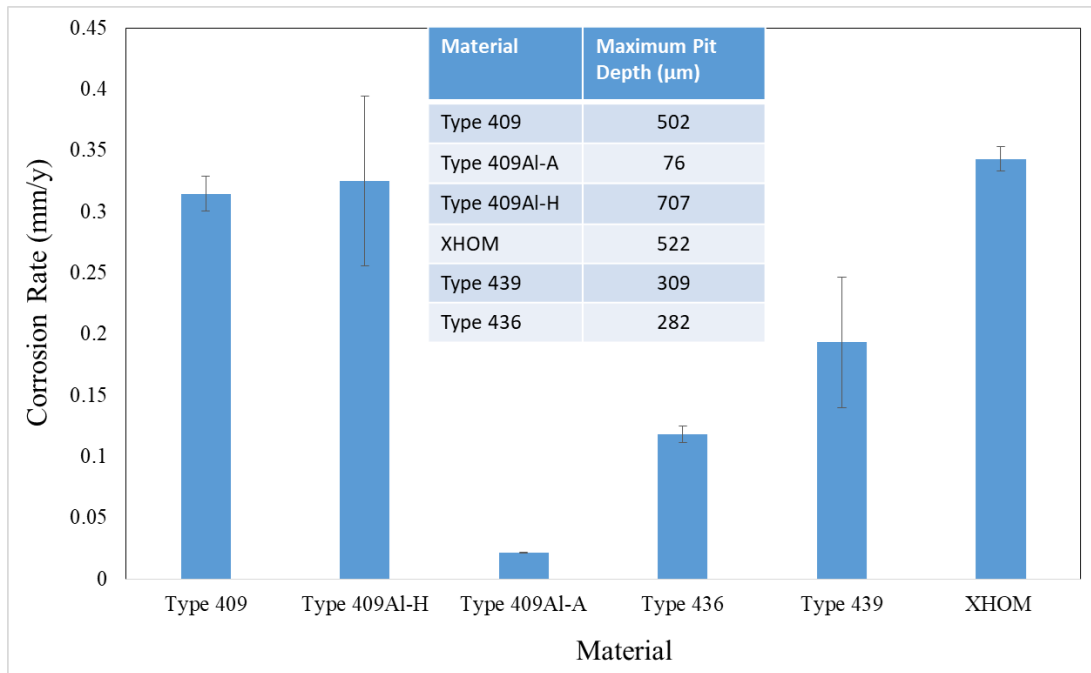
Figure 62: Corrosion rate of samples calculated from mass loss measurements post exhaust gas condensate 9 week exposure

5. Global Discussion

The objective of this study was to determine the suitability of a more cost-effective multi-layered material to replace current generation monolithic ferritic stainless steels for fabrication of automotive exhaust components. Multi-layered materials allow the decoupling of surface properties from bulk properties, enhancing the corrosion resistance of the surface while maintaining the mechanical properties of the bulk substrate. Aluminized Type 409 (Type 409Al) is currently widely used, as the Al-10%Si coating galvanically protects the Type 409 substrate extending the life of the material.

The cost of the Type 409Al is still rather high due to the stainless steel substrate, and the corrosion properties decrease drastically if temperatures reach 600 °C. For this reason the suitability of XHOM, a chromized IF steel with 40% Cr at the surface and 0% Cr in the bulk, was determined for this application. XHOM, along with the current generation benchmark materials were tested in simulated interior and exterior automotive exhaust environments.

During internal environment testing, materials are subjected to a heat treatment of 650 °C for 1 h. To measure whether this heat treatment would lead to sensitization within the materials, DLEPR testing was conducted on samples of each materials in the as-received condition and heat treated condition measuring the i_r/i_a ratio. The DLEPR results indicated that though Type 409 and 439 are sensitized in the as-received condition (without the heat treatment applied), all materials maintained the same i_r/i_a ratio after the heat treatment, indicating that further sensitization during service is not expected.

The results indicated that in the exterior (5% NaCl) environment, the corrosion resistance of XHOM is comparable to the highly alloyed stainless steels (Type 439 and 436) when the cut edges are masked concealing the galvanic couple. This galvanic couple is created by the more noble chromized layer (cathode) and much less noble IF steel substrate (anode). The effect of this galvanic couple was illustrated by XHOM exhibiting the highest E_b, yet also the highest corrosion rate when the cut edges of the XHOM panels were exposed. A difference in the corrosion resistance of the prime and non-prime side became apparent during potentiodynamic testing, caused by the Al_2O_3 particles embedded on the non-prime surface of the chromized layer, resulting in defects in the layer, such as increased roughness, pores and cracks.

Post ASTM B117 exposure, Type 439 and 436 showed no evidence of localized corrosion, unlike Type 409, which exhibited a significant pitting density on the surface. Corrosion of Type 409 initiated at the

edge due to cathodic TiN particles, which are larger along the cut edge (TD-ND, RD-ND) compared to the bulk surface (RD-TD). Corrosion product formed at the cut edge and migrated downwards resulting in under deposit pitting along the surface. Type 409Al demonstrated the sacrificial corrosion nature of the Al-10%Si coating, through the consumption of the coating to produce an Al-rich corrosion product. Once the coating was completely consumed (after about 500 h exposure) Fe-rich corrosion product began forming and shallow pits were found underneath after cleaning. The Al-10%Si coating showed no evidence of passivity in the potentiodynamic testing, which is consistent with the complete consumption of the coating.

XHOM experienced a similar corrosion susceptibility to bare Type 409 sample without masked edges, where corrosion product formed at the top edge and migrated down the surface resulting in under deposit pitting. The XHOM pit was unlike those on Type 409, due to the galvanic couple at the chromized layer/IF steel substrate interface. Once the chromized layer was penetrated, corrosion proceeded laterally along the interface, rather than through the thickness, serving to delaminate the coating.

To test whether the cut edge corrosion of Type 409 is influenced by the strain induced during shearing of the panel from the sheet material, flat dog bone tensile coupons of Type 409 and XHOM were strained to 5% and 10%, then corrosion tested, measuring the effect on the E_b. Type 409 was found to have no change in E_b, indicating that the cut edge corrosion is likely solely due to the exposed TiN particles along the cut edge. The corrosion susceptibility of XHOM proved to be more sensitive to strain as the E_b value decreased by 300 mV at both 5% and 10% strain, possibly caused by the exposure of the columnar grains present below the skin layer, which behave as straight paths for corrosion to reach the substrate.

The influence of drain hole manufacturing methods were tested in NaCl (aq) environment via ASTM B117 exposure. The results indicated that the punching method creates a smearing effect of the XHOM chromized layer partially covering and protecting the cut edge from corrosive media, unlike the drilling method which solely increases the surface roughness of the exposed cut edge. The smeared layer proved to retard cut edge corrosion of XHOM resulting in a lower depth of corrosion of the cut edge compared to the drilled drain hole. Type 409 was also tested and resulted in the drilled hole to leading to more corrosion. As Type 409 was tested and shown to not be affected by strain, the surface roughness caused by drilling is the main driving force for corrosion within the drain hole.

XHOM along with the benchmark materials were exposed for 1500 h to a cyclic exhaust gas condensate test, resulting in an XHOM corrosion rate comparable to Cr-lean Type 409. The higher alloyed ferritic stainless steels exhibited lower corrosion rates than XHOM and Type 409, yet no material outperformed Type 409Al-A. Each of the samples were heat treated (1 h @ 650 °C) to induce sensitization, yet one set of Type 409Al samples were not heat treated (Type 409Al-A) to determine the effect of the intermetallic formation of corrosion resistance. The corrosion rate of the Type 409Al-H is drastically increased compared to Type 409Al-A. This is likely caused by the loss of galvanic protection of the coating as well as the micro-cracks within the heat treated coating behaving as crevices: inducing crevice corrosion. When analyzing maximum pit depths, XHOM exhibited a pit depth only 20 μm deeper than Type 409, cementing that the performance of XHOM is comparable to a current generation ferritic stainless steel whilst remaining the advantage in formability and cost-effectiveness.

XHOM has proven to exhibit a comparable corrosion resistance to the highly alloyed ferritic stainless steels in both interior and exterior environment when the cut edges are masked. With cut edges exposed, the material will fail in the exterior environment, yet behave similarly to Type 409 in the interior environment. This study has clearly proven the validity and suitability of XHOM as an exhaust

component material, not only by exhibiting a similar life expectancy as the current generation ferritic stainless steels, but also by decreasing the cost and weight of the overall automotive exhaust system.

6. Conclusions

1. Type 409 and 439 DLEPR curves exhibit evidence of sensitization in the as-received condition (mill annealed), where no other materials experienced sensitization. Yet all materials experience no change in i_r/i_a ratio indicating whether sensitization occurred prior to installation or not, further sensitization will not occur during service.

2. XHOM prime and non-prime exhibit higher E_b values than benchmark materials in 5% NaCl environment indicating a lower localized corrosion susceptibility due to Cl⁻.

    a. E_b ranking: XHOM prime > XHOM non-prime > Type 436 > Type 439 > Type 409 > Type 409Al (did not passivate)

3. XHOM exhibited the highest corrosion rate during exposure to ASTM B117 conditions, due to the mass loss caused by the cut edge corrosion. The cut edge corrosion is a result of the galvanic couple created by the noble chromized layer (cathode) and the much less noble IF steel substrate (anode). When the cut edge was masked using silicone, the corrosion rate dropped drastically performing comparable to that of the highly alloyed ferritic stainless steel (Type 439 and 436).

4. Pitting of the XHOM material results in delamination of the coating due to the driving force for galvanic corrosion at the chromized layer/IF steel substrate interface once a pit penetrates the substrate.

5. Strain has a large effect on localized corrosion susceptibility of XHOM in 5% NaCl solution, dropping 300 mV after pulling sample to 5% strain and again after pulling to 10% strain. Type 409 exhibited no difference in localized corrosion susceptibility after applied strain. This is

believed to be due to a difference in passive film thickness, where a higher chromium content is associated with a thinner passive film and is therefore more susceptible to strain.

6. During the ASTM B117 exposure, Type 409 initiated corrosion at the cut edge forming corrosion product which migrated down the surface leading to under deposit pitting. The cut edge corrosion of Type 409 is due to the larger size and higher distribution density of active TiN particles along the exposed ND-TD plane, not the induced strain caused by shearing the material to sample dimensions.

7. Drain hole manufacturing method was shown to influence the corrosion susceptibility of Type 409 and XHOM in ASTM B117 conditions. The punching method proved to stretch the chromized layer of XHOM over exposed drain hole cut edge retarding corrosion, which did not occur within the drilled drain hole resulting in a larger depth of attack. Type 409 exhibited little to no corrosion within the punched drain hole yet extensive corrosion within the drilled drain hole, which may be due to a difference in surface roughness caused by drilling compared to punching.

8. Al-10%Si coating galvanically protected the Type 409 substrate in ASTM B117 conditions until fully consumed allowing localized corrosion of the substrate to initiate approximately 500 h into exposure. The corrosion rate of Type 409Al is misleading as the mass loss is primarily due to the coating consumption, where pit depth of bare Type 409 exceeded Type 409Al by seven times, demonstrating the influence of the Al-10%Si coating.

9. ASTM B117 material ranking: Type 436 > XHOM Masked Edges > Type 439 > Type 409Al > Type 409 > XHOM

10. All materials, barring one set of Type 409Al samples were heat treated (650 °C for 1 h) before conducting the exhaust gas condensate exposure. This heat treatment was found to have a drastic influence on the localized corrosion susceptibility of Type 409Al material. This is due to rapid diffusion of Fe and Cr from the substrate forming intermetallic phases within the coating.

This lead to a decrease in galvanic protection of the coating as well as the fabrication of microcracks caused by a difference in thermal expansion coefficients of intermetallic phases.

11. XHOM with exposed cut edges, exhibited a comparable corrosion rate to Type 409 in the exhaust gas condensate exposure as well as a lower localized corrosion susceptibility than heat treated Type 409Al.

12. Exhaust gas condensate material rankings: Type 409Al-A > Type 436 > Type 439 > Type 409 > XHOM > Type 409Al-H

7. Bibliography

[1] Y. Inoue and M. Kikuchi, "Present and Future Trends of Stainless Steel for Automotive Exhaust System," *Nippon Steel Technical Report,* vol. 88, pp. 62-69, 2003.

[2] J. Maki and T. Omori, "Development and Quality Properties of Aluminized Stainless Steel," *Nippon Steel Technical Report,* vol. 71, pp. 65-70, 1996.

[3] D. C. Oliver and M. Sephton, "External corrosion resistance of steel and ferritic stainless steel exhaust systems," *The Journal of The South African Institute of Mining and Metallurgy,* pp. 93-100, 2003.

[4] R. Veit, H. Hofmann, R. Kolleck and S. Sikora, "Investigation of the Phase Formation of AlSi-Coatings for Hot Stamping of Boron Alloyed Steel," *AIP Conference Proceedings,,* vol. 1315, pp. 769-774, 2011.

[5] K. Zaba, M. Nowosielski, P. Kita, M. Kwiatowski and T. Tokarski, "Effect Of Heat Treatment On The Corrosion Resistance Of Aluminized Steel Strips," *Metallurgy and Materials,* 2013.

[6] R. Baboian, "Designing Clad Metals for Corrosion Control," *SAE Technical Paper ,* pp. 1763-1771, 1972.

[7] C. S. Shepard, "Exhaust System Design – Art or Science?," *SAE Technical Paper,* pp. 1-4, 1969.

[8] L. C. Tsai, H. H. Sheu, C. C. Chen and M. D. Ger, ""The Preparation of the Chromized Coatings on AISI 1045 Carbon Steel Plate with the Electroplating Pretreatment of Ni or Ni/Cr-C Film," *Int. J. Electrochem. Sci,* pp. 317-331, 2015.

[9] D. G. A.R. Castle, "Chromium diffusion coatings," *International Materials Reviews,* vol. 44, no. 2, pp. 37-58, 1999.

[10] D. E. Blandy, "Material Alternatives for Today's Emission Control System," *SAE Technical Paper 750972,* pp. 1-6, 1975.

[11] S. Rajadurai, M. Afnas, S. Ananth and S. Surendhar, "Materials for Automotive Exhaust System," *International Journal of Recent Development in Engineering and Technology,* vol. 2, no. 3, pp. 82-89, 2014.

[12] R. Gedney, "Measuring the Plastic Strain Ratio of Sheet Metals," *ADMET INC,* pp. 1-3, 2005.

[13] A. Shrivastava, Introduction to Plastics Engineering, William Andrew Applied Science Publishers, 2018.

[14] Y. Emun, J. Kish, H. Zurob and T. Quan, "Comparative Corrosion Evaluation of Ferritic Stainless Steels for Automotive Exhaust Application," *SAE Technical Paper,* 2018.

[15] Y. HOU and G. CHENGv, "Effect of Nb on the As-cast Structure and Compactness Degree of Ferritic Stainless Steel Dual Stabilized by Ti and Nb," *ISIJ International,* pp. 1-10, 2018.

[16] J. K. Kim, Y. H. Kim, J. S. Lee and K. Y. Kim, "Effect of chromium content on intergranular corrosion and precipitation of Ti-stabilized ferritic stainless steels," *Corrosion Science,* vol. 52, p. 1847–1852, 2010.

[17] Z. Ahmad, Principles of Corrosion Engineering and Corrosion Control, Butterworth-Heinemann, 2006, p. 672.

[18] C. O. A. Olsson and D. Landolt, "Passive films on stainless steels - chemistry, structure and growth"," *Electrochimica Acta,* vol. 43, p. 1093 – 1104, 2003.

[19] J. B. Lee and S. I. Yoon, "Effect of nitrogen alloying on the semiconducting properties of passive films and metastable pitting susceptibility of 316L and 316LN stainless steels," *Materials Chemistry and Physics,* vol. 122, p. 194–199, 2010.

[20] V. Maurice and P. Marcus, "Adsorption layers and passive oxide films on metals," *Tribocorrosion of passive metals and coatings,* pp. 29-64, 2011.

[21] D. D. McDonald, "The Point Defect Model for the Passive State," *J. Electrochem. Soc,* vol. 12, pp. 3434-3449, 1992.

[22] G. S. Frankel, "Pitting Corrosion of Metals A Review of the Critical Factors," *Journal of Electrochemical Society,* vol. 145, pp. 2186-2198, 1998.

[23] P. Marcus, V. Maurice and H.-H. Strehblow, "Localized Corrosion: A model of passivity breakdown including the role of the oxide layer nanostructure," *Corrosion Science,* vol. 50, pp. 2698-2704, 2008.

[24] M. A. N. Ardilaa, W. S. Labiaparia and J. D. B. d. Melloa, "The Influence of Crystallographic Texture and Niobium Stabilisation on the Corrosion Resistance of Ferritic Stainless Steel," *Materials Research ,* vol. 20, no. 3, pp. 576-583, 2017.

[25] G. Lu, H. Cheng, C. Xu and Z. He, "Effect of Strain and Chloride Concentration on Pitting Susceptibility for Type 304 Austenitic Stainless Steel," *Chinese Journal of Chemical Engineering,* vol. 16, pp. 314-319, 2008.

[26] G. Wu, "Effect of Strain in General and Localized Corrosion Behavior of Steels," *Georgia Institute of Technology,* 2019.

[27] J. Lv, W. Guo and T. Liang, "The effect of pre-deformation on corrosion resistance of the passive film formed on 2205 duplex stainless steel," *Journal of Alloys and Compounds, ,* vol. 686, p. 176 – 183, 2016.

[28] A. D. SCHINO and J. M. KENNY, "Effects of the grain size on the corrosion behavior of refined AISI 304 austenitic stainless steels," *JOURNAL OF MATERIALS SCIENCE LETTERS,* vol. 21, p. 1631 – 1634, 2002.

[29] J. Horvath and H. H. Uhlig, "Critical Potential for Pitting Corrosion of Ni, Cr-Ni, Cr-Fe, and Related Stainless steels," *J. Electrochem. Soc,* vol. 115, no. 8, pp. 791-795, 1968.

[30] A. P. Bond, "Effects of Molybdenum on the Pitting Potentials of Ferritic Stainless Steels at Various Temperatures," *J. Electrochem. Soc.,* vol. 120, pp. 603-606, 1973.

[31] S. Kim, W. H. A. Peelen, K. Hemmes and R. C. Makkus, "Effect of alloying element on the contact resistance and the passivation behaviour of stainless steels," *Corrosion Science,* vol. 44, pp. 635-655.

[32] Z. M. Joe and D. R. Kim, "Characterisation of sensitisation of type 409 stainless steel," *British Corrosion Journal,* vol. 34, no. 3, pp. 210-213, 1999.

[33] M. I. Suleiman, I. Ragault and R. C. Newman, "THE PITTING OF STAINLESS STEEL UNDER A RUST MEMBRANE AT VERY LOW POTENTIALS," *Corrosion Science,* vol. 36, no. 3, pp. 479-486, 1994.

[34] D. Jones, Principles and Prevention of Corrosion, 2nd ed., Prentice Hall, 1996.

[35] W. Dong, L. Ma and L. Jiang, ", "Effects of Ti and Nb Stabilization on the Recrystallization and the Pitting Potential in Fe-21%Cr Ferritic Stainless Steels," *Materials Science Forum,* Vols. 561-565, pp. 77-81, 2007.

[36] A. Pardo, M. Merino, A. E. Coy, F. Viejo, M. Carboneras and R. Arrabal, "Influence of Ti, C and N concentration on the intergranular corrosion behaviour of AISI 316Ti and 321 stainless steels," *Acta Materialia,* vol. 55, no. 7, p. 2239–2251, 2007.

[37] X. Li, Y. F. Ni, Y. M. Jiang, J. Li and L. Li, "Intergranular Corrosion of Low Cr Ferritic Stainless Steel 429 Evaluated by the Optimized Double Loop Electrochemical Potentiokinetic Reactivation Test," *Hindawi, Advances in Materials Science and Engineering Volume,* pp. 1-10, 2015.

[38] H. Sidhom, T. Amadou, H. Sahlaoui and C. Braham, "Quantitative Evaluation of Aged AISI 316L Stainless Steel Sensitization to Intergranular Corrosion: Comparison Between Microstructural Electrochemical and Analytical Methods," *METALLURGICAL AND MATERIALS TRANSACTIONS A, ,* vol. 38A, p. 1269 – 1280, 2007.

[39] J. K. Kim, Y. H. Kim, S. H. Uhmb, J. S. Lee and K. Y. Kim, "Intergranular corrosion of Ti-stabilized 11 wt% Cr ferritic stainless steel for automotive exhuast systems," *Corrosion Science,* vol. 51, p. 2716–2723, 2009.

[40] A. International, "A268/A268M – 10: Standard Specification for Seamless and Welded Ferritic and Martensitic Stainless Steel Tubing for General Service," ASTM, West Conshohocken, PA, 2016.

[41] I. A. Franson and J. D. Fritz, "Stabilization Requirements for T409 Ferritic Stainless Steel," *SAE Technical Papers,* pp. 1-7, 1997.

[42] G. Zhang, Q. Gao and Q. Xu, Advances in Engineering Materials and Applied Mechanics, Wuhan, China: CRC Press, 2015.

[43] W. R. Patterson, "Materials, Design and Corrosion Effects on Exhaust-System Life," *SAE Transactions,* vol. 87, pp. 3294-3329, 1978.

[44] W.-J. Beom, K.-S. Yun, C.-J. Park, H.-J. Ryu and Y.-H. Kim, "Comparison of influences of NaCl and CaCl2 on the corrosion of 11% and 17% Cr ferritic stainless steels during cyclic corrosion test," *Corrosion Science,* vol. 52, pp. 734-739, 2010.

[45] E. McCafferty, Introduction to Corrosion Science, Springer, 2010.

[46] A. Steel, "Automotive exhaust system materials comparator," AK Steel Corporation, 2016.

[47] A. Olofsson, "Investigation of Materials for Use in Exhaust Gas Condensate Environment with Focus on EGR Systems," *UMEA University,* 2012.

[48] ATI, "ATI 409HP," *ATI Technical Data Sheet,* vol. 1, pp. 1-12, 2014.

[49] C. A. C. Sequeira, A. M. G. Pacheco and C. M. G. S. Nunes, "Formation of Diffusion Coating on Iron and Steel: 3 Aluminum, Chromium and Zinc Coatings," *Technica 2,* pp. 37-88, 1988.

[50] I. A. MENZlES and D. MORTIMER, "OBSERVATIONS ON THE CHROMIZING OF IRON AND PLAIN CARBON STEELS," *Corrosion Science ,* vol. 5, pp. 539-558, 1965.

[51] R. G. I. Leferink, H. Barten and W. M. M. Huijbregts, "Chromium Diffusion Coatings on Low-Alloyed Steels for Corrosion Protection under Sulphidizing Conditions," *VGB Krafterkstechnik,* vol. 73, no. 3, pp. 1-14, 1993.

[52] T. B. Massalski, "Binary Alloy Phase Diagrams", American Society for Metals.

[53] J. E. McDermott, A. G. Thomas and Z. M. Detweiler, "Methods for Chromium Coating". United States Patent US 20190062856A1, 28 February 2019.

[54] R. Prakash and B. N. Roy, "Quality Improvement in Finished Cold Rolled Sheet by reducing the defect," *International Journal of Scientific & Engineering Research,* vol. 7, no. 3, pp. 595-602, 2016 .

[55] ASTM, "Standard Practice for Operating Salt Spray (Fog) Apparatus," *ASTM International,* pp. 1-12, 2018.

[56] Ascott, "Ascott-analytical," Ascott, 2019. [Online]. Available: https://www.ascott-analytical.com/how-chambers-work/cct-chambers-salt-spray-mode-how-it-works/. [Accessed 2018].

[57] T. Quan, "Thesis Questions," Gmail, Grass Lake, Mi, 2019.

[58] V. Ludlow, K. G. Bain, S. Riaz, K. Muller, J. Wans, G. A. d. Toledo, S. Zajac and D. Senk, "Precipitation of nitrides and carbides during solidification and cooling in continuous casting," *La Revue de Métallurgie ,* pp. 17-24, 2006.

[59] J. Kim, H. Im, J.-m. Kim and J. Kim, "Thermal and electrical conductivity of Al(OH)3 covered graphene oxide nanosheet/epoxy composites," *Journal of Material Science,* vol. 47, p. 1418–1426, 2012.

[60] X. Si, J. Wu, Y. Tang, J. Li and Y. Jiang, "Effect of Pre-deformation on Microstructure and Pitting Corrosion Behaviour of UNS S32205," *International Journal of Electrochemical Science,* vol. 12, pp. 3916-3930, 2017.

[61] L. Peguet, B. Malki and B. Baroux, "Influence of Cold Working on the Pitting Corrosion Resistance of Stainless Steels," *Corros. Sci. ,* vol. 49, pp. 1933-1948, 2007.

[62] M. A. Amin, M. Saracoglu, N. El-Bagoury, T. S. Mohamed, M. Ibrahim, J. Wysocka, S. Krakowiak and J. Ryl, "Microstructure and Corrosion Behaviour of Carbon Steel and Ferritic and Austenitic Stainless Steels in NaCl Solutions and the Effect of p-Nitrophenyl Phosphate Disodium Salt," *Int. J. Electrochem. Sci.,* vol. 11, p. 10029 – 10052, 2016.